Thorsten Berstermann

Ultrafast Piezospectroscopy of Semiconductor Micro- and Nanostructures

Ultrafast Piezospectroscopy of Semiconductor Micro- and Nanostructures

Dissertation

presented to the Faculty of Physics of the
Technische Universität Dortmund, Germany,
in partial fulfillment of the requirements
for the degree of Doktor rer. nat.

presented by

Thorsten Berstermann

Dortmund, May 3, 2010

Accepted by the Faculty of Physics of the
Technische Universität Dortmund, Germany.

Day of the oral exam: 8th April 2010

Examination board:

Prof. Dr. Manfred Bayer
Prof. Dr. Metin Tolan
Prof. Dr. Götz S. Uhrig
Dr. Bärbel Siegmann

Contents

Part I

Introduction

1 Motivation and Outline

He who is certain he knows the ending of things when he is only beginning them is either extremely wise or extremely foolish; no matter which is true, he is certainly an unhappy man, for he has put a knife in the heart of wonder.

Robert Paul Williams

Light and sound have been daily attendants of mankind from time immemorial since they form the basic tools for interpersonal communication and experiencing nature. Nowadays *optics* and *acoustics* have evolved to be two of the main subjects in physics, still attracting interest of thousands of scientists working on light- and soundrelated phenomena all over the world. Soundwaves have been investigated in a wide frequency range in fields like seismology, medicine and material science, and have been found to offer a variety of possible applications. The wavelengths thereby cover a range from kilometers down to a nanometer scale, where the latter have led to the field of terahertz acoustics in solids, utilizing vibrations with ultimate wavelengths in the order of the atomic distances. To obtain information about the vibrational spectra in solids, several techniques have been developed, among of which optical spectroscopy has turned out to be a promising one.

The rapid developement of optical spectroscopy during the last decades was accelerated by more and more advanced laser systems available. The diversity of lasers thereby reaches from spectrally ultranarrow lasers, with linewidths down to Hz at well defined frequencies to ultrashort laser pulses, with pulse durations down to attoseconds, both close to constraints given by fundamental laws of nature. This developement was driven to a high extent by the progress in semiconductor physics, aiming at applications in the field of communication and information technologies. In particular miniaturized semiconductor structures, in which quantum effects became directly accessible required

highly sophisticated spectroscopic equipment.
Nowadays, it is possible to taylor the properties of these semiconductor nanostructures to a wide extend, such that it became feasible to study the interaction between various optically, acoustically and electronically well defined nanostructures with the ambition to experience nature on a quantum level and to apply the gained knowledge to everyday life.

This work focuses on the investigation of the impact of acoustic wave packages on the optical properties of semiconductor nanostructures using optical spectroscopy. In particular fast modulation processes will be presented, occuring on timescales comparable or even shorter than the typical optical response-, or rather interaction times of the structures under consideration. The experiments make use of a picosecond laser ultrasonics technique to generate the acoustic wave packages, which provide a powerful tool for reaching new acousto-optic and acousto-electro-optic regimes.
In this introductory part I, a reasonable physical background will be given in order to catch on with the physical context presented in part II. Readers who are familiar with the principals of ultrafast acoustics, semiconductor microcavity and quantum well structures as well as with two dimensional cavity polaritons may skip this part.
The introductory part is organized as follows. In Chapter 2 a review over the basic theoretical aspects of acoustics will be given. As a preface the phonon concept will be roughly summarized in Chapter 2.1. In Chapter 2.2 the main mechanisms of the used coherent phonon wavepacket excitation process are presented; its time evolution is discussed in Chapter 2.3, where anharmonicity and dispersion are shown to lead to distinct regimes concerning acoustic wavepacket propagation. In the subsequent Chapter 3 the attention will be on the basic properties of the semiconductor nanostructures investigated througout this work. In Chapter 3.1 the focus is on the optical properties of semiconductor Bragg microcavities, quantum wells as well as on cavity polaritons. In Chapter 3.2 the interaction mechanisms of these structures with an acoustic wavepacket are described separating acousto-optic and acousto-electro-optic effects. Chapter 4 comprehends a summary of the theoretical Part I and shows prospects with regard to possible constitutive experimental implementations.

2 Picosecond Laser Acoustics

Generally vibrations might occur in all physical systems in which a potential landscape, which favors a non singular equilibrium state is predominant. If any of theses systems experiences a small perturbation such that the energy of the system is increased, it will start to oscillate around its equilibrium state, with frequencies that can be related to the physical properties of the involved objects, as well as to the kind of perturbation.
In the following chapter an introduction will be given concerning lattice vibrations, which might occur in semiconductor crystal structures focusing on longitudinal, coherent crystal excitations referred to as *coherent longitudinal acoustic phonons*. These excitations will act as the key tool in the modulation processes described in Part II and are therefore of particular importance in the context of this work. In detail in Section 2.1 the phonon concept will be reviewed, where the basic idea as well as the most important phonon properties will be highlighted. In the subsequent Section 2.2 the focus will be on the excitation process of picosecond pulses of coherent longitudinal acoustic phonons, forming propagating strain waves. Further in Section 2.3 the mechanisms of nonlinear and dispersive strain wave propagation will be sketched, leading to shockwave and acoustic soliton formation.

2.1 The Phonon Concept

In order to describe the lattice dynamics in crystals it is convenient to take advantage of the *adiabatic approximation*, that separates the motion of the ionic cores from that of their valence electrons. Within the *adiabatic approximation* the electron dynamics are considered to evolve on timescales three orders of magnitude faster than those of the ion cores and can be approximated by the corresponding electronic ground state [1]. Turning now to the lattice dynamics translational symmetrie of the crystal reduces the problem to the unit cell, which includes all necessary information.
Within the unit cell one might only consider two body interactions [2] writing a potential $U(R)$ depending on the separation R of the atomic ion cores, or, simply spoken, the interatomic separation. Expanding this potential in terms of small displacements $u = R - R_0$ from the equilibrium separation R_0, one may write:

$$U - U(R_0) = u \left(\frac{\partial U}{\partial R} \right)_{R=R_0} + u^2 \left(\frac{\partial^2 U}{\partial R^2} \right)_{R=R_0} + ... \tag{2.1}$$

Following Equation 2.1, in second order approximation, the lattice dynamics may be expressed by a harmonic potential since the linear term vanishes on account of the

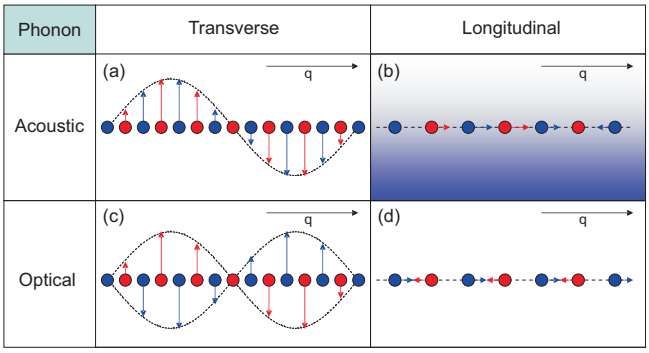

Figure 2.1: Phonon classification:(a) transverse acoustic phonon (b) longitudinal acoustic phonon (c) transverse optical phonon (c) longitudinal optical phonon.

definition of equilibrium. A crystal atom though, in this approximation can be described by a three dimensional harmonic oscillator, justifying the application of linear force models [1]. The electronic contribution thereby enters the model via the phenomenological force constants, whichs physical information might be a nontrivial task to understand [3][4][5].
Equation 2.1 can be solved by a travelling wave ($\mathbf{r}$-space, t-time) of the form $\mathbf{u}\exp[i(\mathbf{qr}-\omega t)+i\phi]$, where $\mathbf{q}$ denotes the wave vector, $\mathbf{u}$ the amplitude of displacement of the atoms from the equilibrium position, ω is the angular frequency of the wave with elementary excitation energy $\hbar\omega$, and ϕ its phase. This crystal excitation is called a *phonon* and describes collective oscillations of the lattice atoms. In general two classes of phonons excist referred as *acoustic phonons* and *optical phonons*, depending on whether the unit cell atoms oscillate in phase or in antiphase. Within these classes a phonon is called *transverse*, if $\mathbf{u}\perp\mathbf{q}$ or *longitudinal*, if $\mathbf{u}\parallel\mathbf{q}$. Figure 2.1 shows a chart from which all different kinds of phonons can be seen. The occupation of the different phonon states in thermal equilibrium is governed by the Bose-Einstein statistics, where the relation between the energies $\hbar\omega$ and the wave vector $\mathbf{q}$ is called the phonon dispersion. A calculated phonon dispersion for a GaAs bulk crystal, based on a one dimensional linear chain model [6][7] is shown in Fig. 2.2. As the model is one dimensional, only longitudinal phonons appear.

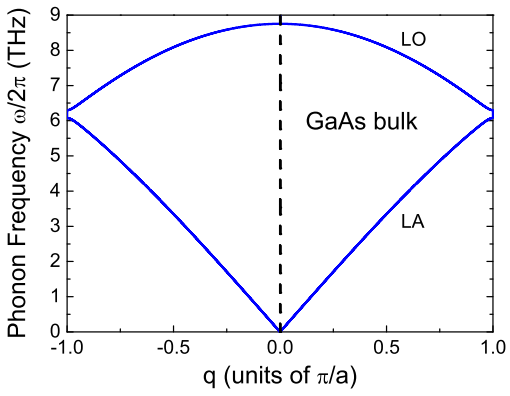

Figure 2.2: Real part of the phonon dispersion in bulk GaAs calculated from a linear chain model [6]: The interatomic force constant $\Lambda = 90.7$ N/m. Further the atom separation $a = 2.83$ Å, the masses $m_{Ga} = 69.723$ m, $m_{As} = 74.923$ m (m, atomic mass unit). (LO) longitudinal optical, (LA) longitudinal acoustic phonon branch. The gaps at both sides of the dispersion indicate nonzero imaginary parts of $\mathbf{q}$.

The phonon occupation in thermal equilibrium is usually referred as *heat* and characterized by the occupation number (i.e. how many phonons are apparent at a certain energy) given by the Bose-Einstein statistics, and the random phase distribution among them. If the occupation number differs from the Bose-Einstein statistics, one speaks about *nonequilibrium phonons* among of which the *coherent nonequilibrium phonons* appear with a well defined phase relationship. Nonequilibrium coherent phonons are of particular interest, since a manifold of them might show interference effects leading to notable lattice deformation, locally changing basic properties of the crystal.

2.2 Coherent Phonons

In the previous section the phonon concept was reviewed and coherent phonons were already highlighted, being in a fixed phase relation to each other. A lot of efforts have been taken to generate and detect either monochromatic [8][9][10][11], or broadband coherent phonons [12][13][14][15] in various structures the recent decades. The phonon frequencies reached up to the terahertz regime, focusing mainly on acousto-optical devices [16][17] or acoustic imaging and material inspection applications [18]. All these efforts have driven the field of acoustics to ultimate frequencies on the edge of constraints given by the lattice dimensions itself, and recently the focus has changed to tailoring the acoustic properties by building up structures on the nanometer scale.

In this work the main attention will be on the excitation of nonequilibrium longidudinal acoustic phonon wave packages, appearing as well localized strain waves in the time-space, that propagate with the longitudinal speed of sound in the respective material. The applied phonon generation technique might be referred as *picosecond ultrasonics* and will be explained in the following section following mainly Ref. [12]. For a more detailed analysis of the underlying physical processes see for example Refs. [19][20][21][22].

2.2.1 Excitation of Ultrashort Coherent Phonon Wavepackets

For simplicity, consider a metal film of thickness d and Reflectivity R, which is hit by a laser pulse of energy Q directed on an area A with diameter much larger than the penetration depth of light ζ into the film and the film thickness. Further consider this laser pulse to be much shorter in time than all relevant scattering mechanisms that might occur in the metal. Then the energy of this laser pulse will be transferred to the electron system, and the energy deposition per unit volume will be distributed along the z-direction (perpendicular to the metal film surface) according to[1].

$$W(z) = C\Delta T(z) = \frac{(1-R)Q}{A\zeta}\exp(-z/\zeta), \tag{2.2}$$

[1]possible diffusion processes are neglected in the following.

where C denotes the spezific heat. When the lattice and the electron system are assumed to be in thermal equilibrium the stress-strain relation [23] due to constrained thermal (isotropic) expansion of the metal can be written as

$$\sigma_{ij} = C_{ijkl}(\eta_{kl} - \alpha\Delta T\delta_{kl}). \tag{2.3}$$

Here η_{kl} is the strain tensor and α the thermal expansion coefficient of the metal. The elastic compliance tensor C_{ijkl} (Hooke's constants), determining the resistivity of the material to an applied stress, can be written as

$$C_{ijkl} = \frac{E}{2(1+\nu)}(\delta_{il}\delta_{jk} + \delta_{ik}\delta_{jl}) + \frac{E\nu}{(1+\nu)(1-\nu)}\delta_{ij}\delta_{kl}, \tag{2.4}$$

with Young's Modulus E and Poisson's Ratio ν, such that the stress-strain Relation 2.3 reads

$$\sigma_{ij} = \frac{E}{1+\nu}\left[\eta_{ij} + \frac{\nu}{1-2\nu}\eta_{kk}\delta_{ij}\right] - \frac{E\alpha\Delta T}{1-2\nu}\delta_{ij}. \tag{2.5}$$

Due to the geometrical conditions described above the only components (z-direction) of the stress (strain) tensor are σ_{33} (η_{33}). The equation of motion for the overall displacement though can be written as [24][25]

$$\rho\frac{\partial^2 u_3}{\partial t^2} = \frac{\partial\sigma_{33}}{\partial z} = 3B\frac{\partial}{\partial z}\left(\frac{1-\nu}{1+\nu}\frac{\partial u_3}{\partial z} - \alpha\Delta T(z)\right), \tag{2.6}$$

where $E = 3B(1-\nu)$ has been replaced by the Bulk Modulus B, $\eta_{33} = \partial u_3/\partial z$ by the spatial derivative of the displacement in z-direction, and ρ denotes the mass density of the metal. The solution of Equation 2.6 contains two components, among of which the propagating part of the strain, launched in z-direction is given by Equation 2.7. Equation 2.7 describes a bipolar strain wave i.e. with compressive ($\eta(z,t) < 0$) and decompressive ($\eta(z,t) > 0$) parts. The waves localization in time-space is given by the sound velocity v_s and the penetration depth ζ, where its amplitude is determined by the deposited energy density, i.e. the power of the laser used for the excitation process.

$$\eta(z,t) = -\left(\frac{3(1-R)Q\beta B}{2AC\zeta\rho v_s^2}\right)\exp[-(z-v_s t)/\zeta]\mathrm{sign}(z-v_s t) \tag{2.7}$$

The considerations above are summarized in Figure 2.3, where also hot electron diffusion and heat diffusion are sketched leading to a broadening and smoothing of the injected strain wave depending on the used metal. However, the produced strain wave will propagate through the metal film and will be reflected and transmitted partially due to the acoustic impedance missmatch at the interface. The reflection and transmission coefficients related to an acoustic wave of frequency ω, propagating with sound velocity $v_i(\omega)$ from material 1 to material 2 with mass densities ρ_i (i=1,2) expressed by the acoustic impedances $Z_i(\omega) = \rho_i v_i(\omega)$ are given by

$$R(\omega) = \frac{Z_2(\omega) - Z_1(\omega)}{Z_2(\omega) + Z_1(\omega)}, \quad T(\omega) = \frac{2Z_1(\omega)}{Z_2(\omega) + Z_1(\omega)}. \tag{2.8}$$

Once the strain wave has passed the interface toward a substrate (i.e. GaAs in this work) it is free to propagate over distances up to millimeters, depending mainly on the temperature of the lattice and the involved frequency components.

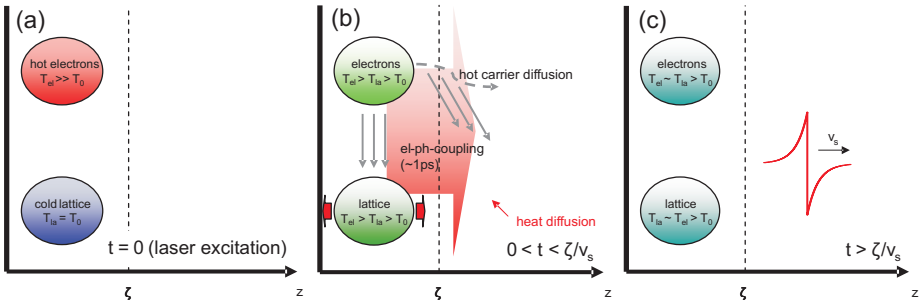

Figure 2.3: Three stages of the experimental strain wave generation process in the metal film. (a) The 150fs short excitation laser pulse heats the electron system in the surface region of the metal film within the penetration depth of light ζ according to Equation 2.2 to several thousand K. (b) Energy transfer from the electron system to the lattice. Due to thermal expansion of the lattice a local thermal stress is set up in the lattice in z-direction. The region of stress generation might be extended by fast heat diffusion or hot (not thermalized) electron diffusion [19] depending on the material. The time ζ/v_s indicates the escape time of the stress induced strainwave from the heated region (v_s-longitudinal sound velocity in the metal). (c) A bipolar strain pulse (red line: Equation 2.7) has been launched into the deeper part of the metal film. A substantial part of the energy has transferred to heat, leaving the lattice and the electron system at a temperature higher than before the excitation process.

2.3 Anharmonicity: Shockwaves and Acoustic Solitons

In the previous Section 2.2 it was discussed how a propagating strain wave might be injected into a material using a metal film. The strain thereby has been considered to be the first order spatial derivative of a lattice displacement originating from coherently excited longitudinal acoustic phonons. This section will provide a connection between the phonon concept, described in Section 2.1 and these strain waves, where the equation of motion 2.6 will be expressed in terms of energy. In this context, the harmonic approximation concerning Equation 2.1 will be extended toward higher order contributions, justifying the treatment of rather high strain amplitudes in an equation of motion beyond the harmonic approximation. In the end of this section the Korteweg-de-Vries (KdV) equation will be introduced, which describes the propagation of nonlinear dispersive strain waves and important features will be discussed.

2.3.1 Concept of Strain Energy

In order to understand the work necessary to elongate or compress a linear elastic object consider a rod of length L like shown in Fig. 2.4 [26]. The force P necessary to elongate the rod by ΔL thereby depends linearly on ΔL.

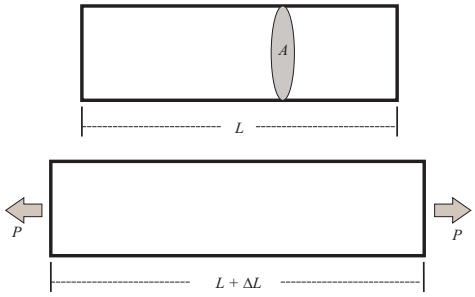

Figure 2.4: A rod of length L and cross sectional area A. The force P required to elongate the rod by ΔL.

Keeping in mind that $\eta_{33} = \Delta L/L$ and $\sigma_{33} = \tilde{C}\eta_{33}$ (compare Equation 2.3) in the one dimensional case one writes for the energy

$$U = \int_0^{L\eta_{33}} P d(\Delta L) = \int_0^{L\eta_{33}} \frac{A\tilde{C}}{L} \Delta L d(\Delta L) = \frac{1}{2} V \tilde{C} \eta_{33}^2 = WV, \tag{2.9}$$

where $\tilde{C}$ is an elastic constant and

$$W = \frac{1}{2}\sigma_{33}\eta_{33} \tag{2.10}$$

denotes the work necessary to elongate a quasi one dimensional rod such that its deformation is given by η_{33}. The work is stored in the rod as the potential energy of deformation, which is thought to be completely recoverable by switching off P. The stress σ now can be identified as the derivative of the energy of deformation with respect to the deformation (strain), yielding the equation of motion

$$\rho \frac{\partial^2 u_3}{\partial t^2} = \frac{\partial}{\partial z} \frac{\partial W}{\partial \eta_{33}}. \tag{2.11}$$

Comparing the right hand side of Equation 2.11 with Equation 2.1, it is obvious that the harmonic phonon approximation is recovered in the linear elastic strain energy concept, where all changes might be expressed by the local deformation relating neighboring atom displacements to the undisplaced lattice. Note that the phonon dispersion relation shown in Fig. 2.2 is a result originating from the discrete character of the lattice, which cannot be deduced from the strain energy concept.

2.3.2 Nonlinear Elastic Expansion

Starting from the harmonic potential approximation, it is nearby to take higher order expansion coefficients into account when dealing with higher local deformation. A generalized expression of Equation 2.9 including the higher order strain energy then might be written as

$$W - W_0 = C_{ij}\eta_{ij} + \frac{1}{2} C_{ijkl}\eta_{ij}\eta_{kl} + \frac{1}{6} C_{ijklmn}\eta_{ij}\eta_{kl}\eta_{mn} + ... \tag{2.12}$$

with $\eta_{ij} = (u_{ij} + u_{ji} + u_{ik}u_{kj})/2$ and $u_{ij} = \partial u_i/\partial r_j$ (r_j, directions). The nonlinear equation of motion up to the second order of the derivatives u then reads

$$\rho \frac{\partial^2 u_i}{\partial t^2} = \frac{\partial u_{jk}}{\partial r_l} \left(C_{ijkl} + u_{pq} A_{ijklpq} \right), \tag{2.13}$$

where the coefficients A_{ijklpq} establish the nonlinearity in the system and are given by second and third order elastic constants (see Equation 2.12)[24][25]. The physical effects arrising from Equation 2.13 will be illuminated in the next section in a simplified manner.

2.3.3 Korteweg-de-Vries Equation

In Section 2.2.1 it has been demonstrated that the induced thermal stress using a metal film and a sufficiently large area of laser excitation will lead to a localized bipolar deformation in time-space, which at most affects the z-direction i.e. the direction perpendicular to the metal film surface. This strain wave was thought to be injected into a substrate in which it might propagate over fairly long distances. In this particular case Equation 2.13 reduces to [27]

$$\rho \frac{\partial^2 u}{\partial t^2} = \left(C_2 + C_3 \frac{\partial u}{\partial z} \right) \frac{\partial^2 u}{\partial z^2}. \tag{2.14}$$

For simplicity all indices have been omitted, since this equation is a scalar one. In Equation 2.14 C_2 and C_3 are combinations of second and third order elastic constants. It follows from Equation 2.14, that a high strain amplitude $(\partial u/\partial z)$ wave obeys not a constant sound velocity anymore. Contrary it shows a deformation dependent, generalized sound velocity. Say C_3 is negative [24][27], then the compressive parts $(\eta = \partial u/\partial z < 0)$ of the strain wave propagate faster in time, whereas the decompressive parts slow down, yielding a self steepening process of the leading and the trailing edge of the wave after propagation over long distances due to nonlinear elasticity. The self steepening process resulting in an N-shaped shockwave is visualized in Figure 2.5.

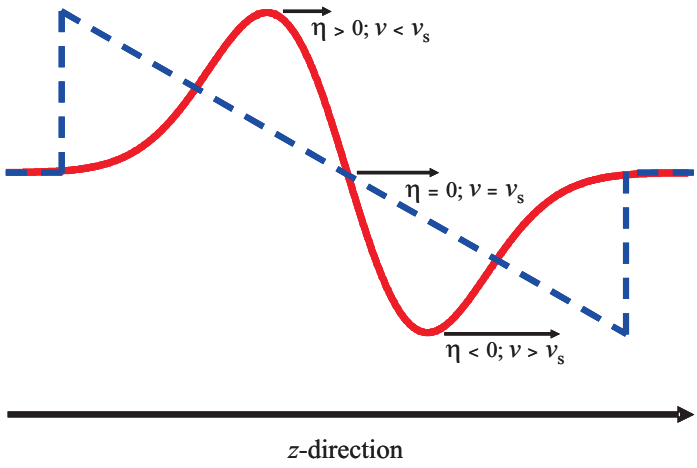

Figure 2.5: Sketch of the spatial shape change of a high amplitude strain pulse after propagating through a nonlinear elastic material. (Red curve) Injected strain pulse, approximated by the derivative of a gaussian function. Parts of the wave with $\eta < 0$ propagate faster than the longitudinal sound (v_s) whereas parts with $\eta > 0$ are slowed down (compare Equation 2.14). (Dashed blue curve) Nonlinear shockwave after long propagation distances.

Note in particular that the slope of the N-wave becomes *faster* after propagation at the leading and trailing edges, where it becomes *slower* in the center of the pulse. The fast rise at the edges of the pulse indicate high frequency components within the

fourier spectrum of the pulse. This suggests that a dispersionless treatment of the wave is no longer valid, since high frequency acoustic phonons propagate slower than low frequency ones (see also Fig. 2.2). However, since dispersion is a result of the discrete lattice it has to be added to Equation 2.14 artificially. The highest frequencies involved are around $\sim$ THz. Thus the dispersion relation might be expressed as

$$\omega^2 = v_s^2 k^2 - 2 v_s \gamma k^4 + ..., \tag{2.15}$$

where $v_s = (C_2/\rho)^{1/2}$ denotes the linear sound velocity and $\gamma > 0$ is the coefficient of the lowest order dispersion (v_s =4.77 km/s; $\gamma = 0.74$ in (001) GaAs [13]). The dispersive part of the motion in this case can be accounted for in Equation 2.13 by adding a term $2\rho v_s \gamma(\partial^4 u/\partial z^4)$ to the right hand side [27]. Differentiating with respect to z and replacing the displacement u by the strain η it follows:

$$\frac{\partial^2 \eta}{\partial t^2} = B_1^2 \frac{\partial^2 \eta}{\partial z^2} + 2 B_1 B_2 \frac{\partial}{\partial z}\left(\eta \frac{\partial \eta}{\partial z}\right) + 2 B_1 B_3 \frac{\partial^4 \eta}{\partial z^4} + ..., \tag{2.16}$$

where

$$B_1 = v_s,\ B_2 = C_3/2\rho v_s,\ B_3 = \gamma. \tag{2.17}$$

Equation 2.16 corresponds to the time derivative of the well studied Korteweg- De Vries Equation (KdV-Equation), and though contains its solutions, namely spatially unlocalized cnoidal solutions and the localized soliton solutions. Acoustic solitons in solids have been observed for the first time by *H.-Y. Hao & H. J. Maris* [27] and are characterized by high stability and a delicate balance concerning their nonlinear and dispersive properties. Solitons form the normal modes of the respective nonlinear system similar to the phonon modes in the linear system and therefore act as nonlinear crystal excitation with increased sound velocity [28].
Numerically calculated strain pulses with three different amplitudes before and after propagation through 114 μm GaAs material in (001) direction[2] [29] are shown in Figure 2.6. The chosen incident strain amplitudes cover three distinct regimes where nonlinear elasticity and dispersion is negligible (Fig. 2.6(a)), nonlinear elasticity is dominant but dispersion is negligible (Fig. 2.6(b)) and finally both, nonlinear elasticity and dispersion are of importance during the propagation (Fig. 2.6(c)).

[2]Calculated by P. J. S. van Capel - *Debye Institute, Department of Physics and Astronomy, University of Utrecht, Netherlands*

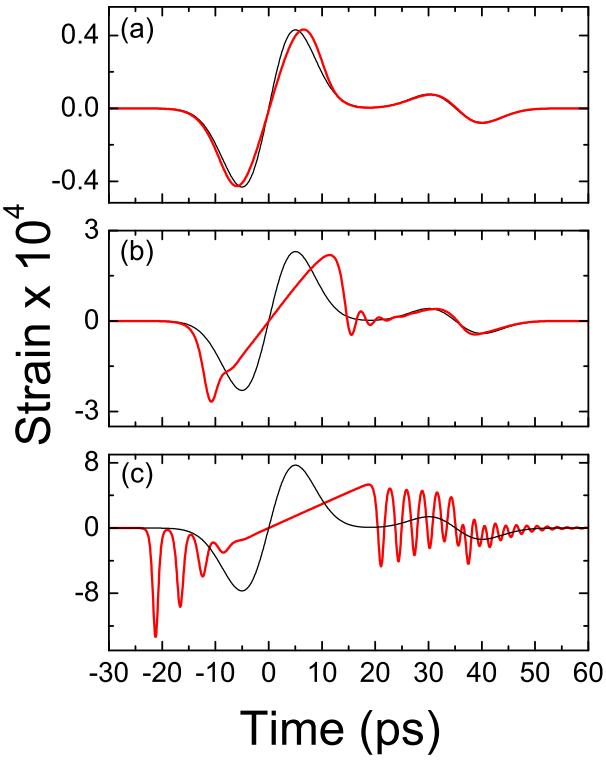

Figure 2.6: (a) Incident (thin black line) temporal pulse shape and resulting (thick red line) temporal pulse shape of a strain pulse after the propagation through 114 μm (001) GaAs. Dispersion and nonlinear elastic effects are negligible at the given strain amplitude resulting from an optical excitation density on the metal transducer of $P = 1$ mJ/cm^2. (b) Same as (a) but with increased strain amplitude ($P = 5.1$ mJ/cm^2) and notable nonlinear elastic effects (N-wave). (c) Same as (b) but with increased strain amplitude and notable dispersive effects (solitons at $P = 10.2$ mJ/cm^2).

The thin black curves show the incident pulse shapes as injected from the metal film [20], which show an additional pulse feature compared to the discussion in Section 2.2 around 35 ps originating from internal acoustic reflections in the metal film. The time separation between the first and the second feature corresponds to twice the propagation time of the pulse through the metal film. The thick red curves show the transformed pulses after the propagation. From Figure 2.6(a) it is obvious, that the strain pulse shape is approximately conserved along the propagation through the material. The pulse is almost linear, and only very weak nonlinear effects cause the maximum and minimum to diverge slightly. In Figure 2.6(b) the situation strongly differs. The maxima and minima of the strain pulse diverge by more than 10 ps while the edges become fairly steep, indicating the behaviour of a nonlinear shockwave in which the propagation speed depends on the local strain. Dispersive features are only of minor importance at the beginning of the leading edge and the end of the trailing edge, where a small peak and weak oscillations show up, respectively. Contrary, at high initial strain amplitudes (Fig. 2.6(c)) the behaviour of the wave again is qualitatively different. The overall pulse shape has spread in time, where the trailing part shows fast oscillations. The leading part shows three solitons, which have splitted off during the propagation and travel with a speed considerably higher than the center of gravity. Since real strain waves scatter on the thermal background phonons during the propagation through a material, the above assumptions hold for low temperatures

only. To account for this a term proportional to the third order derivative of the strain with respect to z might be added to the right hand side of Equation 2.16, yielding the KdV-Burgers equation [24]. Since the experiments here have been performed at low temperatures this fact is not further considered throughout this work. All of the above mentioned three strain regimes might be realized experimentally varying the excitation laser power on the metal film, and will lead also to various different effects concerning the detection of the investigated acousto-optic and acousto-electro-optic effects in Part II of this work. The basic optical properties of the studied structures will be given in the next Chapter 3.

3 Semiconductor structures

In Chapter 2 the principles of strain pulse generation and propagation have been reviewed. The second step is to present a basic overview concerning the optical and acoustic properties of the relevant semiconductor structures investigated in detail in this work, namely semiconductor quantum wells (QWs) and semiconductor microcavities (MCs). It is crucial to be aware of the mechanisms governing the optical response of these structures in order to study the interaction with the previously discussed acoustic pulses. Therefore it will be given an introduction to the optics of MCs and QWs in Section 3.1 of this chapter, as well as a description of the main principles of light-matter interaction, governing the coupled quantum well-microcavity dynamics. Afterwards, information on the interaction mechanism between the acoustic pulses and the respective semiconductor structure will be provided in Section 3.2, differentiating displacement- and traininduced phenomena. Additional information on spectroscopic details will be given in the corresponding chapter of Part II within this work.

3.1 Optics

Since in the 1950s the transistor promised to replace the *old fashioned* tube technology, semiconductors have evolved to be one of the main research subjects in solid state physics, where their electronic properties clearly were in the focus of interest. The importance of the optical properties of semiconductors was recognized not much later in the early 1960s when the possibility to fabricate semiconductor lasers was first discovered, demonstrating the need for a fundamental knowledge concerning the electro-optic response of semiconductors. Driven by the appearance of modelocked titanium-sapphire lasersystems in the 1980s, semiconductor optics and electro-optics nowadays are highly attractive for fundamental physics as well as for industrial applications, since the end of Moore's Law's validity seems to be close in the future. The need for optical nanoscale devices operating at THz-frequencies has pushed the field of semiconductor optics to the todays prominence, promising applications in information processing and communications. The downscaling process thereby has lead to heterostructures of various semiconductors with well defined interfaces of monoatomic layer precision, as well as to the quantum confinement of electronic and optical states down to zero dimensions, namely semiconductor quantum dots or nanoparticles (electronic) and photonic crystals (photonic). In the following the properties of MCs and QWs are discussed taking over the photonic and electronic part in this work, respectively.

3.1.1 Semiconductor Microcavities

Semiconductor microcavities have been fabricated and studied in various different ways like metallic and dielectric planar cavities, pillar cavities, microsphere and microdisc cavities as well as photonic crystal cavities, all aiming at the confinement of light in certain directions[30][31][32][33][34]. Here, the investigated cavity structures are formed out of distributed Bragg reflectors (DBRs), acting as mirrors that are positioned on both sides of a central cavity layer. The DBRs in such cavities usually consist of periodic stacks of two $\lambda_0/4$-layers of different refractive indices n_1 and n_2, where λ_0 is given in the simplest case by the spatial extension of the central cavity layer, i.e. $\lambda_0{=}n_c d_c$, where d_c is the thickness of the central layer. The periodic structure of the DBRs causes a photonic band gap called stop band, similar to the electronic band gaps in periodic crystal structures. Photons, propagating in the direction of the composed periodicity (say z-direction) are hindered to pass the cavity structure and are reflected efficiently. The reflected amount of light might be close to 100% depending on the photon energy, the number of stacks and the refractive index missmatch at the involved material interfaces. A sketch of such a Bragg resonator is shown in Figure 3.1. The central layer (defect layer) gives rise to a break in the symmetrie (periodicity) of the structure. The result is a dip in the photonic stop band reflectivity allowing for spectrally well defined photons to propagate in z-direction within the structure.

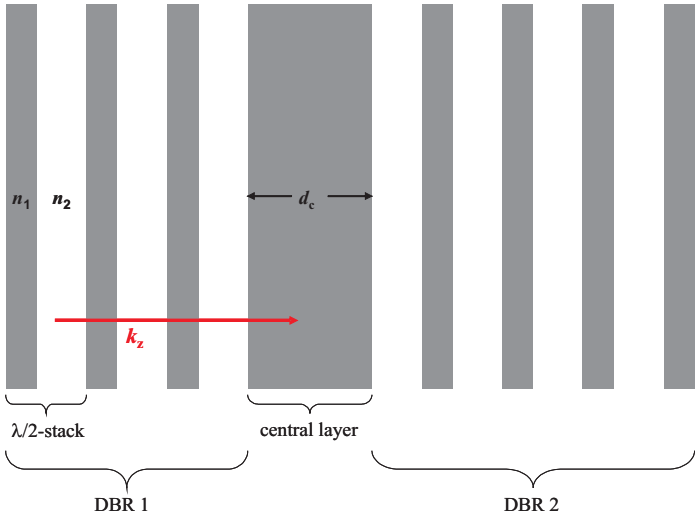

Figure 3.1: Sketch of an optical Bragg Resonator: (red arrow) Direction of hindered photon propagation; n_1 and n_2 refractive indices of the stack materials defining the thickness of the layers according to λ_0; DBRs forming top and bottom mirror; d_c central layer thickness

The optical response of a stacked structure can be calculated using a transfermatrix approach matching the boundary conditions of the corresponding electric field on the interfaces according to Maxwell's Equations [35][36]. For a TE optical wave (Transverse Electric), on the interface of two optical layers with refractive indices n_1, n_2, perpendicular to the layers surfaces, these boundary conditions read (transparency is assumed in the considered wavelength range)[1]

$$E_1 + E_1^{'} = \overline{E}_2 + \overline{E}_2^{'} \tag{3.1}$$

[1]Same for TM waves at normal incidence.

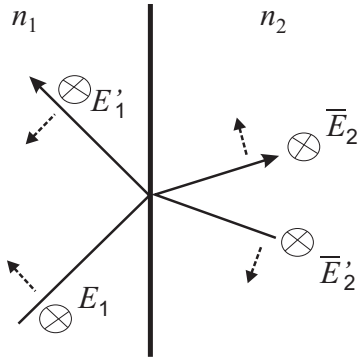

Figure 3.2: Boundary conditions for a TE wave at the interface i (say i=1) of two optical layers with refractive indices n_1,n_2. Forward and backward propagating waves are labelled with E_i and $E_i^{'}$ respectively. The fields on the left side of the interface are labelled E_i whereas on the right side the fields are labelled $\overline{E}_{i+1}$. The dashed arrows indicate the direction of the waves magnetic field amplitude. The described model assumes the angle of incidence to be zero.

$$H_1 + H_1^{'} = \overline{H}_2 + \overline{H}_2^{'}, \tag{3.2}$$

where E and H denote the electric and magnetic field of the wave, respectively, according to Figure 3.2. Replacing the magnetic field by the electric field assuming $H_i = \sqrt{\epsilon_i} E_i = n_i E_i$ it is possible to combine Equations 3.1 and 3.2 in the matrix equation[2]

$$\begin{bmatrix} 1 & 1 \\ n_1 & -n_1 \end{bmatrix} \begin{pmatrix} E_1 \\ E_1^{'} \end{pmatrix} = \begin{bmatrix} 1 & 1 \\ n_2 & -n_2 \end{bmatrix} \begin{pmatrix} \overline{E}_2 \\ \overline{E}_2^{'} \end{pmatrix}. \tag{3.3}$$

The dynamical matrices $D_1(n_1)$ and $D_2(n_2)$ thereby describe the boundary matching of forward and backward propagating waves on the left and right side of the interface, respectively, yielding an equation relating the fields on the left and right side via a combined matrix

$$\begin{pmatrix} E_1 \\ E_1^{'} \end{pmatrix} = D_1^{-1}(n_1) D_2(n_2) \begin{pmatrix} \overline{E}_2 \\ \overline{E}_2^{'} \end{pmatrix}. \tag{3.4}$$

The frequency dependence of the refractive index far off resonance has been assumed to be of minor importance in the following. Since in an extended multilayered structure the electro-magnetic wave, propagating through the layers, will change its phase, it is necessary to relate also the phases on both sides of each layer to each other, i.e. the phases of the fields E_i and $\overline{E}_i$. This will be accounted for using a propagation matrix P_i including the thicknesses d_i of the layers and only changing the phase of the respective wave. The phase change is given by

$$\begin{pmatrix} \overline{E}_i \\ \overline{E}_i^{'} \end{pmatrix} = P(d_i, n_i) \begin{pmatrix} E_i \\ E_i^{'} \end{pmatrix} = \begin{bmatrix} e^{i\phi(d_i,n_i)} & 0 \\ 0 & e^{-i\phi(d_i,n_i)} \end{bmatrix} \begin{pmatrix} E_i \\ E_i^{'} \end{pmatrix}, \tag{3.5}$$

where the phase ϕ_i is given by $\phi_i = 2\pi n_i d_i / \lambda$, and λ is the wavelength of the incident wave. All together the relation between forward and backward propagating waves of the first and the last (s) interface of a multilayered structure is given by

$$\begin{pmatrix} E_1(\omega) \\ E_1^{'}(\omega) \end{pmatrix} = D_1^{-1}(n_1) \left[\prod_{i=1}^{s} D_i(n_i) P_i(d_i, n_i, \omega) D_i^{-1}(n_i) \right] D_s(n_s) \begin{pmatrix} \overline{E}_s(\omega) \\ \overline{E}_s^{'}(\omega) \end{pmatrix} \tag{3.6}$$

[2]Permeability of the materials is assumed to be $\mu_i = 1$.

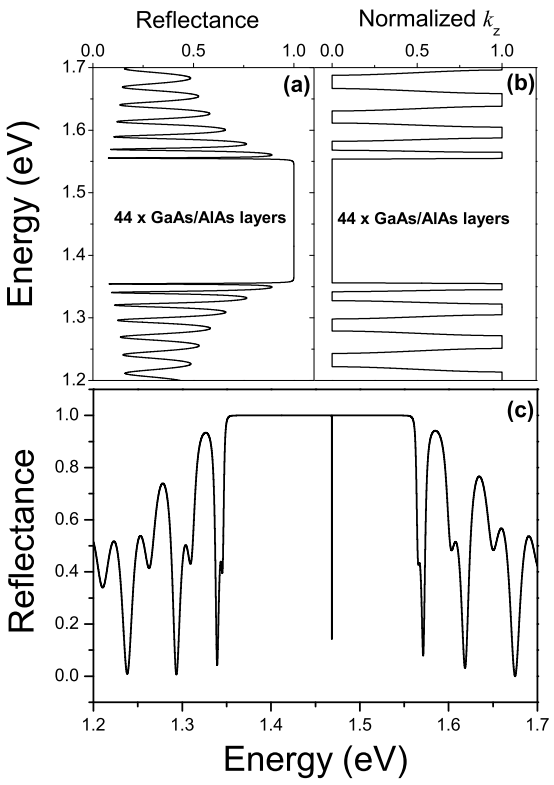

Figure 3.3: Calculated optical response of DBR structures using Equation 3.6. (a) Reflectance of a DBR with 44 GaAs/AlAs $\lambda_0/2$-layer stacks. A pronounced stop band is visible in the range from 1.35 eV - 1.55 eV. (b) Energy of the structure photons according to (a) in dependence of the normalized photon wavenumber k_z (real part). One corresponds to the brillouin zone edge originating from the $\lambda_0/2$ periodicity. (c) Same as (a) but with a defect layer of thickness $n_c d_c = \lambda_0$ incorporated after the 20th $\lambda_0/2$ stack. An additional sharp feature occours within the stop band with reflectance smaller than one, indicating a longitudinally confined photon mode. A photon with the photon mode energy might propagate within the structure in z-direction however with decreased speed. The speed thereby corresponds to the spectral width of the photon mode of the microcavity (not visible here) and is a measure of "how often" the photon will be reflected at the mirrors before escaping from the structure.

or

$$\begin{pmatrix} E_1(\omega) \\ E_1'(\omega) \end{pmatrix} = \begin{bmatrix} M_{11}(S,\omega) & M_{12}(S,\omega) \\ M_{21}(S,\omega) & M_{22}(S,\omega) \end{bmatrix} \begin{pmatrix} \overline{E}_s(\omega) \\ \overline{E}_s'(\omega) \end{pmatrix}, \tag{3.7}$$

with S, the layered structure of interest and ω, the frequency of the electromagnetic wave. In particular the reflectance of the structure is given by the squared modulus of $(M_{21}/M_{11})^2 = r_c(\omega)$ (i.e. the squared reflection coefficient of the structure) and its dispersion is given by the diagonal entries of M_{ij} (Fig. 3.3). The time dependence of a reflected infinitely short laser pulse is then given by the response [35]

$$R(t) = \left| \frac{1}{2\pi} \int_{\text{res}} r_c(\omega) e^{-i\omega t} d\omega \right|^2, \tag{3.8}$$

where "res" denotes the spectral resonance region. An example of calculated reflectance spectra and dispersion of DBR structures with and without defect layer is shown in Figure 3.3. Further the matrix $M_{ij}(S,\omega)$ containing the optical response to an incident wave of frequency ω can usually be expressed as $M_{ij}(\omega)$ if all structure parameters are assumed to be constants. However, concerning the experiments in this work this assumption does not hold, since a strain pulse is known to significantly alter the above discussed parameters of the microcavity (see Chapter 3.2).

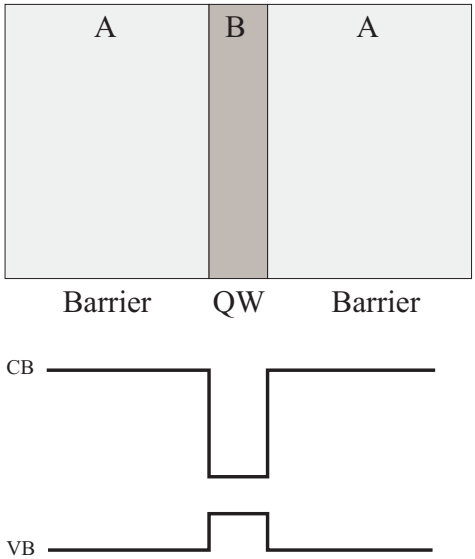

Figure 3.4: Sketch of a QW structure. (upper part) The QW material B is sandwiched between the barriers of material A. (lower part) Corresponding bandstructure in z-direction in a type-I material composition [38].

3.1.2 Semiconductor Quantum Wells

Where in the preceding section the optical response of an optical resonator was discussed, which is however a passive device, usually [37] not able to produce the photons that might be influenced by its presence, in this section the focus will be on an active medium called a semiconductor quantum well (QW). A QW is able to absorb and emit energetically well defined photons. In this structure the electronic (and hole) motion is restricted in one direction due to a composition of different band gap materials, which constitute a potential offset like sketched in Figure 3.4. This confinement gives rise to a discretisation of the quantum numbers in the respective direction and a steplike density of states compared to the square root behaviour in the bulk situation [38][39]. In particular the binding energy of the corresponding exciton (electron-hole) states [40] in a QW is increased making the resonance a very robust one with regard to the environmental temperature and applied external fields [41][42]. Further it is possible to tune the resonance energy of an exciton state by the influence of the confinement potential, tailoring the potential depth as well as its width [43]. The exciton Hamiltonian taking into account one valence and one conduction band within the effective mass approximation is given in Equation 3.9. The discretization only acts in direction of the confinement, i.e. the direction in which the different band gap materials have been grown (say z-direction).

$$\mathcal{H} = -\frac{\hbar^2}{2m_e}\frac{\partial^2}{\partial z_e^2} + V_e(z_e) - \frac{\hbar^2}{2m_h}\frac{\partial^2}{\partial z_h^2} + V_h(z_h) - \frac{\hbar^2}{2\mu}\left(\frac{\partial^2}{\partial \rho_x^2} + \frac{\partial^2}{\partial \rho_y^2}\right) - \frac{Ke^2}{\sqrt{\rho^2 + (z_e - z_h)^2}} \tag{3.9}$$

Here m_e and m_h are the electron and hole effective masses in growth direction, respectively, $\rho = \rho_e - \rho_h$ is the fraction of the electron-hole distance in the plane of the QW, μ is the in-plane reduced electron-hole mass and K is a constant. The potentials V_e and V_h describe the confinement potential due to the band offset in z-direction usually assumed to be steplike as sketched in Figure 3.4. It can be seen from Equation 3.9 that

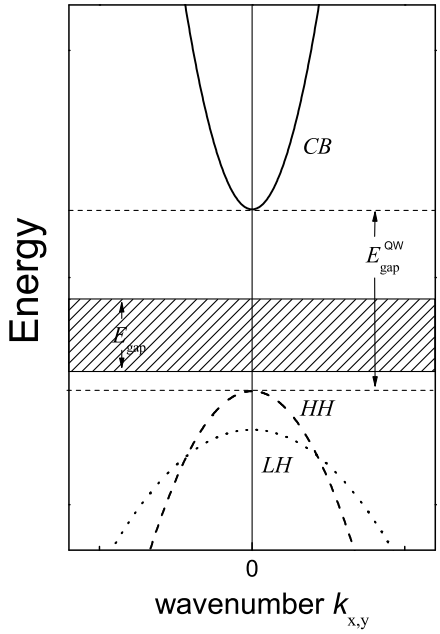

Figure 3.5: Sketch of a two dimensional (zinc blende) QW bandstructure (three bands). The two hole bands (dashed line: HH; dotted line: LH) lift their degeneracy in contrast to the bulk case for $k_{x,y} = 0$ due to the k_z-quantization with different effective masses $m^*_{z,\mathrm{HH}}$ and $m^*_{z,\mathrm{LH}}$ and the band gap E_{gap} is effectively increased (E^{QW}_{gap}). In particular it is $m^*_{z,\mathrm{HH}} > m^*_{z,\mathrm{LH}}$ perpendicular to the QW plane, where $m^*_{x,y,\mathrm{HH}} < m^*_{x,y,\mathrm{LH}}$ in the plane of the QW. The two valence bands anticross in the full Luttinger description [44].

the exciton solutions might be separable into z- and ρ-direction components depending on which direction has the largest impact on the coulomb term in the hamiltonian. However, the excitons get quantized in z-direction if the potential width of $V_{e,h}(z_{e,h})$ is sufficiently small ($(z_e - z_h)^2 << \rho^2$), which means that the dispersion of the electron and hole band, taken to be $\sim k^2$ in the bulk material turns into a constant offset in z-direction proportional to the inverse electron and hole effective masses [38]. The two dimensional bandstructure of a QW (zinc blende), including one conduction band (CB) and two (heavy hole HH, light hole LH) valence bands, is sketched in Figure 3.5 according to the quantized Luttinger Hamiltonian [44]. Later on in this work $k_{x,y}$ will be assumed to be close to zero in all cases. This leads to two distict exciton resonances in the optical spectrum, due to the coulomb coupling of the conduction band to the heavy hole as well as to the light hole bands (see Figure 3.6). A lift of the degeneracy might also be caused by stress applied to the structure. This may leads to a shift of the bands due to the materials deformation potentials, yielding a change in exciton resonance energy. A further discussion of this effect will be presented in Chapter 3.2.

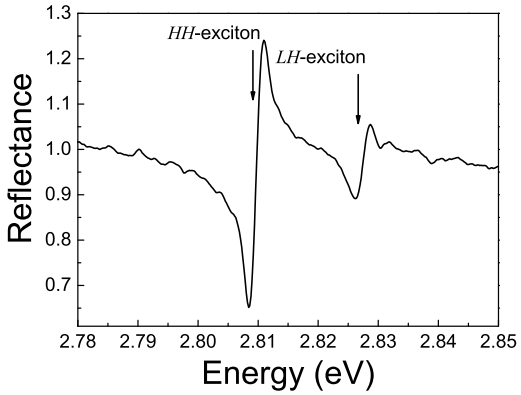

Figure 3.6: Measured reflectance of a ZnSe QW embedded between ZnMgSSe barriers [29]. Two exciton resonances are seen, namely the HH-exciton and the LH-exciton at lower and higher energies respectively.

The reflectance spectrum shown in Figure 3.6 differs from the simple shape of QW reflectance as given in references [38] and [35], which can be explained by additional interferences due to the QW top barrier layer thickness [45]. The spectral shape of the excitons (Fig. 3.6) can be written as

$$r_i^{QW}(\omega) = 1 + A_i \frac{\hbar(\omega - \omega_i)}{\Gamma_i^2 + \hbar^2(\omega - \omega_i)^2}, \tag{3.10}$$

where $\hbar\omega_i$ is the respective resonance energy ($i = \mathrm{LH}, \mathrm{HH}$), Γ_i denotes the resonances widths as seen from the measured spectrum, and the A_i are scaling constants.

3.1.3 Principles of Light-Matter Interaction

In this section a basic idea of light-matter interaction will be given, bringing together the previously discussed MC and QW structures. Consider a QW inside a MC at the antinode position of the confined light field (center of the defect layer). Matching the resonance energy of the confined exciton (say HH-exciton) to the confined cavity mode, it is possible to strongly enhance the light matter coupling, which is - without a cavity - limited by the QW's spatial extension. In particular it is possible to reach the strong coupling regime using a single QW in a planar MC structure as demonstrated by *C. Weisbuch et al.* [46].
The regimes of light-matter interaction can be distinguished by the relation of coupling parameters within the considered system. Where the exciton might couple to the environment by photons, leaving the QW or via interaction with phonons, the cavity will release photons with a coupling strength to the environment corresponding to its capability to confine photons as described in Chapter 3.1.1. However if these mechanisms are predominant in comparison to the exciton-cavity coupling, one speaks about the weak coupling regime, where the cavity mode principally acts as a filter function for the exciton. Nevertheless the radiative properties of the exciton will be altered due to the cavity's influence on the optical density of states, which may culminate in the purcell effect in completely confined photonic cavities [47]. If on the other hand a photon at resonance energy has the possibility to interact with the QW-exciton sufficiently often due to a high internal reflection propability at the cavity walls, and likewise the

photon absorption propability is efficient, the photon may be absorbed and reemitted several times before leaving the cavity. The state of such a system is no longer a pure photonic or excitonic state. Rather, the mixture of both states is called a polariton state i.e. a strongly coupled light-matter state, that manifests in an upper polariton and a lower polariton branch, in the following refered as upper (UP) and lower (LP) polariton. The energies of these lower and upper polariton branches are shifted with respect to the uncoupled cavity and exciton resonances towards lower (LP) and higher (UP) energies.
Here the main attention will be on the polariton energies and their photonic and excitonic character. To this extend the main results from a (semi) classical treatment will be introduced.
From the classical point of view it is apparent that the modes of two coupled ideal oscillators will not exhibit the same energies, irrespective of how the parameters of the system are changed. This phenomenon is known as the normal mode anticrossing, where the normal modes are assumed to be the new eigenstates of the coupled system. Assuming the exciton and the photon state in the cavity to be oscillators with the complex frequencies $\omega_l - i\gamma_l$ ($l = x$ and $l = c$ for the exciton and photon state respectively), one writes the coupled mode equation as [35][38]

$$(\omega_x - i\gamma_x - \omega)(\omega_c - i\gamma_c - \omega) = V^2. \tag{3.11}$$

In Equation 3.11 the imaginary parts γ_l of the uncoupled exciton polarisation and photon eigenfrequencies introduce the coupling to the environment of each mode (exciton nonradiative coupling). The coupling parameter V describes the exciton photon interaction strength. Solving Equation 3.11 with respect to ω yields two polariton frequencies

$$\begin{aligned} \omega_{\mathrm{UP,LP}} = \frac{\omega_x + \omega_c}{2} - \frac{i}{2}(\gamma_x + \gamma_c) \\ \pm \left[\left(\frac{\omega_x - \omega_c}{2} \right)^2 + V^2 - \left(\frac{\gamma_x - \gamma_c}{2} \right)^2 + \frac{i}{2}(\omega_x - \omega_c)(\gamma_c - \gamma_x) \right]^{\frac{1}{2}} \end{aligned} \tag{3.12}$$

as long as the squareroot term remains a real term. The polariton energies from Equation 3.12 might be written as $\hbar\omega_{\mathrm{UP,LP}} = E_{\mathrm{UP,LP}}(E_x, E_c, \gamma_x, \gamma_c, V)$. Defining the detuning

$$\Delta_d = E_x - E_c \tag{3.13}$$

one may write

$$E_{\mathrm{UP}}(\Delta_d = 0) - E_{\mathrm{LP}}(\Delta_d = 0) = 2\hbar\Omega_R, \tag{3.14}$$

where Ω_R is the so called Rabi-Frequency of the system, defining the minimum normal mode splitting as well as the frequency, with which the probability to find one of the polariton branches in a certain superposition state has swapped to the other branch and back. $2\Omega_R$ constitutes the beating frequency of both polariton branches. The polariton branches consist of a photonic and an excitonic part with periodically

oscillating propability amplitudes in time. The wavefunction of the overall polariton state reads [48]

$$|\Psi\rangle = |\mathrm{UP}\rangle + |\mathrm{LP}\rangle = (a_1(\Delta_d)|C\rangle + a_2(\Delta_d)|X\rangle) + (a_1(\Delta_d)|X\rangle - a_2(\Delta_d)|C\rangle) \quad (3.15)$$

with $|X\rangle$, $|C\rangle$ beeing the uncoupled exciton and cavity (photon) state vectors, and the Hopfield Coefficients [49] $a_1(\Delta_d)$ and $a_2(\Delta_d)$, which constitute the detuning dependent UP excitonic and photonic character, respectively (vice versa for the LP). Explicitly, the Hopfield Coefficient in the considered system read

$$a_1 = \frac{V}{\sqrt{2\Delta_1(\Delta_1+\Delta_2)}}, \quad a_2 = \sqrt{\frac{\Delta_1+\Delta_2}{2\Delta_2}}, \qquad \Delta_1 = (\omega_x - \omega_c)/2, \qquad \Delta_2 = \sqrt{\Delta_1^2 + V^2}. \quad (3.16)$$

Figure 3.7(a) shows the dependence of the polariton energies on the underlying exciton energy at fixed E_c. At resonance, i.e. $\Delta_d = 0$, the two branches anticross with a minimum energy distance of $2\hbar\Omega_R$. In contrast at increasing large values of Δ_d (far from resonance) the two polariton energies asymptotically approach the corresponding uncoupled state energies and likewise adopt the corresponding photonic (excitonic) content (Fig. 3.7(b)). At very large detunings Equations 3.12, 3.15 and 3.16 recover completely the underlying uncoupled exciton and cavity photon states.

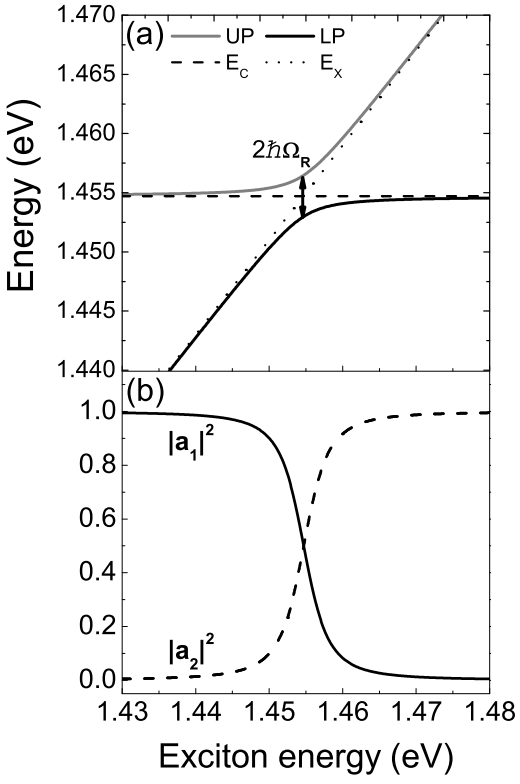

Figure 3.7: Calculated polariton properties according to Equations 3.12 and 3.16. The parameter have been chosen to be in agreement with the sample from Chapter 9 at zero angle of incidence. (a) UP and LP polariton energies in dependence on the underlying exciton energy E_x (dotted line). The cavity photon energy E_c (dashed line) is held constant. The polariton energies anticross at resonance i.e. $E_x = E_c$ with a splitting according to Equation 3.14. (b) Same dependence as in (a) but for the Hopfield Coefficients $|a_1|^2$ and $|a_2|^2$ following Equation 3.16.

3.2 Acousto-Optics and Acousto-Opto-Electronics

In the following, the concepts introduced in the preceding chapters will be merged to provide a basic knowledge about the interaction of picosecond acoustic pulses, like described in Chapter 2, with the introduced semiconductor structures.
The starting point will be the semiconductor Bragg-Resonator, i.e. an optical microcavity, which is subject to two interaction mechanisms. Beside the changes in the spatial dimensions of the periodic structure due to the dynamical displacement of the interfaces, the photoelastic effect will be discussed, changing the refractive index of each layer in the structure due to the strain. Further, the impact of the acoustic pulse on the bandstructure of the investigated semiconductor quantum wells will be discussed. The resonance energy shifts of the respective quantum well exciton resonance might be described by an effective deformation potential, which connects the bandenergies with the local strain.

3.2.1 Semiconductor Microcavities

The semiconductor Bragg-Microcavity, as described in Chapter 3.1.1, was shown to exhibit a sharp resonance within a photonic stop band in the growth direction of the periodic layers. The spectrum was explained by the interference of forward and backward propagating electromagnetic waves, reflected and transmitted at the Bragg-Resonators interfaces. Since coherent phonons likewise are able to show interference effects, according to Chapter 2.1 and Equation 2.8, similar restrictions will be present for the phonons sent to a Bragg-Resonator. The acoustic frequencies comprised in the applied acoustic pulses, ranging continuously up to more than a terahertz, will - in contrast to the optics - cover several tens of phononic stop bands. An example of a calculated phononic bandstructure of a GaAs/AlAs infinite superlattice is shown in Figure 3.8 [6]. The phonon dispersions of the bulk semiconductors are shown on the left (panel(a)), and the corresponding zonefolded phonon dispersion is shown on the right (panel(b)) side, originating from the additional optical period of the superlattice. Similar to the photons, the phonons on the zone edges are prohibited to propagate in the growth direction.

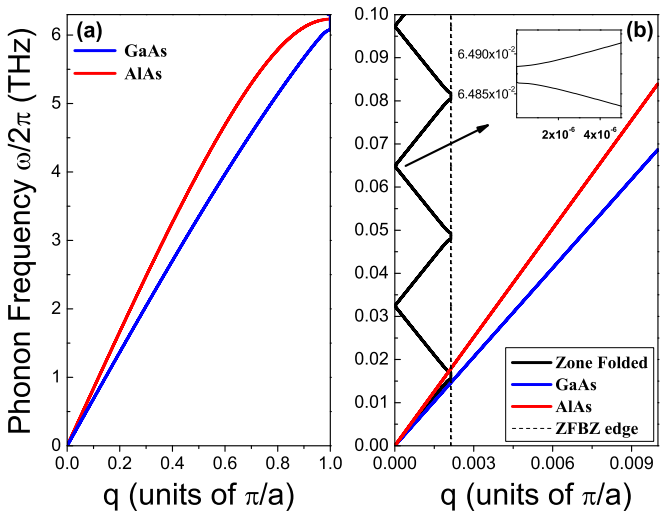

Figure 3.8: Phonon dispersion in an optical superlattice: (a) Bulk GaAs and AlAs LA phonon dispersion as in Fig. 2.2. Additional parameters: aluminum mass m_{Al} = 26.982 m, force constant AlAs Λ_{AlAs}=95.4 N/m. (b) Bulk dispersions as in (a) and the zonefolded LA phonon dispersion for an infinite superlattice yielded from the layer thicknesses d_{GaAs} = 60.07 nm and d_{AlAs} = 73.08 nm. (Dashed line) Zone folded Brillouin-Zone (ZFBZ) edge corresponding to the periodicity $d_{AlAs} + d_{GaAs}$. Phononic stop bands occour at the center and the edge of the ZFBZ.

Disregarding the influence of the acoustic pulse on the structure as well as nonlinearity (i.e. independent phonons), the missing and confined phonons change the temporal shape of the red pulse from Figure 2.6(c) within the central λ-cavity of the structure - discussed in more detail in Chapter 8 - to the shape shown in Figure 3.9 [50][3].

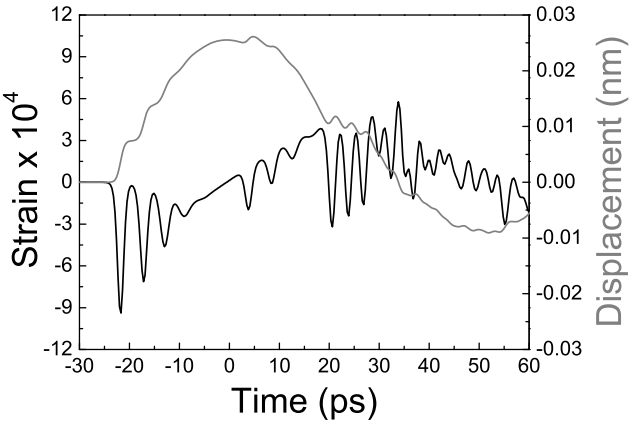

Figure 3.9: Short term temporal acoustic pulse shape in the middle of a GaAs/AlAs λ-cavity (see Chapter 8) corresponing to an acoustic pulse sent to the cavity as shown in Fig. 2.6(c)(red pulse). Black curve shows the strain profile [50]; grey curve shows the displacement profile.

Now, the question how the interaction of the acoustic pulse with the microcavity is established, or more specific, how the optical properties of the Bragg-Resonator might be changed due to the presence of an acoustic pulse is adressed. The obvious mechanism is the displacement of the interfaces constituting the structure, since the interface positions determine the interference pattern of the electromagnetic field according to Equation 3.6. A sketch of a Bragg-Resonator consisting of two materials

[3]Calculated by B. A. Glavin - *Institute of Semiconductor Physics, National Academy of Science, Kiev, Ukraine.*

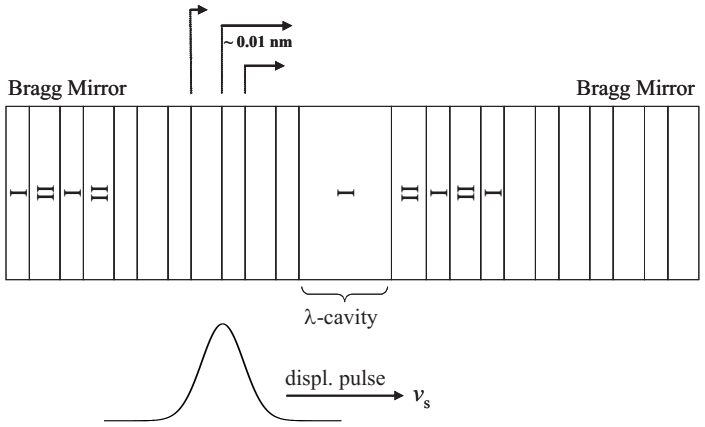

Figure 3.10: Sketch of a Bragg-Resonator, influenced by an acoustic pulse concerning the displacement profile. The pulse propagates with velocity v_s from left to right and subsequently moves the interfaces to the right side changing the respective layer thicknesses. The typical displacement amplitudes are ~ 0.01 nm [51].

(say material I and material II) is shown in Figure 3.10. The dynamical displacement, propagating from left to right, subsequently shifts the interfaces out of their equilibrium positions, where - depending on the spatial width of the acoustic pulse - one or more interfaces might be affected at once. As a consequence the right sided layer of a respective interface shrinks where the left sided one is expanded. The interference pattern though is expected to change and so the optical response of the microcavity. This purely geometrical aspect already gives an impression of the main changes in the optical response. In case the λ-cavity is shrinked one expects a shift of the cavity mode towards higher energies, if one assumes that the main contribution of an energy shift of the cavity mode is determined by the λ-cavity dynamical thickness. However the correct dependence might be calculated using Equation 3.6 with time dependent interface positions according to the propagating acoustic pulse. Since the reflected light polarisation depends also on the position within the stop band one might expect also changes in the polarisation of the resonance reflectivity [35].
Furthermore it is seen in Equation 3.6, that the optical response also depends on the refractive index n, which in the stationary case alternates with the periodicity of the Bragg-Mirrors except in the λ-cavity. The thicknesses d_i of the layers are matched such that the products $d_i n_i$ are one quarter of $d_c n_c$. The products $d_i n_i$ are also known as the optical thicknesses of the respective layers i and are changed due to the displacement of the interfaces as described above as well as to the change in the refractive indices, caused by the local strain of the acoustic pulse. The latter effect is known as the elasto-optic (or strain-optic, piezo-optic, acousto-optic) effect, which in general might be written as [52]

$$\Delta\left(\frac{1}{\epsilon}\right)_{ij} = -\frac{\Delta\epsilon_{ij}}{\epsilon_{ii}\epsilon_{jj}} = \sum_{kl} p_{ijkl}\eta_{kl}, \tag{3.17}$$

where ϵ_{ij} and η_{kl} denote the dielectric and the strain tensor respectively. The property p_{ijkl} is known as the photo-elastic tensor [53] and describes the changes in the dielectric tensor due to an applied strain. Neglecting absorption, Expression 3.17 might be

simplified to the first order in matrix notation concerning zinc-blende structures to

$$2n_x \Delta n_x = -n_x^4 p_{zz,x} \eta_{zz}. \tag{3.18}$$

In Equation 3.18 the additional assumtions of uniaxial strain in the growth direction (say zz-direction) of the structure and the case of normal incidence of linearly polarized light have been made, yielding the only photo-elastic constant $p_{zz,x}$ to be left. The constant $p_{zz,x}$ describes the influence of the uniaxial strain η_{zz} on the response of the transverse electric field. The influence of the local strain on the cavity layers is sketched in Figure 3.11, where $p_{zz,x}$ is in the order of ~ 0.1 and has been taken to be negative [54]. The dashed blue line indicates the equlibrium values of the refractive indices in the different layers where the solid blue lines indicate the respective average changes. The justification of the average is given by the altered average optical thickness of the layer, influencing the interference pattern of the incident light. In fact in this simplification no effects of propagating strain are present but time dependent optical thicknesses. A decreased refractive index means according to the above discussion that at a time when the compressive (leading) part of the strain reaches the λ-cavity the optical length will be decreased due to the displacement and due to the refractive index change in a similar way. Experimental details of the modulation process of the optical properties of a Bragg-Resonator will be discussed in Part II of this work.

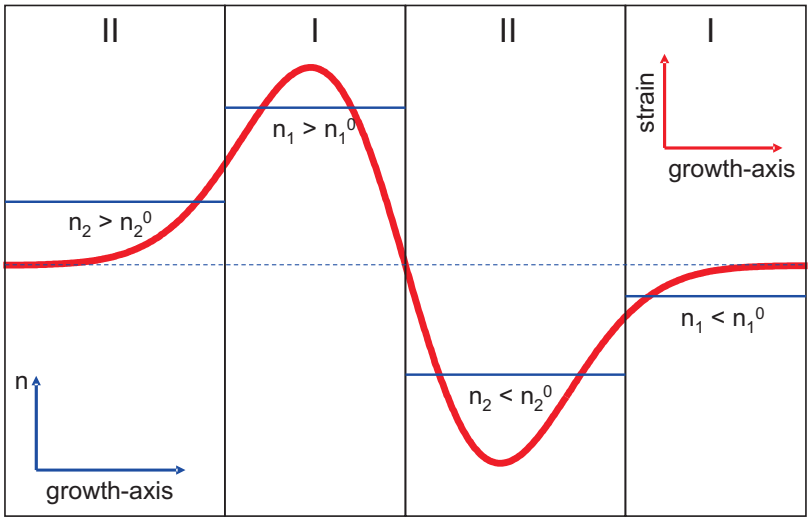

Figure 3.11: Sketch of the strain induced changes of the refractive index. The compressive strain reduces the equlibrium refractive index (dashed blue line) to lower values, while it is increased by the extensive part of the strain following Equation 3.18. The optical length of the layers change according to the strain induced average refractive index (solid blue lines).

3.2.2 Semiconductor Quantum Wells

In order to explain the electron-acoustic phonon interaction in a semiconductor, one needs to remind the adiabatic approximation concerning the atomic and electronic

systems like described in Chapter 2.1. The electronic energies in this approximation only depend on the "fixed" atom positions R_i $(i = 1, 2, ..., N)$ at any considered time and might be written [55]

$$E_{n\mathbf{k}} = E_{n\mathbf{k}}(R_1, R_2, ..., R_N), \tag{3.19}$$

where n and $\mathbf{k}$ are the electronic bandindex and wave vektor respectively; N denotes the number of participating atoms. The change in the electronic energies due to a vibration consequently can be expressed via the displacement u_i of the lattice atoms as

$$\left(\frac{\partial E_{nk}}{\partial R_i}\right) u_i. \tag{3.20}$$

It is obvious that if the phonon wavenumber q is equal to zero, no energy changes will appear since the crystal is displaced as a whole. Another necessary condition therefore is a non-zero deformation, i.e. a spatial gradient concerning the atom displacements. This gradient is described by the strain tensor η_{ij} discussed in the previous chapters. In the linear approximation [56] the strain wave (see 2.2.1) induced energy change of an exciton transition, which is constituted by the energy change in the conduction band as well as in the respective valence bands (see 3.1.2) might be written as

$$\Delta E_X^i(t) = a_i \eta_{zz}(t) \tag{3.21}$$

with a_i, being the overall deformation potential constants $(i = \mathrm{HH}, \mathrm{LH})$, connecting the strain with the band energies. The constants a_i comprise hydrostatic and tetragonal deformation potential constants concerning electrons and holes. The latter is responsible for a symmetry change in the crystal and therefore causes a lift of the degeneracy of the bulk heavy and light hole bands at $k = 0$ [57] similar to that induced by the dimensional feature discussed before (see Figure 3.5). The order of magnitude of the deformation potential a is ~ 10 eV in most semiconductors [55], leading to expected resonance energy shifts of the exciton transitions of ~ 10 meV within the considered strain conditions. Since in this work it is not possible to distinguish between different kinds of deformation potential constants, because only the exciton transition energy is considered, the description of deformation potential interaction will be restricted to the constant a. It is important to notice that a clear optical resonance energy response to a local dynamical strain in a quantum well is only possible due to the nanoscale of the QW-structure and is limited when the spatial variation of the strain gets shorter than the QW thickness.

4 Summary and Experimental Prospects

Summarizing the introductory Part I, an overview was concerning the main physical principals, necessary to understand the effect of a spatio-temporal localized strain wave on the optical properties of semiconductor microcavities, semiconductor quantum wells and the regarding optically coupled system was provided.
It was shown in Chapter 2 that the phonon concept, i.e. the theory of linear elasticity is a good starting point to derive the propagation of laser excited coherent LA phonon wavepackets, but limitations of this point of view are present at elevated strain amplitudes, that require a nonlinear description of lattice deformation. As a special feature of nonlinear elastic waves, the formation of shockwave fronts has been discussed. The dispersive effects in a shock wave thereby might cause the formation of supersonic solitary waves called acoustic solitons within the Korteweg- de Vries description of the dynamical strain.
In Chapter 3 the optical properties of semiconductor microcavities and semiconductor quantum wells have been reviewed, focusing on the reflectance spectra and the resonance reflectance time evolution. Further important features of the coupled quantum well exciton - cavity photon system were presented. Thereby the properties of cavity polaritons have been highlighted, being the new normal modes of the coupled system. In the last sections of Chapter 3 possible interaction mechanisms of the strain wave with the semiconductor structures have been considered. It turned out that for the Bragg microcavity, as a purely photonic system, the dynamical interface displacement as well as the photoelastic effect may alter the photonic mode energy in dependence of the strain wave. The interaction mechanism for the quantum well exciton is governed by the deformation potential interaction, defining the electron and hole band energies in dependence of the dynamical strain wave.
It is straight forward that other prospective interaction mechanisms occur in structures where for example piezoelectricity or magnetostriction are present. Also laser properties might depend on the strain application. An outlook concerning possibilities of the here applied techniques concerning different structures not considered in detail within this work will be given in the end of Part II.
There, the main questions to be answered are in which way, how fast and to what extend is it possible to modulate the optical resonance energies of the discussed structures using a strain wave. What conditions must be fullfilled for maximum modulation amplitudes and what are the restrictions? Which timescales play a role concerning the outcoming experimental results and how can these timescales be tailored? How and

to what extend can the light matter interaction in coupled systems be altered? Is it also possible to alter the radiative emission dynamics of a semiconductor system, to increase or decrease the amount of radiated intensity in dependence of the strain wave? These questions will be answered after the discussion of the experimental results in Part II. It will be shown that utilizing ultrafast modulation processes due to a strain wave, new regimes might be entered concerning the speed of the modulation of an optical resonance and the light matter interaction in a semiconductor. New strong features show up in the optical spectra, that can be related unambiguously to the strain waves temporal evoution.

Part II

Ultrafast Piezospectroscopy

5 Outline and Experiments

Turning now to the experimental point of view, in this first chapter of Part II a description of the used experimental setup will be given and the important timescales discussed in the following chapters will be introduced. Where this chapter is meant to give an overview with regard to the experimental method, details will be clearified in the respective chapters, which to a wide extend can be read independently with the focus on the chosen topic. However cross references will be given justifying the steps of argumentation, constituting to an overall understanding of the impact of strain waves on semiconductor microcavity structures.
Chapter 6 contains an analysis of the spectral response of a semiconductor Bragg resonator, as introduced in 3.1.1, to a propagating strain wave. Thereby the possibility of optical bandpass switching in resonator structures will be highlighted. In Chapter 7 a semiconductor quantum well acts as the object of modulation showing strong spectral effects due to the coherence time of the exciton transition, where in Chapter 8 the previously gained knowledge will be used to interpret the obtained results from a quantum well embedded in a Bragg resonator, reaching a new diabatic regime of optical resonance energy modulation. In Chapter 9 data will be provided, where the ultimate limits of strong and weak light matter interaction are reached (Chapter 3.1.3). In all of these chapters it is made use of spectral reflectance spectroscopy whereas in Chapter 10 the modulation of radiated spontaneous photoluminescense from a strongly coupled microcavity system is investigated. In Chapter 11 the results of Part II will be summarized and prospects will be given concerning future developement of utrafast piezospectroscopy. In particular the open questions arising from Chapter 4 will be under discussion.

5.1 Experimental Setup

The experimental setup consists essentially of a laser system, a cryogenic system and a detection scheme, all of which might be modified slightly in order to fullfill the required experimental conditions, e.g. the spectral region or the desired power level of the acoustic and optical excitation processes. A sketch of the setup is shown in Figure 5.1. The heart of the laser system is a *Coherent RegA 9000* regenerative optical amplifier, that intensifies the nanojule femtosecond light pulses from a standard titanium:sapphire source (repetition rate: 80 MHz) in order to reach femtosecond microjule pulses with a repetition rate between 50 kHz and 250 kHz preferentially at a wavelength of 800 nm. This is in particular desired for the excitation of high amplitude, nonlinear strain

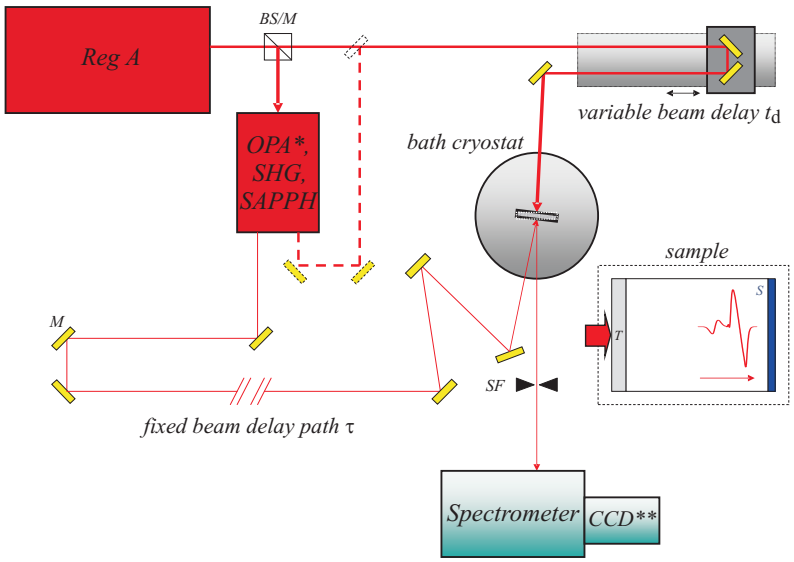

Figure 5.1: Experimental setup as described in the text: RegA: regenerative amplifier; OPA: optical parametric amplifier; SHG: second harmonic crystal; SAPPH: sapphire crystal; CCD: charge coupled device; T: transducer; S: semiconductor structure; BS: beamsplitter; M: Mirror; t_d, τ: see table 5.1; exchangable: (OPA, SHG, SAPPH)* ; (CCD, Streak Camera)**; red curve: propagating strain wave.

waves as described in Chapter 2.2. The output pulses of the RegA might be split using a beamsplitter, sending one part of the pulse through a nonlinear medium like a sapphire or an second harmonic generating (indicated as SAPPH and SHG) crystal and the other part - via a variable delay (t_d) - directly focused to the aluminum transducer. The transducer is deposited on the backside of each sample like shown in the inset of Figure 5.1. T and S here denote the metal transducer and the semiconductor structure under consideration, respectively. Alternatively the RegA output pulses can be sent to an optical parametric amplifier (OPA), enabling for a tunable frequency conversion in the visible and the near infrared spectral region. The OPA has an additional *residual pump laser ouput*, which exhibits sufficiently intense pulses for the strain wave excitation (dashed red line).

The cryogenic system typically consists of a bath cryostat, allowing for temperature control inbetween 2 K and room temperature, where also the detection angle relative to the surface of the samples can be controlled. After passing a fixed delay pass τ, which corresponds to the time the strain wave needs to travel from T to S, the conditioned second beam, e.g. the one sent through the SAPPH crystall, is focused opposite to the acoustic wave excitation spot onto the frontside of the sample (toward S) right onto the detection line. The detection line consists of a spatial filter as the main element in order to control the detected light cone.

Finally the reflected (or emitted) light from the sample is sent towards the detection apparatus, where a 0.5 m grating spectrometer followed by a CCD camera or a Streak Camera is used in order to detect the reflectance spectrum or the time resolved luminescence originating from the sample, respectively. A more detailed description of the measured signal properties and the relevant timescales is given in the next section.

Table 5.1: Important time definitions and timescales in this work

quantity (time)	explanation	typical timescale/range
τ	strain wave propagation	$>$ 20 ns
t_d	variable time delay	$<$ 3 ns
τ_l	luminescense decay time	$<$ 1 ns
τ_c	optical coherence decay time	$<$ 10 ps
δt_{exc}	excitation pulse duration	$<$ 200 fs
$t_{exc}(t,t_0)$	time of optical excitation	

5.2 Excitation and Detection

The properties and decay times of the detected signal will be shown to be of major importance for the experimental observations presented in Part II. Therefore a preliminary discussion is provided in this section to illustrate the basic experimental idea, before being discussed in more detail in the respective chapter. A scheme of the excitation processes of the strain wave and the optical signals as well as the related time quantities are shown in Figure 5.2. The corresponding timescales are given in Table 5.1. The strain wave is excited in the aluminum transducer and takes a time τ for propagating through the (GaAs) substrate of the sample before it reaches the semiconductor structure (see Fig. 5.1 (sample)). The propagation time τ is approximately 20 ns for a 100 μm thick GaAs substrate, assuming the longitudinal speed of sound to be 4800 m/s [58]. The variable time delay t_d offers the possibility to vary the overall delay between the strain wave excitation and the optical excitation. The optical excitation process at t_{exc} though, can be realized at any point in time concerning the passing strain wave at the respective semiconductor structure.
An important property of the detection process is the decay time of the optical excitation, which is given by the coherence time of the excited electromagnetic resonance polarisation τ_c (see also Chapters 3.1.1 and 3.1.2) or the radiative decay time of the excited photoluminescence τ_l in case of reflectance or photoluminescense, respectively (also referred to as t_2 and t_1). The timescales thereby can vary significantly in different experiments. Changing the resonance energy during the respective decay will be shown to potentially have influence on the measured (fourier) spectra under certain experimental conditions, which will be discussed in the following chapters (see box in the upper panel of Fig. 5.2). Thereby, it is obvious, that the slope of the strain (displacement) wave is a measure of how fast the system is changed at a certain time and will therefore be an important parameter in the evaluation of the experimental data.

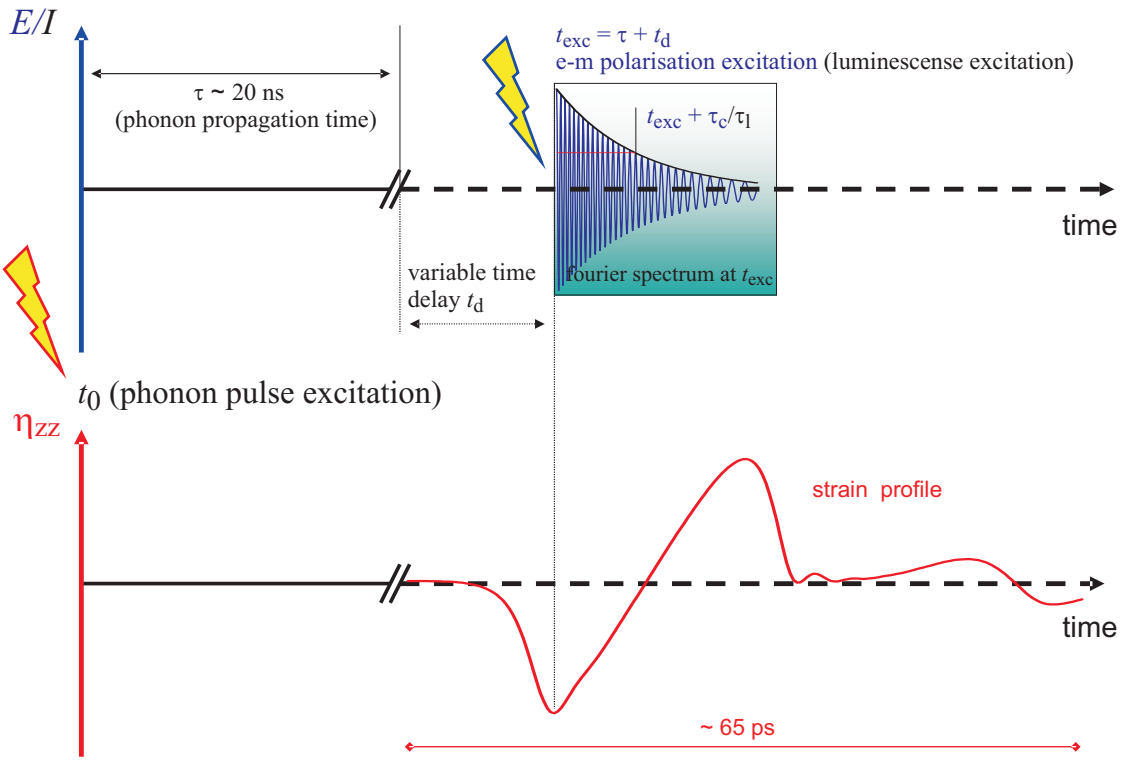

Figure 5.2: Scheme for the time relations of the excitation and the detection processes. Upper panel: optical excitation and decay process; lower panel: corresponding time evolution of the strain wave. In the box of the upper panel the detected time window for the coherent electromagnetic field decay (blue line) and alternatively the emitted luminescense intensity (black line) are given.

6 Optical Bandpass Switching in a Semiconductor Microcavity

Optical resonators and in particular the Bragg structures introduced in Chapter 3.1.1 have gained a lot of interest due to their ability to efficiently confine light. Improvements of the growth procedure nowadays have led to spectrally sharp cavity modes thats quality factors may reach values up to 10^5 spectrally surrounded by effective stop bands with close to unity reflectance [34][59]. The so formed optical bandpass though is able to filter a well defined photon energy and is defined by the optical dimensions of the Bragg structures. It is expected that such a structure shows a notable optical response to a propagating strain wave, altering the refractive indices of the layers and the positions of the interfaces (see Chapter 3.2), such that a switching of the transmission energy becomes feasible.
In this chapter reflectance spectra of the cavity mode in a II-VI semiconductor based planar microcavity, that is modulated by a strain pulse, will be presented. The modulation occurs when the strain pulse passes interfaces of the layered cavity structure at which the electric field has an antinode. Maximum modulation is reached when the pulse enters or leaves the central cavity layer. The mode shifts in the cavity with a finesse of about 2000 are comparable to its mode linewidth, which shows that the proposed technique is prospective for ultrafast optical switching.
Modulation of periodic structures have been achieved up to the MHz regime [60][17] using piezo-electric transducer techniques whereas the presented data here show modulations in the subterahertz regime, entering a new timescale concerning acoustic manipulation of photonic structures. In contrast to earlier experiments, investigating the elastic properties of semiconductor layered structures and phononic band gap materials [61][62][63][11][64][65][66], here the focus will be on the changes in the spectral optical response, where a maximum cavity mode energy shift of $\sim$ 1 meV is reached during tens of picoseconds [51].

6.1 Sample and Experiment

A scheme of the experimental configuration and the sample structure is shown in Fig. 6.1(a). The central $ZnS_{0.06}Se_{0.94}$ layer of the studied λ-cavity has a size of 196 nm, corresponding to the targeted wavelength of the cavity mode and is sandwiched between two DBRs formed by periodic stacks consisting of 18.5 (on the substrate side) and 15 (on the surface side) pairs of $\lambda/4$ layers of high (47 nm $ZnS_{0.06}Se_{0.94}$, $n_h = 2.684$) and

low (60.3 nm MgS/ZnCdSe superlattice, $n_l = 2.082$) refractive index materials [67][1]. The sample was grown by MBE on a 400 μm thick (001)-oriented GaAs substrate. The λ-cavity contains also three ZnCdSSe quantum wells around the central antinode position of the confined light field, whichs exciton transitions are in resonance with the cavity mode at room temperature. However, at cryogenic temperatures there is a 50 meV detuning of the quantum well exciton resonances to higher energies relative to the cavity mode [68], so that quantum well states do not need to be considered for the present experiments. A reflectance spectrum of the cavity at $T = 10$ K is provided in Fig. 6.1(b), showing the cavity mode at the energy $E_0 = 2.470$ eV. The spectral linewidth of the cavity mode is $\delta E = 1.2$ meV (spectral resolution 0.16 meV) leads to a quality factor $Q = E_0/\delta E \sim 2000$.

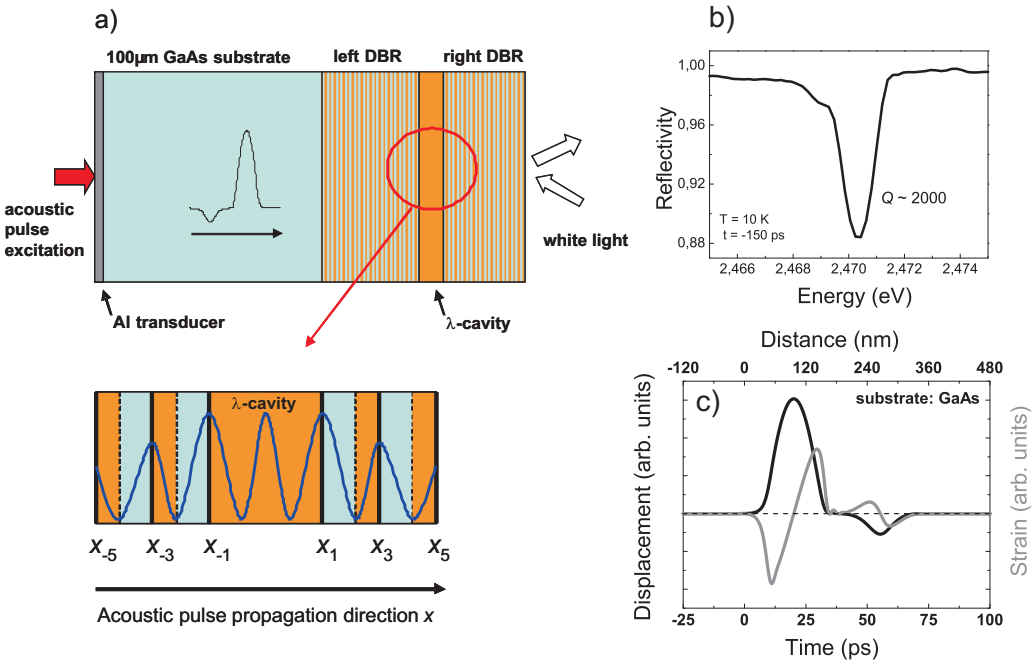

Figure 6.1: (a) Scheme of the experimental setup and sample structure consisting of the aluminum transducer, the GaAs substrate and the cavity, sandwiched between two Bragg mirrors. The indicated interfaces correspond to the antinodes of the confined electric field (modulus sketched by the blue solid curve) as described in the text. The displacement pulse is injected via a laser pulse, indicated as an arrow at the left side. Right arrows show the white laser pulses for probing the reflectance spectrum. (b) Reflectance spectrum from the microcavity structure without influence of the displacement pulse. (c) Typical temporal and spatial shape of the displacement pulse (black line) and the corresponding strain (grey line) during propagation through the sample. The dashed line indicates zero displacement/strain.

On the backside of the substrate a 100 nm thin aluminum film was deposited, after polishing the substrate down to a thickness of 100 μm. The film serves as the

[1]The refractive indices n_l and n_h are valid for a temperature $T = 10$ K and a photon energy $\hbar\omega_p = 2.431$ eV

transducer for the injection of the picosecond acoustic pulses into the GaAs substrate according to Chapter 2.2 (see also Fig. 6.1(a)). These pulses are generated by hitting the transducer with 150 fs short laser pulses (central wavelength 800 nm), emitted at a repetition rate of 100 kHz by a regenerative amplifier. The average power incident on the sample did not exceed 130 mW. A picosecond acoustic pulse is injected into the semiconductor substrate due to fast thermal expansion of the Al film after each excitation [19][21] (also referred to as pump). This pulse, consisting of a coherent acoustic wavepacket, propagates through the substrate with the longitudinal speed of sound ($v_{LA} = 4800$ m/s in GaAs) such that it reaches the cavity structure after a propagation time ~ 20 ns. The performance of the experiment in a cryogenic environment ensures that damping of the acoustic wave packet due to anharmonic interaction with thermal phonons is negligible [20]. The experiments were performed in a bath cryostat in which the sample was efficiently cooled by helium vapour. The temperature was measured by a sensor near the sample and stabilized at $T = 10$ K using a manostat, where no integrated temperature rise due to the optical pump excitation was observed. Figure 6.1(c) shows a typical temporal profile of a displacement pulse and the accompanying strain propagating in the GaAs substrate calculated according to Ref.[29], which was discussed earlier in this work (Chapter 2.3.3). The dominant part of the displacement pulse can be well modelled by a Gaussian function. The small negative dip at 55 ps corresponds to a displacement resulting from internal reflections in the Al film. The displacement amplitude is on the order of picometer for typical optical pump excitation densities P (1-10 mJ/cm^2) on the transducer, where the strain amplitude is 10^{-4} - 10^{-3}. The duration of the leading part of the pulse is about 20 ps corresponding to a spatial extension of 100 nm. The heat pulse, which is generated in the metal film in parallel with the displacement pulse is known to reach the opposite side of the substrate essentially later than the coherent pulse [69] so that it does not have to be considered further in the context of the following discussion.
After passing the GaAs substrate the acoustic pulse first reaches the left DBR of the microcavity (see Fig. 6.1(a)), then enters the central layer before reaching the right DBR. The measurement of the effects induced by the acoustic pulse on the optical spectrum of the microcavity is realized by recording the spectral reflectance spectrum using white light pulses originating from the same laser that excites the acoustic pulses in the transducer. The white light is generated by splitting off a part of the pulse emitted by the regenerative amplifier and sending it through a sapphire crystal (see Fig. 5.1). The white light pulse is reflected from the microcavity at variable time delays t, where the movement steps of the variable pump time delay provide sampling steps of $\delta t_d = 300$ fs[2].

6.2 Acoustic Pulse Induced Effects

Figure 6.2(a) shows a contour plot of experimentally measured reflectance spectra as a function of the delay time when a laser pulse with an energy density of 6 mJ/cm^2 per

[2]For simplicity the subscript in t_{exc} will be omitted in the following.

pulse hits the transducer. The delay time $t = 0$ shown by the dashed vertical line has been defined as the time when the maximum of the displacement profile of the pulse passes the middle of the cavity (at 6 mJ/cm^2). Note that the fixed delay time τ will be omitted.

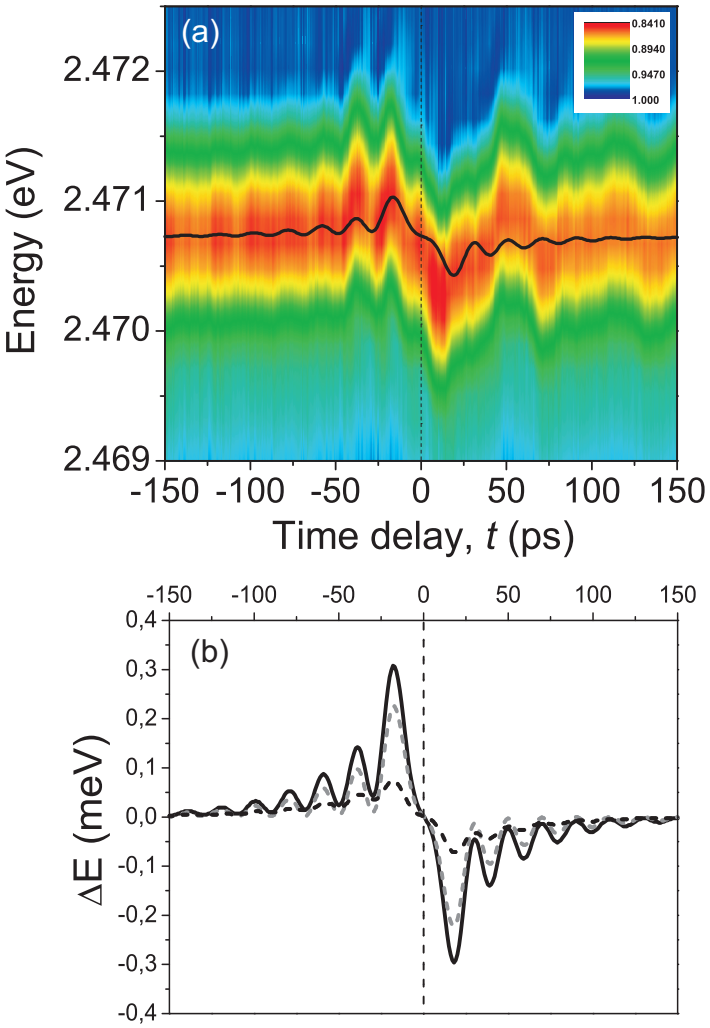

Figure 6.2: (a) Spectral/temporal contour plot of the reflectance in presence of the displacement pulse propagating through the structure measured at a laser energy density of $P = 6$ mJ/cm^2 on the transducer ($T = 10$ K). The black line shows the transfer matrix calculation of the time evolution of the resonance mode energy for a Gaussian shaped displacement pulse propagating with a velocity of 5365 m/s. The vertical dashed line indicates the time, when the middle of the cavity is maximum displaced. (b) Calculated energy response based on the displacement (dashed black curve), the photoelastic effect (dashed grey curve) and the combined response like shown in panel (a).

At times well before $t = 0$, the spectrum consists of the cavity mode, which for delays up to $t = -150$ ps basically undergoes no changes, showing that the acoustic pulse does not yet influence the microcavity within the experimental accuracy. At later times a modulation of the cavity mode is seen, which continuously becomes more pronounced up to $t \sim -20$ ps and shows a quasi-periodic temporal structure with repeated shifts towards higher energies compared to the unperturbed case. Maxima of the resonance energy modulation are reached at times, that are equidistantly spaced with a separation of 20 ps. The amplitude of the higher energy shifts has its maximum for the modulation peak at $t \sim -20$ ps and is equal to $\Delta E = 0.28$ meV. For later times $t > 0$ the mode shifts to lower energies by comparable amplitudes, but the temporal evolution of the modulation becomes more complicated and in particular the quasi-periodicity is lost. Figure 6.3(a) shows the corresponding reflectance plot for the

signal measured at twice higher excitation density P. The modulation of the resonance energy to higher energies is stronger and reaches a maximum of $\Delta E = 0.47$ meV, where the oscillations at $t < 0$ are not so pronounced as at lower excitation density (compare Figs. 6.2(a) and 6.3(a)). The inset in Fig. 6.3(b) shows the dependence of the maximum higher energy shift ΔE on P. It is seen that for $P < 9$ mJ/cm^2 this dependence is linear while at higher P saturation occurs.

6.3 Discussion and Analysis

To understand the temporal/spectral behavior of the reflectance signal, one has to consider: (*i*) the changes of the cavity mode energy E_0 induced by the displacement of the interfaces in the Bragg mirrors and (*ii*) how E_0 changes with the strain induced modification of the refractive indices in the respective layers. The results will be discussed at first on a qualitative level and will then be compared to the temporal/spectral evolution of calculations based on a transfer matrix formalism (see Chapter 3.1.1). The focus thereby will be on a propagating displacement pulse and will be generalized with respect to the strain later on.
While moving through the interfaces of the DBRs, the displacement pulse perturbs the periodicity of the structure by modulation of the interface positions x_i (see Fig. 6.1(a)), leading to variations of E_0. Apparently, if the modulation amplitude δx_i is not too large ($0 < |\delta x_i| << \lambda$) displacements of the interfaces where the electric field has antinodes change E_0, while the modulation of other interfaces where the electric field possesses nodes have negligible effect on E_0. In the studied λ-cavity, the field has antinodes in the centre and also at the edges of the central cavity layer [35] (sketched by the blue curve in the lower part of Fig. 6.1(a)). Thus the displacement of these edge interfaces ($i = 1$ and $i = -1$ in Fig. 6.1(a)) will have the biggest effect on E_0. Further the displacement pulse, which is propagating along the x-direction from left to right reaches the left edge of the cavity layer ($i = -1$) and induces a positive displacement ($\delta x_{-1} > 0$) corresponding to a compression of the cavity layer, and so to an increase of E_0. Later the displacement pulse reaches the right cavity edge ($i = 1$) inducing a positive displacement of the interface ($\delta x_1 > 0$). This leads to a tension of the cavity layer and thus, E_0 decreases. Qualitatively such behaviour is consistent with the experimental data presented in Fig. 6.2(a) and Fig. 6.3(a), where the energy shifts with $E > 0$ and $E < 0$ are observed at times $t < 0$ and $t > 0$ respectively.
The displacements of the uneven interfaces inside the DBRs ($i = \pm 3, \pm 5..$), at which the electric field possesses antinodes also affect E_0. These interfaces are marked by bold solid lines in Fig. 6.1(a) and correspond to refractive index changes from low to high along the x-direction. The influence of δx_i on E_0 in the DBRs will decrease with increasing distance of the respective interface from the cavity edges because the electric field is decaying exponentially inside the DBRs. The penetration depth of the light field into the DBRs is calculated to be 420 nm [35], corresponding to about twice the wavelength of the cavity. Therefore the displacement pulse moving through the left DBR from left to right induces an effect of δx_i on E_0 appearing as high energy shifts

with the amplitudes $\Delta E_i > 0$ at the temporal positions t_i when the pulse passes the corresponding interface. The value of ΔE_i increases when the pulse approaches the central layer. In the right DBR the process evolves in reversed order, so that $\Delta E_i < 0$ decreases when the pulse moves away from the cavity layer. The observation of the quasi-periodic oscillations in the experimentally measured temporal evolution of E_0 (Fig. 6.2(a)) while the displacement pulse passes the left DBR is also in agreement with this qualitative consideration.
Similarly it is possible to qualitatively include the effect of strain induced changes in the refractive index. It has been shown in Chapter 3.2 that a bipolar strain profile will cause the optical length of the central layer to decrease (negative strain) when the displacement pulse takes its maximum at x_{-1} taking into account the sign of the photoelastic constant [54]. Therefore it is intuitive, that the energy shift of E_0 due to the strain pulse follows mainly the direction as the one due to the displacement of the interfaces.
To be more specific calculations of the cavity mode energy in the presence of a moving Gaussian displacement pulse, corresponding to the dominant part of the pulse shown in Fig. 6.1(c) have been performed, using a transfer matrix formalism like discussed in Chapter 3.2 (see also Equation 3.6). The displacement of the interfaces is realized simply by setting the new positions as a function of the local displacement at each time. The layer thicknesses d_i and so the optical path in the layers changes correspondingly. For the photoelastic effect Equation 3.18 enters the calculation, where the elasto-optic constant is $p_{zz,x} \approx -0.2$ [54], and for the strain in each layer j the average

$$\tilde{\eta}_{xx}^{j} = \frac{1}{N_j} \sum_{n=1}^{N_j} \eta_{xx,j}^{n} \tag{6.1}$$

has been taken. Here $\tilde{\eta}_{xx}^{j}$ is the average strain in layer j, N_j is the number of available strain datapoints in layer j, and $\eta_{xx,j}^{n}$ is the local strain at datapoint n in layer j. The obtained effective refractive indices $\tilde{n}$ then enters Equation 3.6.
The result for the displacement amplitude 0.04 nm, corresponding to a strain amplitude of $0.7 \cdot 10^{-3}$, is shown in Fig. 6.2(a) by the solid line. For a sound velocity of 5365 m/s in the DBR good agreement between the experiment and calculations is seen in the time interval when the displacement pulse passes the left DBR and the cavity layer. The calculations confirm the main point of the qualitative discussion that the resonance energy changes only when the acoustic pulse passes the interfaces where the electric field possesses antinodes and the fitted strain and displacement values are in good agreement with earlier observations [70]. The contribution from the strain and the displacement of the acoustic pulse to the energy shift are shown seperately in Fig. 6.2(b) by the dashed grey and black lines respectively. The black line in Fig. 6.2(b) corresponds to the calculation presented in panel (a). The portion of the strain and displacement induced contributions thereby is easily seen to be dependent on the spatio temporal extension of the acoustic pulse, since at the same displacement amplitude the accompanying local strain amplitude - as the spatial derivative of the local diplacement - decreases with increasing spatial extension of the displacement pulse.

When the displacement pulse is propagating through the right DBR the experimentally measured signal behaves different from the one predicted theoretically. This discrepancy apparently is due to a more complex displacement pulse time evolution in comparison with the simple Gaussian shape used in the model. Indeed the layered structure of the microcavity will cause multiple reflections of the acoustic pulse at the interfaces resulting in oscillating features in the tail of the pulse [50].
Turning now to the discussion of the experimental result obtained for high values of P (Fig. 6.3) it is seen that the value of the maximum positive resonance energy shift ΔE_{-1} saturates at high excitation density (Fig. 6.3(b) inset) and the oscillations of ΔE_i $(x_{-3}, x_{-5}...)$ are less pronounced than for low P; compare Fig. 6.2(a) and Fig. 6.3(a). Such a behaviour is the result of nonlinear propagation when the acoustic pulse propagates through the GaAs substrate.

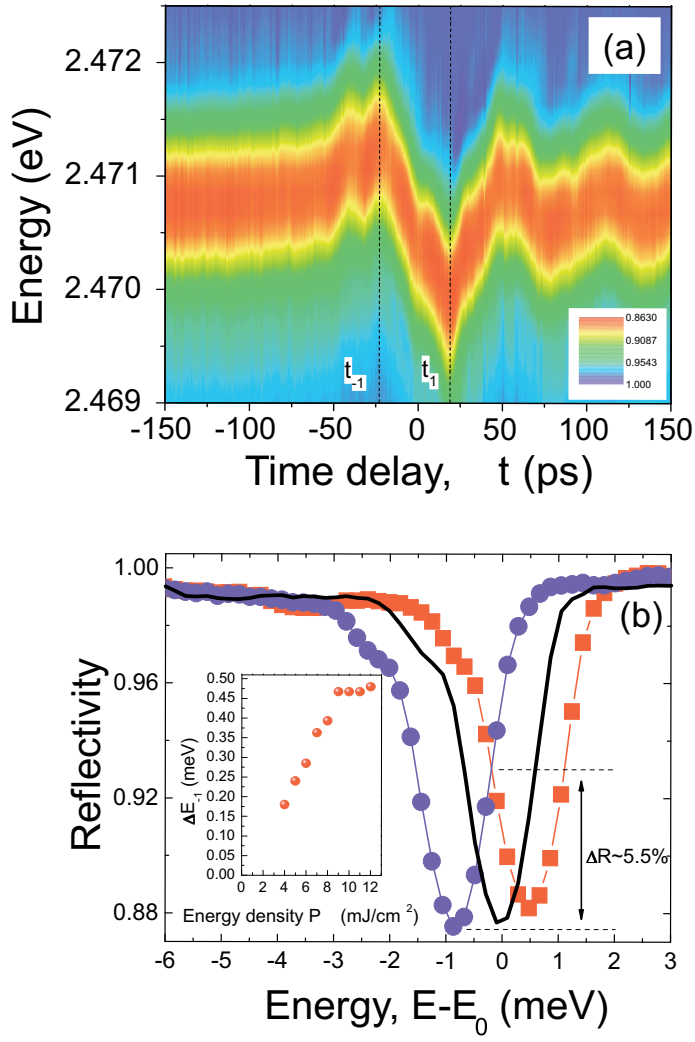

Figure 6.3: (a) Spectral/temporal contour plot of the cavity reflectance (see text) in the presence of the displacement pulse measured at a laser energy density of $P = 12$ mJ/cm^2 on the transducer ($T = 10$ K). (b) Three spectral cuts in panel (a), corresponding to the delay times $t_{-1} = -23$ ps (red squares), $t = -150$ ps (thick solid line) and t_1 (blue circles). (Inset) Dependence of the maximum higher energy shift ΔE_{-1} on the excitation laser energy P.

It is well known that at high P (i.e. high displacement and strain amplitudes) the initially injected Gaussian pulse spreads in time while the corresponding strain is transformed into a shockwave front, acoustic solitons and a dispersive tail [29][15] (compare

Fig. 2.6). Thus at high P the displacement pulse possesses a complex temporal shape covering more than one interface and correspondingly the oscillatory behaviour of E_0 becomes less pronounced. To illustrate this phenomenon Fig. 6.4 shows the expected energy response for three different spatio-temporal extensions of the acoustic pulse. It is clearly seen in the calculations that for a broader pulse the oscillatory behaviour of E_0 gets supresssed, when more and more interfaces are affected by the acoustic pulse at the same time. For shorter pulses the strain contribution dominates. The bipolar charakter of the strain wave and the differing thicknesses of the epitaxial layers of the high and low refractive index materials might lead - according to Equation 6.1 - to average refractive index changes in the different layers of opposite sign and of different absolute maxima, even if the photoelastic constant p_1 and p_2 in material 1 and material 2 are taken to be equal. As a result, at short pulse extensions, where the photoelastic effect dominates, the calculations show also a small shift $\Delta E < 0$ at time $t < 0$ not present at actual pulse extensions realized in the experiments.
The spatial spreading of the displacement pulse with the increase of P also explains the saturation of ΔE_{-1} at high densities; inset of Fig. 6.3(b). Furthermore the complicated pulse shape can lead to the fact, that the maximum of the lower energy shift $\Delta E_1 = -0.8$ meV at $t_1 = 19$ ps appears to be notably larger than ΔE_{-1} at $t_{-1} = -23$ ps at high excitation densities. This difference can be seen in Fig. 6.3(b) where corresponding cuts through the reflectance spectra are shown. Indeed spreading of the negative and positive displacement parts of the pulse over the left and right DBRs will induce bigger shifts of E_0 in comparison to those induced by a Gaussian shaped pulse or an asymmetric strain profile.
The maximum measured cavity mode energy shift from higher to lower energy is equal to 1.3 meV which is comparable to the cavity mode spectral width of 1.2 meV. This can be seen in Fig. 6.3(b), which shows spectral cuts of Fig. 6.3(a) at t_{-1} (red squares) and t_1 (blue circles). The cut at $t = -150$ ps (thick solid line) corresponds to an energy of the cavity mode, that is not yet affected by the displacement pulse. Taking into account the resonance width, the observed reflectance change is 5.5 % at an energy exceeding (being equal) the width of the cavity mode. This corresponds to a change in transmission of 50 % for negligible absorption.

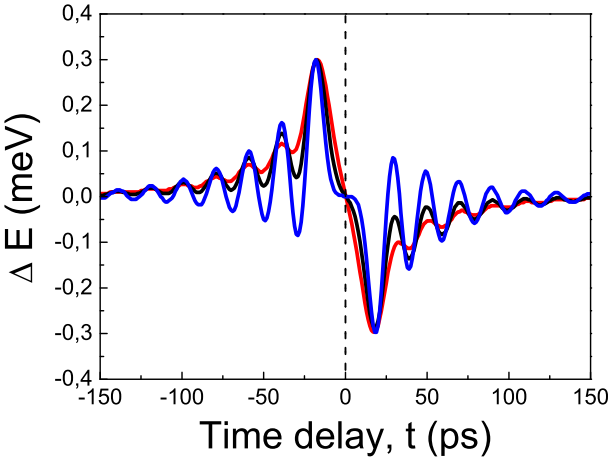

Figure 6.4: Calculated energy response of the cavity mode as described in the text. (black curve) same dependence like shown in Fig. 6.2. (blue curve) Spatial extension of the acoustic pulse 70 % of that building the black curve. (red curve) Spatial extension of the acoustic pulse 130 % of that building the black curve.

6.4 Summary and Outlook

It was demonstrated that the cavity mode energy is changed within tens of picoseconds when a displacement pulse moves mirror interfaces close to the central layer of the λ-cavity at which the confined light field takes its extrema. An oscillatory behaviour of the cavity resonance energy is observed, where the measured signals are induced by processes which were not reported in earlier works where the oscillatory behaviour of the probe intensity was observed (see for example [71]). The reported results open many possibilities among of which the obvious and attractive one is ultrafast modulation of the filtering function of a resonator. For such applications, one may increase the Q value of the resonator by an order of magnitude to perform a complete ps-switch, offering the possibility of ultrafast gating. The characteristic time dependence of the switch might be tailored by controlling the shape and the spatial extension of the displacement pulse using acoustic filters and alternative metal transducers. In this respect combination of optical and acoustic microcavities may be a step forward to THz modulation of light. But also for fundamental quantum effects, resonator modulation may turn out to be attractive. High quality resonators may also be formed by a Bragg mirror and a metal tip that is positioned close to the Bragg mirror by a piezo drive. In such a resonator huge field enhancements may be obtained, whose amplitude may be modulated through modulation of the Bragg mirror. Further the investigation of the dynamical Casimir effect, based on the action of fast oscillating cavity boundaries on the vacuum field might be a prospective application [37].

7 Chirping of an Optical Transition in a Quantum Well

Modulation of the optical properties of a Bragg Resonator as a high quality photonic structure has been demonstrated so far in the previous Chapter 6. Optical resonators however, are passive structures, altering the photonic mode densities in certain directions intended to show negligible optical absorption at the working frequencies.
It is further interesting to investigate the response of an active opto-electronic medium (see Chapter 3.1.2) to the strain waves described previously. The nonlinear elastic properties of solids result in the phenomenon of the transformation of a coherent strain wave to a train of ultrashort acoustic solitons (see Fig. 2.6). Such an acoustic soliton might occupy a space as small as a few nanometers, corresponding to durations as short as a few hundred femtoseconds, and may reach strain amplitudes exceeding 10^{-3} [27][15][72][73][74][14]. These spatial and temporal characteristics of acoustic solitons are close to the typical sizes of nanostructures (quantum wells, wires and dots) and relaxation times of their electronic excitations and constitute a new way of THz modulation in semiconductor optics.
In this chapter it will be demonstrated, that acoustic solitons, formed during the propagation of a picosecond strain pulse in a GaAs crystal with a
ZnSe/ZnMgSSe quantum well (QW) on top, lead to exciton resonance energy shifts of up to 10 meV within picoseconds and ultrafast frequency modulation, i.e. chirping, of the exciton transition. The effects are well described by a theoretical analysis based on the Korteweg- de Vries equation and accounting for the properties of the excitons in the quantum well [29], where beside the strain wave shape and amplitude the most important parameters will be shown to be the exciton resonance coherence time and the finite QW width. Good agreement between experiment and theory is reached, which paves the way for a new class of ultrafast acoustic experiments in semiconductor opto-electronics.

7.1 Sample and Experimental Conditions

Figure 7.1 combines the starting positions concerning the given physical problem as described in detail in the previous Chapters 5, 3.1.2 and 2.2. The idea and scheme of the experiment are shown in Fig. 7.1(a). The sample used was a (001)-oriented GaAs slab with a thickness $l_0 \sim 100$ μm. The heterostructure deposited by MBE on the front side of the slab was a ZnSe QW with a width $a = 8$ nm embedded between

$Zn_{0.89}Mg_{0.11}S_{0.18}Se_{0.82}$ barriers [75]. As the thermoelastic transducer a $\sim$ 100 nm thin aluminum film was deposited on the backside of the GaAs slab. In the experiments the sample was immersed in liquid helium ($T_0 = 1.8$ K), and the Al film was excited by 200 fs pulses from an amplified ti:sapph laser (wavelength 800 nm) with a repetition rate of 250 kHz. This pump beam was focused to a 100 μm FWHM spot on the film, creating energy densities P up to 10 mJ/cm^2 per pulse. The temporal evolution of the injected strain pulse (Fig 7.1(b)) was calculated using the known methods of ultrafast acoustics and coincides with results from direct conventional pump-probe measurements [76]. In the experiments a nearly symmetric bipolar strain wave packet is injected into the GaAs slab, which can be modeled to a good degree of accuracy by a Gaussian derivative with strain amplitudes reaching $8 \cdot 10^{-4}$ in GaAs for the highest pump intensity (see Fig. 7.1(b)).
To summarize Chapter 2.2, the temporal and spatial evolution of the strain pulse $\eta_P(t, x)$ (where x is the distance from the Al film) depends on P and on the linear and nonlinear elastic properties of the crystal and can be calculated numerically. At low pump excitation densities (W <1 mJ/cm^2), the injected strain pulse propagates linearly through the GaAs slab with the velocity of longitudinal sound and reaches the ZnSe/ZnMgSSe heterostructure at a time $\tau \sim 20$ ns without any sizable distortion. At excitation densities P >1 mJ/cm^2, however, nonlinear elastic effects start to play a role and the injected strain pulse transforms into a more complicated waveform, where at medium fluences $1-3$ mJ/cm^2, the wave transforms into a shockwave. Finally, above 3 mJ/cm^2, notable dispersion effects concerning the high frequency phonon components in the supersonic compressive strain cause a further transformation of the shock front into a train of ultrashort soliton pulses. Figure 7.1(c) shows an example trace for $\eta_P(t, x(\tau))$, calculated for P =10 mJ/cm^2 (for a discussion, see also the strain pulses in Fig. 2.6). The most striking features are the development of acoustic frequencies in the THz range, and the formation of supersonic strain solitons at the front.
The effect of the soliton pulses on the optical response of the QW was studied using optical reflectance spectroscopy. For this, a probe beam was split from the laser beam, passed through a sapphire plate to generate femtosecond white light pulses, and given an optical delay of 20 ns, corresponding to the travel time of the longitudinal strain pulse through the GaAs crystal slab (see also the experimental setup in Fig. 5.1). The probe beam was focused on the front side of the slab to a spot less than 50 μm diameter exactly opposite to the pump spot (Fig. 7.1(a)). The reflected probe beam was collected and analyzed by a spectrometer and CCD camera with the readout synchronized with the scanning optical delay line in the pump beam. The chosen time step δt_d of the variable delay was set to 300 fs.

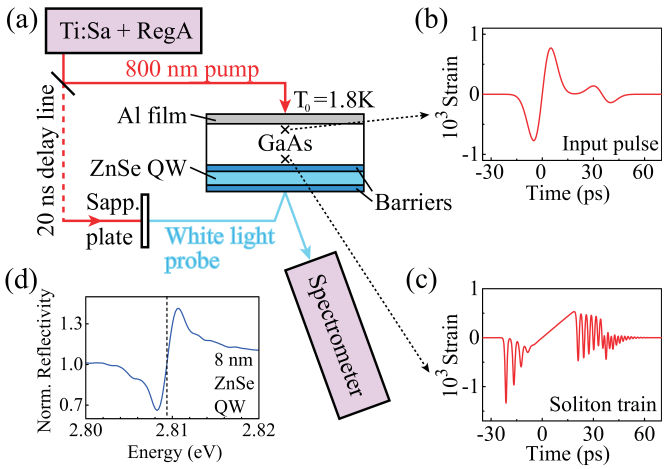

Figure 7.1: (a) Experimental scheme. (b) Calculated strain pulse as initially generated in the metal film for excitation density $P = 10$ mJ/cm^2, and (c) its transformation to a soliton train after propagation through 100 μm of GaAs. The time in (b) is shifted toward that in (c) by the sample traversal time τ. (d) Measured reflectance spectrum of the ZnSe QW heavy hole exciton, normalized to the off-resonance background. The vertical dashed line in (d) shows the energy position of the heavy-hole exciton resonance.

Figure 7.1(d) shows the reflectance spectrum in the absence of a pump pulse in the energy range of the heavy-hole exciton resonance in the QW [75]. The exact shape of the reflectance spectrum is determined by the thickness of the top barrier layer [45]. For the used sample, the reflectance $r_i^{QW}(\omega)$ normalized to the off-resonant background can be described by Equation 3.10.

7.2 Strain Modulated Exciton Resonances

The following investigation mainly focuses on the optical response of the QW heavy-hole exciton resonance, as described in Chapter 3.1.2, when acoustic solitons impact on the structure. To motivate this restriction, Fig. 7.2 shows the time traces of the resonance energy reponse of the heavy-hole (HH, blue triangles) and light-hole (LH, red circles) exciton at *low* excitation density $P = 2$ mJ/cm^2, making it possible to follow easily the strain profile of the impinging acoustic wave. A similar response has been measured earlier [77], relating the unconventional shape of the wave to the incident strain wave from the GaAs slab and the reflected, phase shifted strain from the barrier to liquid helium interface at the position of the QW. Both traces obey the same time dependence with slightly differing absolute values of the induced energy change, which is most likely due to differences in the tetragonal and hydrostatic deformation potential constants of the heavy-hole and light-hole bands (see also discussion in Chapter 3.2). However this difference is small and in the further discussion the light-hole exciton response will be omitted. The results for three values of P are shown in Fig. 7.3 as spectral-temporal contour plots, where the color scheme in each panel of Fig. 7.3 is a measure of the time-dependent reflected spectral intensity normalized to the off-resonant value. The value $t = 0$ corresponds to the arrival time τ of the center of the initial bipolar wave packet (Fig. 7.1(b)) at the QW. Times $t < -25$ ps and $t > 100$ ps correspond to the situation prior to the arrival of the strain wave packet and after full passage of the heterostructure respectively, where no temporal modulation is observed and the reflectance spectrum is equal to the one in the absence of strain, shown in the insets of Fig. 7.3 by a dashed line.

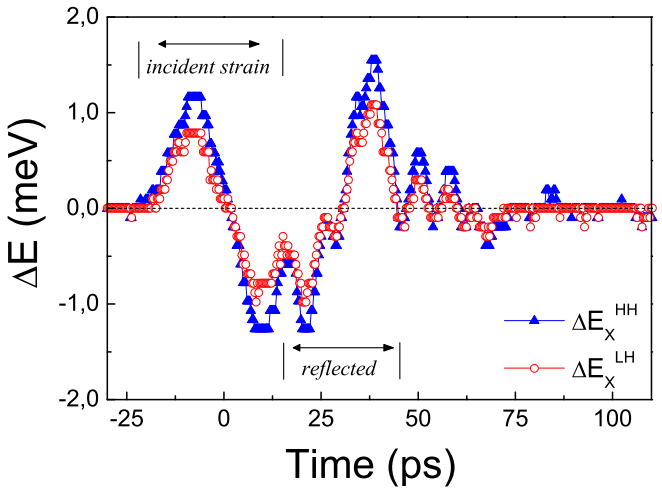

Figure 7.2: Induced energy change concerning the heavy-hole (blue triangles) and light-hole (red circles) exciton resonances at $P = 2$ mJ/cm^2, $T = 1.8$ K. Time intervals where the incident strain from the GaAs slab dominates the response and where the reflected strain from the barrier liquid helium interface adds are indicated as *incident* and *reflected*. The traces obey the same time dependence with close amplitudes.

In the time interval -25 ps $< t <$ 100 ps, however, the measurements show strong responses, that depend on the pump excitation density P. In the linear regime ($P <$1 mJ/cm^2, Fig. 7.3(a)), the optical response essentially tracks the temporal evolution of the exciton resonance according to the strain profile of the acoustic wave. The important point here is that the exciton resonance does not change its shape but simply shifts to different energies (compare solid and dashed lines in the inset of Fig. 7.3(a)). The strain-induced shift of the exciton resonance $\Delta E(t)$ in this case might be approximated by $\Delta E(t) = a\eta_{QW}(t)$ (see Chapter 3.2), where a denotes the net deformation potential constant). The time dependent strain in the QW $\eta_{QW}(t) = \eta_0(t) - \eta_0(t - t_r)$ consists of the sum of the pulse $\eta_0(t)$ incident from the GaAs slab, and its reflection $\eta_0(t - t_r)$ from the sample to liquid-helium interface, arriving a time $t_r = 2l_r/v_{ZnSe}$ later ($l_r = 50$ nm is the distance from the QW to the surface, and $v_{ZnSe} = 4000$ m/s is the mean longitudinal sound velocity in the ZnSe/ZnMgSSe heterostructure [78]), both indicated in Fig. 7.2. The minus sign in the reflected wave is due to the phase jump of π at a free surface. Huge changes in the time-resolved reflectance spectra are observed for higher P (Figs. 7.3(b) and 7.3(c)): (i) sharp features in the temporal signal appear, (ii) the leading edge of the detected signal shifts to earlier times with the increase of P, (iii) the spectrum broadens strongly (inset Fig. 7.3(b)), and (iv) doublet structures appear at certain times t (inset Fig. 7.3(c)). Features (i) and (ii) point to acoustic solitons arriving at the QW, which might become shorter than 1 ps (see Fig. 7.1(c)), explaining the sharp features in the temporal evolution of the detected signal at high P. Furthermore, the soliton velocity is supersonic, which results in the early arrival of the front of the strain wave packet, as observed in [27][73][14]. The arrival times, corresponding to the first energy maximum due to the incident strain wave (see Fig. 7.2), are shown in Fig. 7.4 (lower panel). It is clearly seen, that at excitation densities P exceeding 4 mJ/cm^2 the arrival time notably shifts to earlier times t until reaching the earliest measured relative arrival times of -8 ps. This time corresponds

to a net change of soundspeed in the GaAs slab of $\Delta\tilde{v}_{GaAs} \sim 2$ m/s, i.e. an increase of 0.4%. Note that the true soliton speed is even higher since the transformation process into the split off solitons is not an instantaneous one. Note also that at high exitation densities P the readout becomes difficult due to the strong chirp of the resonance.

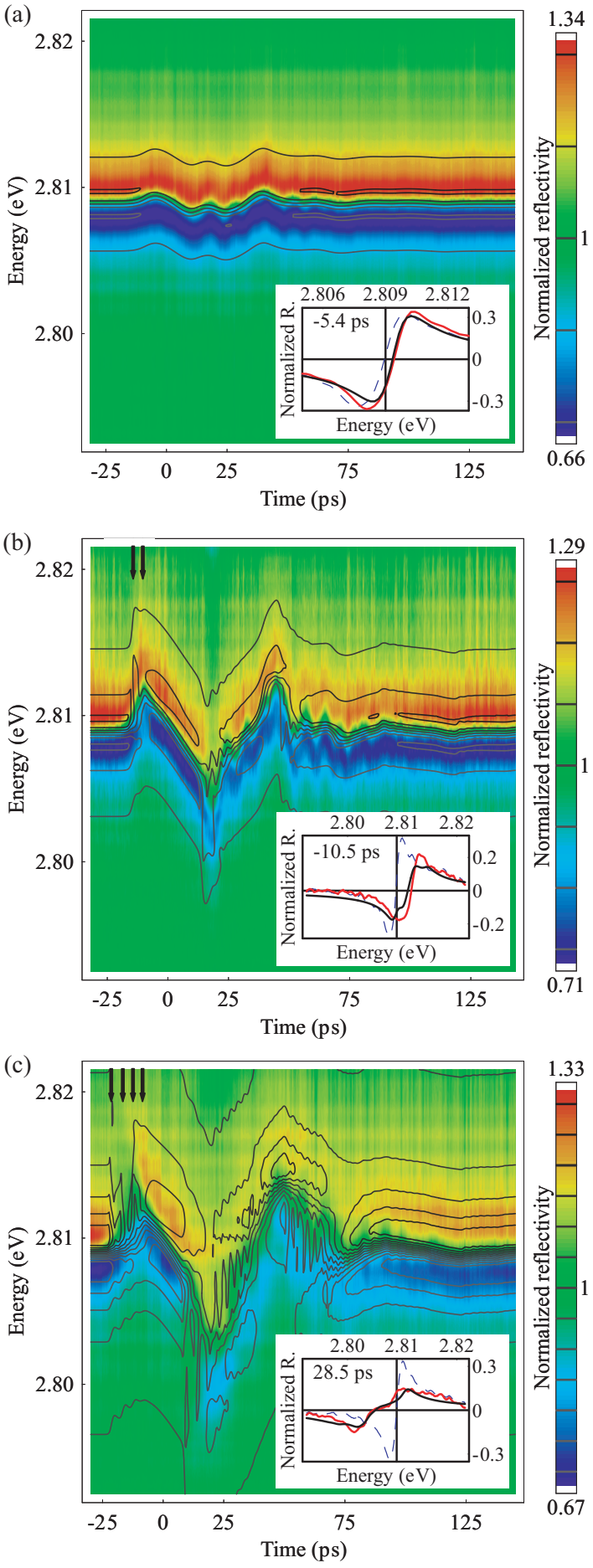

Figure 7.3: Spectral-temporal contour plots of the reflectance normalized to the off-resonance background, measured for pump fluences of (a) 1 mJ/cm^2, (b) 5.1 mJ/cm^2, and (c) 10.2 mJ/cm^2. Black lines are calculated contours of equal reflectance changes for corresponding pump fluences. Insets show the spectral profiles of reflectance: the blue dashed line is the stationary spectrum, the red and black lines are, respectively, the measured and calculated spectra at the specified time, for the corresponding fluence. Black arrows in (b) and (c) indicate the arrival time of individual solitons at the QW center.

7.3 Discussion and Analysis

To understand the optical response on a quantitative level, the temporal evolution $\Delta E(t)$ of the exciton resonance upon passage of a soliton train was calculated [29]. The shape of the strain wave thereby was calculated according to Chapter 2.2.

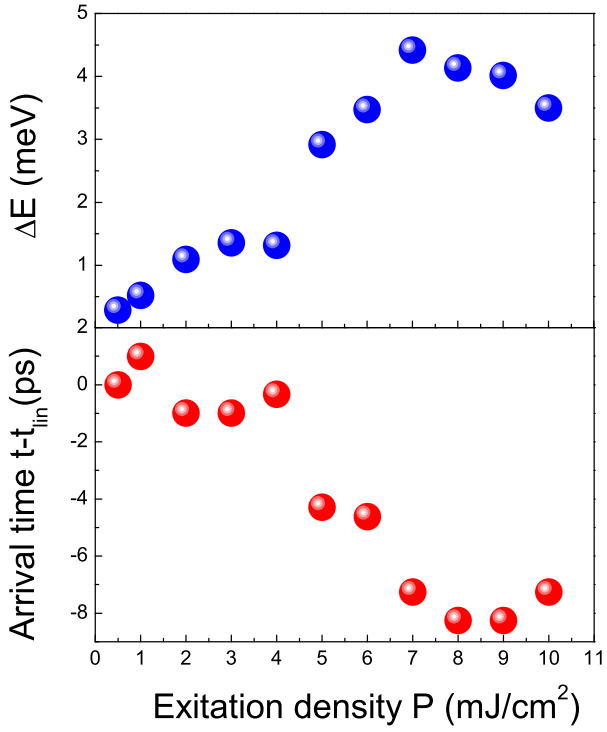

Figure 7.4: Dependence of the arrival time (lower panel) and the energy shift (upper panel) of the first response maximum due to the incident strain wave. The arrival times are related to travel time $\tau = t_{lin}$ of the linear strain pulse at an excitation density on the metal transducer of $P = 0.5$ mJ/cm^2.

Because of the small distance between the QW and the surface, the temporal shapes of the incident and reflected strain pulses are taken identical except for the phase jump (see also [77]). It turnes out that in the soliton regime the spatial strain variations become so short, that the QW no longer can be considered as an infinitely narrow object as might be true for the linear regime. Taking account for the QW extension within the the approximation of infinitively high barriers the electron wave function might be written as $\phi(x') = \sqrt{2/d}\,\cos(\pi x'/d)$ ($x' = 0$ at the center of the QW). The finite size restricts the time resolution to the travel time through the QW $d/v_{ZnSe} \sim 2$ ps, and limits the sensitivity for very short soliton pulses, where the energy is concentrated mostly in the high-frequency components. For illustration the relation between a single soliton spatial extension ($P = 10$ mJ/cm^2) and the quantum well electronic (similar for the hole) probability distribution $|\phi|^2$ is shown in Figure 7.5.

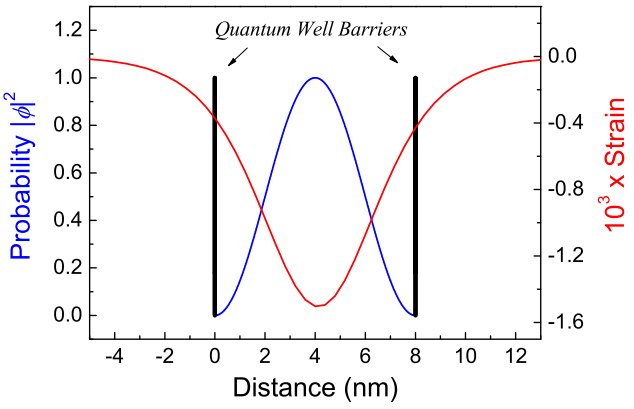

Figure 7.5: QW electronic probability distribution $|\phi|^2$ (blue curve) in the infinetly high barrier approximation and spatial strain profile of the leading single soliton at an excitation density $P = 10$ mJ/cm^2 (see Fig. 7.1(c)). Thick vertical black lines indicate the QW barrier positions.

Clearly the strain amplitude is only a local feature within the QW implying a response of the electron (and hole) based on a covolution ansatz concerning the strain and the electronic wavefunction. Assuming that the strain does not change the potential profile of the QW significantly, perturbation theory gives the energy shift of the exciton resonance in the QW in the presence of the strain pulse as the convolution

$$\Delta E(t) = a \int_{-d/2}^{d/2} |\phi(x')|^2 \eta_{QW}^P(t, x') dx' \tag{7.1}$$

Note that Equation 7.1 is reminiscent of the equation of matrix elements for the exciton-phonon interaction in a QW [79] that indeed shows a cutoff for high-frequency phonons.

The interaction of the probe light with the exciton system is inherently not instantaneous but takes the exciton coherence time τ_c, which in high-quality QWs at low temperatures is close to twice the value of the radiative exciton lifetime [80] and is longer than the duration of the probe pulse and the strain soliton pulses. Thus a spectral broadening and a shift of the exciton resonance are induced by the strain profile arriving at the QW up to a coherence time τ_c after the incident probe pulse. This is illustrated in Fig. 5.2 where the modulation of the polarisation decay after the optical probe pulse becomes obvious. The overall measured spectrum at time t though is composed from the chirped (i.e. frequency modulated) polarisation decay. To compute the spectra $R(E, t)$ at time t, a further convolution was performed:

$$R(E, t) = \frac{1}{\tau_c} \int_t^\infty r_{QW}[E - \Delta E(\tilde{\tau})] \exp\left(-\frac{\tilde{\tau} - t}{\tau_c}\right) d\tilde{\tau} \tag{7.2}$$

where $r(E)$ and $\Delta E(\tilde{\tau})$ are given by Eqs. 3.10 and 7.1, respectively. In the calculations [29] of the optical resonance response, the best agreement concerning the energy shifts is obtained for $a = -8$ eV [29]. A dependence of the measured values for the first higher energy shift ΔE from the excitation energy density P is shown in Fig. 7.4 (upper

panel). The saturation at high P is likely to be due to difficulties in the determination of the exact energy position (see Fig. 7.3(c)) as well as to the reduced sensitivity of the QW to very high strain derivatives i.e. very high frequency components. Further $\tau_c = 4.6 \pm 1.3$ ps [29], close to the measured dephasing time of excitons in similar QWs [81]. The results of the numerical calculations for three values of P are shown in Figs. 7.3(a) and 7.3(c) as solid contour lines of equal reflectance. Good agreement between the experiment and simulations is seen. The sharpening of the leading edges at elevated P signifies the formation of ultrashort strain pulses, i.e., solitons, indicated by arrows in Figs. 7.3(b) and 7.3(c). The arrival time of the solitons decreases with the increase of P (Fig. 7.4), as correctly described by the simulations.
The inset of Fig. 7.3(b) shows a typical chirped spectrum at the time of passage of a soliton, which has clearly induced both a shift and significant broadening. The simulations and experiments at the highest energy density show individual soliton pulses, which, however, are not clearly separable. The passage of incident and reflected solitons leads to strong spectral broadening over a large range of times, visible as an increase in green areas in Fig. 7.3(c). The reasons for this are that both the duration of individual soliton pulses and the time separation between different soliton pulses are shorter than τ_c. Thus as soon as the soliton train arrives, the exciton resonance is driven several times back and forth during its coherence time τ_c.
An even more elucidating example is presented in the inset in Fig. 7.3(c), which shows a clear doublet structure that can be observed around $t = 28$ ps and might be explained by the tensile part of the incident wave, shown in Fig. 7.1(b). Here, a dispersive tail develops of both high frequency and high amplitude (Fig. 7.1(c)). Within the time τ_c, the excitons are swept in energy over several meV a couple of times. One can qualitatively understand the origin of the doublet by making the analogy with a pendulum, which spends most of the time in its extreme positions. At high P both experiment and theory show that $\Delta E(t)$ reaches 10 meV (Fig. 7.3(c) at $t = 20$ ps and reveal that the reflected pulse induces higher excursions relative to the incident one. This experimental observation, which is absent for low P, is due to the circumstance that the whole strain wave spreads in time and the first soliton pulse reflected from the surface and the tensile part of the incident pulse train meet in the QW and interfere constructively, similar to coherent strain control like reported in [82]. All experimental results presented in Fig. 7.3 show minor amplitude oscillations with a period ~ 10 ps after passage of the incident pulse which are not present in the simulated curves, and are not understood yet. It might be speculated that this oscillations are due to elasto-optic effects similar to that discussed in Chapter 6, which have not been considered in the numerical calculation.

7.4 Outlook

The soliton-induced effects in more sophisticated nanostructures (e.g., tunneling devices, shallow QWs, quantum wires, dots, and molecules), where the adiabatic approximation for electron and lattice systems is not valid anymore, may lead to the discovery

of new and ultrafast phenomena at constant carrier densities. An example of such a diabatic modulation process will be discussed in the next Chapter 8, where indeed new clear chirping features show up in the frequency modulated spectra, which indicate a modulation much faster than the respective coherence time of the optical transition. The experiments and theoretical analysis have shown, that the effect of acoustic solitons on the electronic states may be used as an ultrafast method for modulating the optical response in nanostructures. The large value of the energy resonance shift may become a basis for picosecond control of emission from nanophotonic devices (semiconductor microcavities, 2D arrays, etc.), and will be demonstrated in a first attempt in Chapter 10.

8 Generation of Terahertz Sidebands in a Planar Quantum Well Cavity

WHERE in the previous two Chapters 6 and 7 the impact of an acoustic pulse on the optical properties of a Bragg resonator and a single quantum well have been reported, and a fundamental understanding of these structures has been gained separately, in the following chapter a single quantum well will be placed within the central layer of a Bragg resonator. The combined quantum well-cavity system is in the regime of strong light matter interaction, as basically described in Chapter 3.1.3.
It will be demonstrated, that a fast modulation process might cause new significant spectral features, which can be related to the modulation process itself. Here the generation of terahertz sidebands, due to fast and strong energy modulation of a detuned quantum well cavity lower polariton resonance is reported. In particular the regime of resonance chirping treated in Chapter 7, will be further extended to a clear diabatic modulation of a sharp lorentz like resonance [50].

8.1 Introduction

Manipulation on ever faster time scales has led to enormous progress in basic and applied research. These advancements in ultrafast control have been based mostly on the availability of ultrafast laser sources, which may provide coherent light pulses with durations as short as attoseconds [83]. In parallel the field of ultrafast acoustics has been developed towards terahertz frequencies (see Chapter 2). Recently efforts have been undertaken to merge the fields of ultrafast optics and acoustics resulting in a variety of novel acousto-optic phenomena. Among them are the generation of THz radiation by acoustic waves [84], the amplification of THz sound waves in a combined optical and phonon microcavity [65], strain pulse induced chirping of an optical transition (Chapter 7) [29] as well as the switching of an optical microcavity resonance (Chapter 6) [51].
Here the ultrafast acoustics techniques used in the previous chapters are applied to a semiconductor quantum well microcavity in the strong-coupling regime. By injecting terahertz strain pulses a modulation domain can be obtained in which large variations in the optical frequency are induced on time scales shorter than the polariton decoherence. Under these conditions characteristic sidebands which are spectral fingerprints of

the terahertz modulation process appear in the spectrum near the polariton resonance.

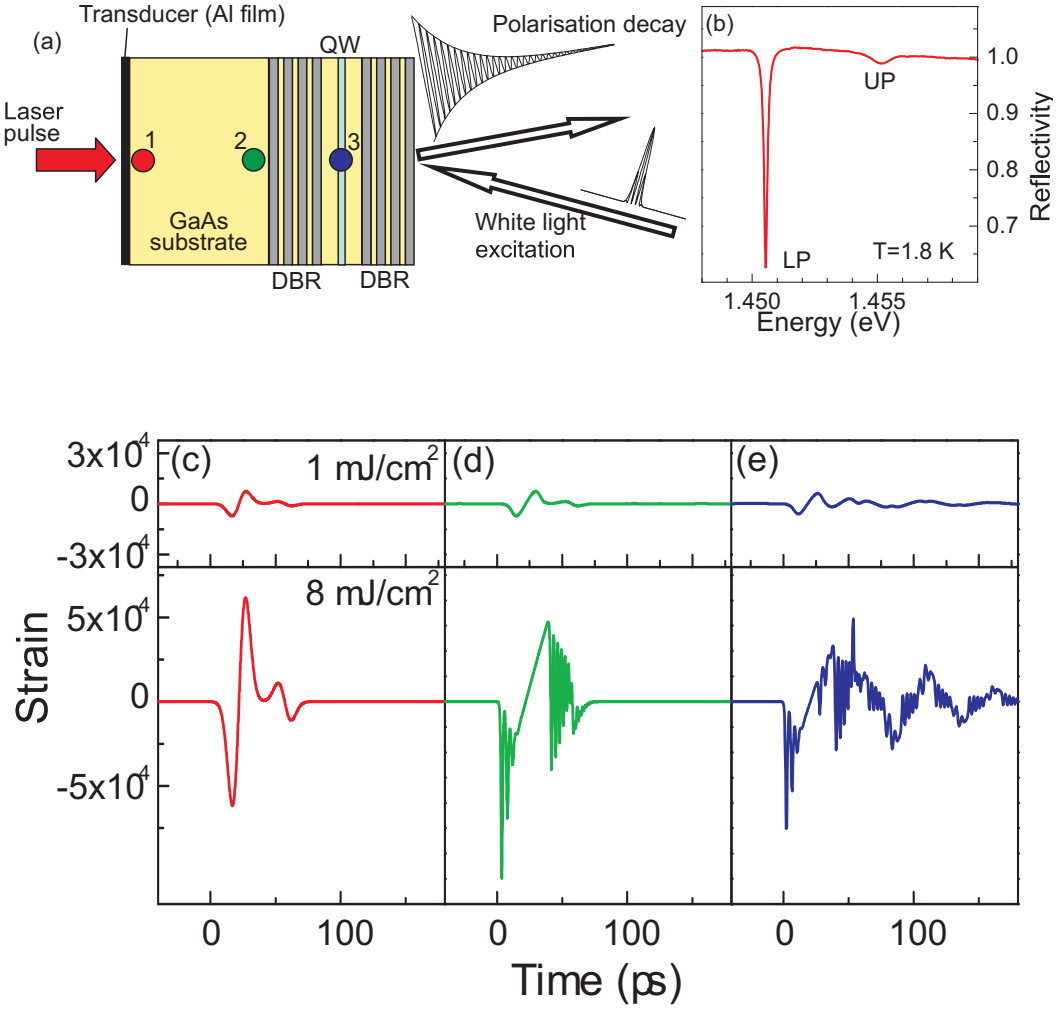

Figure 8.1: Experimental principles of modulation. (a) Scheme of the experiments on a microcavity formed by two distributed Bragg reflector mirrors (DBR) with a quantum well embedded in between. The strain pulses are generated by a laser pulse shown by a red arrow, focused onto an aluminum film. (b) Reflectance spectrum from the microcavity without modulation. LP and UP: spectral resonances of the lower polariton and upper polariton respectively. (c-e) Strain pulses $\eta(t)$ simulated for low (upper panels) and high (lower panels) excitation densities P at various distances (indicated by the spots 1-3 in panel (a)) from the aluminum transducer. the propagation time from the transducer to the corresponding points was subtracted for clarity.

It is well-known that traditional MHz and GHz acoustics allows efficient modulation of the optical frequency ω, such that the variations $\Delta\Omega$ of the modulation amplitude are large enough to be seen in the spectrum of the optical signal [85][86]. When the modulation of the signal occurs on a time scale τ_a (the time that it takes the optical frequency to reach maximum modulation $\Delta\Omega$, which is much longer than the coherence time τ_c, it is easily possible to follow the time dependence of the modulated optical frequency $\omega(t)$ from the emitted (reflected) light intensity, as the modulation occurs adiabatically. For semiconductors, for example, modulation frequencies τ_a^{-1} in the GHz

regime could be achieved corresponding to τ_a exceeding by far the typical coherence times $\tau_c \sim 10^{-12} - 10^{-11}$ s in these systems. In this case the existing time-resolved methodologies using linear or nonlinear spectroscopy are fully sufficient to track the optical frequency modulation $\omega(t)$ [77].
Tracing $\omega(t)$ from the spectrum is hampered, however, when τ_a is clearly shorter than τ_c and simultaneously the perturbation is so strong that the modulation amplitude $\Delta\Omega$ exceeds by far the stationary spectral width $\Delta\omega \sim \tau_c^{-1}$. This situation is implemented here in a system for which the adiabatic regime is left by applying an ultrafast acoustics technique. The diabatic situation, with which one is confronted then, is characterized by

$$\tau_a \leq \tau_c \text{ and } \Delta\Omega > \Delta\omega \tag{8.1}$$

In the following ultrafast strain pulses are applied to a semiconductor microcavity (MC) in the strong-coupling regime showing coherent emission over comparatively long times. Insight into the diabatic regime might be obtained by analyzing the optical signal in the spectral domain. Where intuitively such a spectral analysis appears to be inappropriate, since all information about the modulation process should be blurred by signal integration over times essentially longer than τ_a, it will be shown that contrary the experimentally obtained spectra contain clear signatures of the microcavity resonance modulation. In agreement with a theoretical model [50] it will be demonstrated that in the diabatic regime pronounced sidebands of the modulated resonance appear, from which information about the modulation process might be obtained.

8.2 Experiment and Sample

The basic scheme of the experiments which were carried out at liquid-helium temperature ($T = 1.8$ K) is shown in Fig. 8.1. The high quality optical MC structure (panel (a)) contains an 8-nm-wide $In_{0.04}Ga_{0.96}As$ quantum well (QW) in the middle of a GaAs cavity layer of width d=240 nm, corresponding to the wavelength λ of the confined photon resonance. This λ-cavity layer is surrounded by distributed Bragg reflectors built from 24 and 20 pairs of GaAs/AlAs $\lambda/4$ stacks at the bottom (toward subtrate) and the top (toward vacuum), respectively. The Q factor of the MC is $\sim 10^4$, leading to the strong-coupling (polariton) regime between the QW exciton state and the confined photon mode [46][87]. Figure 8.1(b) shows the stationary optical reflectance spectrum $R(E)$ of the MC in which two narrow resonances corresponding to the lower (LP) and upper (UP) polaritons are seen. The photonlike LP resonance is slightly broadened relatively to the cavity mode, and shows a spectral width $\Delta\omega = 0.18$ meV.
In the ultrafast coherent experiments the polariton resonances were excited by 150 fs white light pulses from a laser system with a repetition rate 100 kHz. The beam was focused on the sample surface of the MC to a spot with a diameter 100 μm. As a result of the femtosecond broadband excitation, the LP and UP states emit coherent light into the specular direction relative to the excitation beam (Fig. 8.1(a)). The amplitude of the reflected light decays within a time τ_c corresponding to the coherent polarisation decay of the resonances. The value of τ_c is connected with the spectral

width of the resonance $\Delta\omega$ by the following relation:

$$\tau_c = \frac{2}{\Delta\omega}, \tag{8.2}$$

where the factor 2 arises from the fact that τ_c corresponds to the decay of the electromagnetic field amplitude, while the spectral width of the optical resonance reflects the decay of the field intensity. The value of τ_c for the LP resonance obtained from the optical spectrum using Equation 8.2 is equal to 7.2 ps.

The THz frequency modulation is achieved using strain pulses, injected into the sample via a metal transducer as described in Chapter 2.2. The strain pulses are generated by excitation of a 100 nm thin Al film deposited on the GaAs substrate opposite to the MC by 800 nm femtosecond light pulses, taken from the same laser system as the white light pulse (Figs. 8.1(a), 5.1). The energy density of the excitation laser pulse thereby could be increased up to $P = 16$ mJ/cm^2, which corresponds to a maximum strain amplitude of $\eta_0 \sim 10^{-3}$ [29][77].

The strain pulses propagate through the 100 μm (001)-oriented GaAs substrate with the velocity $c_{LA} \sim 4800$ m/s of longitudinal sound in GaAs [58]. Accordingly the strain pulses reach the MC with a delay of about 20 ns relative to the 800 nm excitation pulse. The temporal shape of the strain pulse reaching the MC strongly depends on the excitation density on the transducer (see Chapter 2.2). At low excitation densities $P < 1$ mJ/cm^2 the shape of the pulse does not change significantly while propagating through the substrate (compare upper panels (c) and (d) of Fig. 8.1). At higher P nonlinear elasticity and the phonon dispersion become important and the pulse shape is modified during propagation. This results in the formation of a shockwave and, at low temperatures, an acoustic soliton train at the beginning of the strain pulse, while at its end dispersive phonon oscillations take place [27]. The temporal evolution of the strain pulse for this nonlinear regime, shown in the lower panel of 8.1(d) was calculated numerically [29]. Further modifications (Fig. 8.1(e)) of the strain pulse reaching the QW are due to multiple reflections at the interfaces of the MC structure [88].

The strain pulse $\eta(t)$ arriving at the QW modulates the detuning $\Delta_d = E_x - E_c$ between the energies of the uncoupled cavity mode and exciton, E_c and E_x, respectively (see Chapter 3.1.3) where the effect of the strain pulse on E_x is significantly stronger than on E_c [51][29] as can be deduced easily from Chapters 6 and 7. However small oscillations are visible in the LP spectrum before the strain pulse reaches the QW (see Fig.8.5) from which, according to Chapter 6, a sound speed in the superlattice of ~ 5250 m/s can be deduced. This value is well between the known values for GaAs (4800 m/s [58]) and AlAs (6400 m/s [89]) as expected for a periodic structure [7] (compare also Fig. 3.8(b)). The lower amplitude compared to Chapter 6 most likely is due to the larger optical dimensions of a III-V cavity compared to the strain pulse spatial extension (indicated by the photonic resonance wavelength). Further the different elasto-optic response [90] as well as the fact that the polariton energy response to the cavity shift is smaller than the pure cavity shift (Fig. 3.7) lead to the observed differences.

The strain pulse now induces a time-dependent detuning $\Delta_d(t) = a\eta(t) + \Delta_d^0$, where

$a \sim -10$ meV is the deformation potential of the exciton in the (In,Ga)As/GaAs QW [91] (see Chapter 3.2) and $\Delta_d^0 = 3.3$ meV is the detuning without applied strain. Using the dependence of the polariton energy on the detuning (Fig. 3.7), the corresponding energy shift concerning the polariton resonances within the coherence time τ_c can be estimated. For instance in the time interval 10 ps $< t <$ 25 ps shifts of the LP resonance within $\tau_c = 7.2$ ps of 0.15 meV and 0.37 meV for $P = 1$ mJ/cm^2 and $P = 8$ mJ/cm^2 respectively, are expected. Thus the effect of a strain pulse with sufficiently high amplitude on the polariton resonance energies turns out to be well suited to reach a diabatic optical modulation regime at THz frequencies under consideration of the relations 8.1.

8.3 Diabatic Frequency Modulation

In the experiments, the spectrum of the coherent polariton emission was analyzed by a spectrometer with a resolution of 0.16 meV and monitored as function of the time delay t_0 ($t_0 = t_{exc}$ from Chapter 5) between the white light excitation pulse and the strain pulse at the QW. The results are shown in Fig. 8.2 for the UP (panel(s)) and LP (panels (b) and (c)). The polariton spectrum, which under stationary conditions consists of the well defined UP and LP resonances (Fig. 8.1(b)), undergoes enormous changes when the strain pulse is hitting the QW. THz modulation of the UP energy (panel (a)) by several meV occurs. Regardless of the smaller LP modulation amplitude (panels (b) and (c)), for certain values of the delay t_0, the LP spectra show a remarkable, well defined structure with spectral fringes at the flanks of the main resonance. The most pronounced sidebands with up to three fringes are observed for high amplitude strain pulses (panel (b)) in the delay intervals $t_0 = 10$ to 25 ps and $t_0 = 90$ to 105 ps, which correspond to the linear parts of the strain evolution (lower panel (e) of Fig. 8.1). Figure 8.2(b) shows the reflectance spectrum $R(t, E)$ for a delay $t_0 = 17$ ps, at which several fringes are clearly detected.
The observed spectral sidebands can be related to the characteristics of the diabatic THz optical frequency modulation. To illustrate that this observation is a general phenomenon, a scalar harmonic oscillator is considered, decaying with time τ_c, which can be described by a time dependent variable $x(t)$ following the equation of motion:

$$\frac{d^2x}{dt^2} = -\omega_0^2(t)x - \frac{2}{\tau_c}\frac{dx}{dt} + f(t - t_0). \tag{8.3}$$

Here $\omega_0(t)$ denotes its time varying frequency and $f(t - t_0)$ is a short excitation pulse acting on the oscillator at time $t = t_0$. The quantities $\omega_0(t)$ and $f(t-t_0)$ are associated with the optical polariton frequency and white light excitation, respectively, and $x(t)$ is the polariton field. The scales, values, and initial conditions for solving Eqn. 8.3 are chosen in accordance with the experiments. The Fourier-transformed (FT) power spectrum of $x(t)$ for the case when $\omega_0(t)$ is increasing linearly with t is shown in the contour plot in Fig. 8.3(a) as a function of t_0. A high-energy sideband with well resolved spectral fringes is clearly seen. The sidebands can be also seen in Fig. 8.3(b)

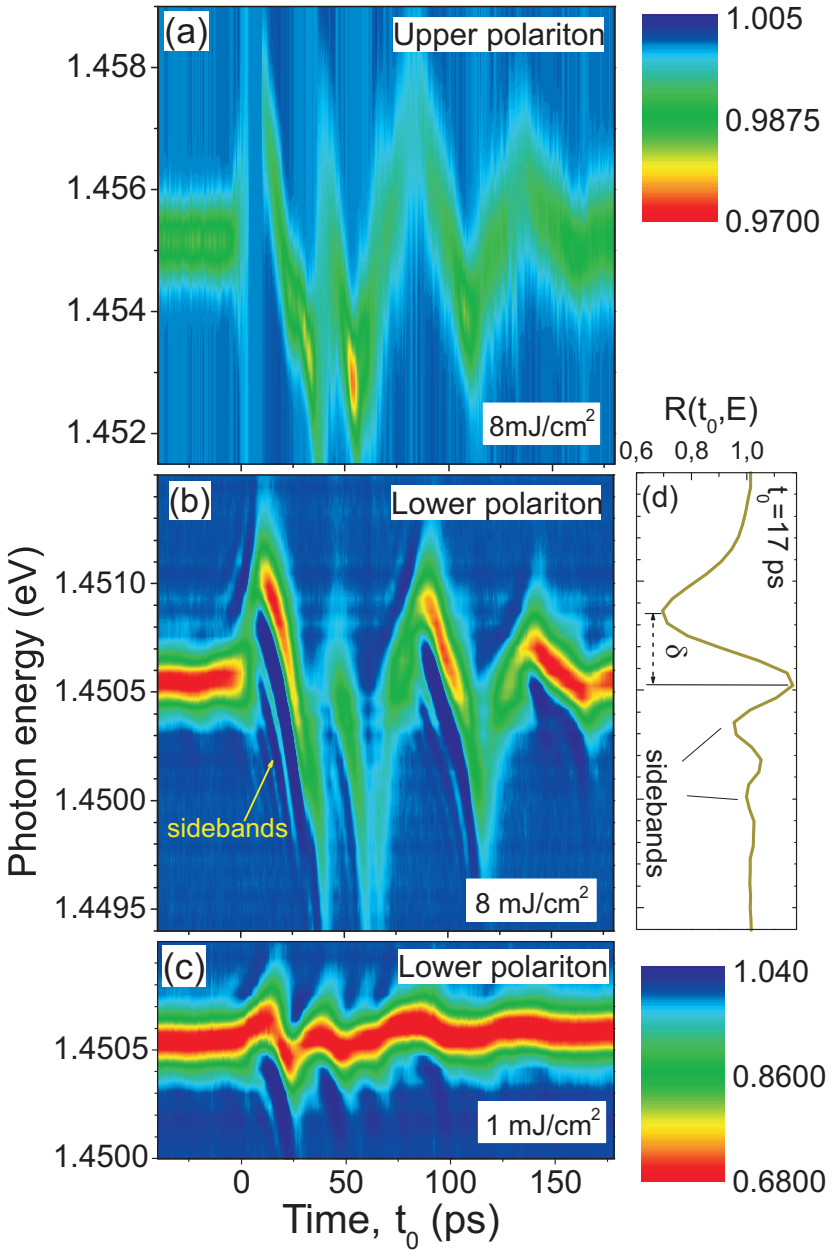

Figure 8.2: Experimental spectral/temporal contour plots. The modulated UP (a) and LP (b,c) optical signals measured at high (a,b) and low (c) excitation densities P focused onto the metal transducer. Panels (b) and (c) have the same intensity scale, which is shown on the right side of (c). (d) Spectrum measured at delay $t_0 = 17$ ps between the arrival of the strain pulse at the MC and the white light pulse.

which shows the spectrum obtained at a fixed delay of $t_0 = 10$ ps. Besides these sidebands, the typical feature in the time-integrated spectra for delay t_0 is the shift in the spectral density maximum to higher energies with respect to $\omega_0(t)$, which is shown in Fig. 8.3(a) by the dashed white line. In case when ω_0 is decreasing with t_0 the spectral density maximum is shifted to lower energies relative to ω_0 and the sidebands appear on the low-frequency side of the stationary resonance position.
Figure 8.3(c) shows the normalized positions $\beta = \tau_c(\tilde{\omega}_m - \omega_0)$ of the sideband maxima of the modulated signal at frequencies $\tilde{\omega}_m$ as a function of the dimensionless parameter $\tilde{w} = \tau_c^2(d\omega_0/dt)$, which is the ratio of the frequency shift during the coherence time τ_c and the half of the resonances spectral width τ_c^{-1}. The maxima positions are seen to be proportional to $\tilde{w}^{1/2}$. The symbols indicate the values of $\tilde{w}$ below of which the corresponding fringe does not appear as a maximum in the spectrum. From Fig. 8.3(c) it is seen, that the value must be higher than 0.25 to have at least one additional maximum. According to the theory the sidebands in our experiments will become well pronounced if the shift in a polariton resonance within the coherence time τ_c exceeds $\Delta\omega/8 = 0.0225$ meV. Such conditions are obviously realized in the detected signals shown in Fig. 8.2. Note that the same evaluation for the structure discussed in Chapter 6 yields a minimum necessary energy shift of the cavity mode of 0.15 meV within the coherence time ~ 2 ps, which is not achieved.

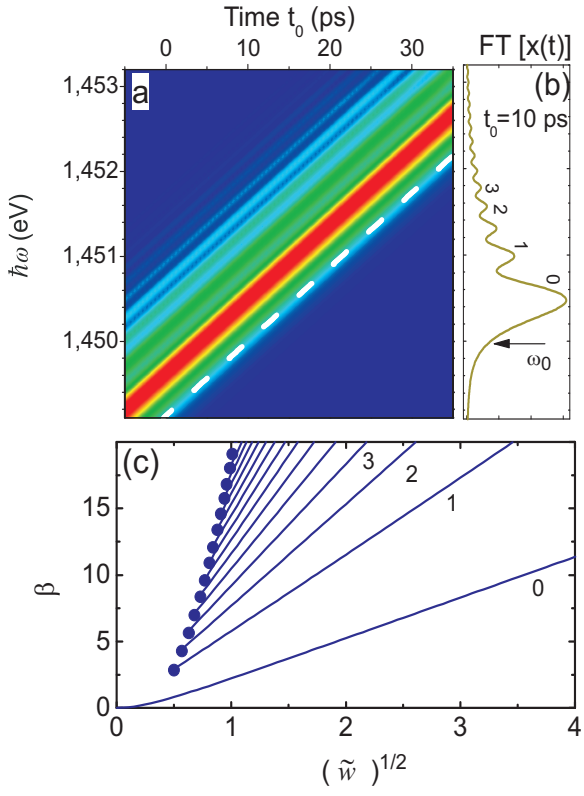

Figure 8.3: Calculations of the modulated spectrum of a scalar oscillator excited by a broad band excitation pulse in a situation when the resonance energy changes linearly with time: (a) spectral/temporal contour plot of the power Fourier-transformed time-dependent variable $x(t)$, ω_0 is shown by the dashed line; (b)oscillator power spectrum for t_0=10 ps; (c) normalized positions β of the sideband maxima as function of the parameter $\tilde{w}$, which characterizes the modulation rate. Symbols indicate the values below of which the corresponding maximum cannot be observed.

8.4 Model Calculation

The model presented above demonstrates the general idea of the diabatic approach. To become more quantitative, a specific analysis has been performed for the MC studied here [50], which will be given here for illustration.
The strain pulse results in a time-dependent modulation of the exciton energy $E_x(t)$, which is observed as a shift in the polariton resonances in the strong-coupling regime. Because the amplitude of the exciton shift $\Delta E_x(t)$ exceeds the polariton Rabi splitting the adequate description cannot be obtained within the single (lower or upper) polariton branch approximation. Instead direct solution of the Maxwell equations with a time dependent exciton resonance is necessary. If the spectral range of interest is narrow compared to the stop band of the cavity Bragg mirrors the resonant approximation of cavity electrodynamics can be used [92][93]. Within this approximation the Maxwell equations are reduced to a system of two coupled equations that describe the dynamics of the cavity mode electric field at the quantum well $\epsilon_{QW}(k,t)$

$$\left[i\frac{d}{dt} - E_c(k)\right]\epsilon_{QW}(k,t) = \gamma(k)\sum_i P^i(k,t) + \alpha(k)\epsilon_{inc}(k,t), \tag{8.4}$$

and of the resonant exciton polarization, integrated over the thickness of the quantum well $P(k,t)$

$$\left[i\frac{d}{dt} - E_x^i(t)\right]P^i(k,t) = A^i\epsilon_{QW}(k,t). \tag{8.5}$$

Here E_c and E_x are the resonance energies with nonzero imaginary parts due to the decay of the cavity mode and exciton dephasing, respectively. A is the magnitude of the quantum well exciton resonance susceptibility, α and γ are the coupling constants of the microcavity electromagnetic field with the external field and the QW exciton polarization, respectively. The polariton Rabi splitting Ω_R can be calculated from $\Omega_R = \sqrt{A\gamma}$. The incident pulse far from the microcavity $\epsilon_{inc} = \epsilon(t)\exp(-i\Omega_{inc}t)\delta(k - k_{inc})$ is assumed to have the form of a plane wave with energy Ω_{inc} and in-plain wave vector $k_{inc} = \Omega_{inc}/c$, $\epsilon(t)$ is the electric field amplitude of the excitation pulse, which in the calculations is assumed to have a Gaussian shape with a duration of 100 fs. The summation over the partial polarizations P^i is introduced in Equation 8.4 in order to take into account the inhomogeneous broadening of the exciton line, which is described by the distribution of $E_x^i(t)$ and A^i. The cavity resonance energy E_c and the coupling constants α and γ are calculated in the scattering matrix formalism [92] by solving the Maxwell equations for the particular cavity geometry and analyzing the poles of the scattering matrix in the complex energy plane [93]. The solution of Eqs. 8.4 and 8.5 yields the dynamics of the cavity electromagnetic field $\epsilon_{QW}(t)$, which depends strongly on the delay between the incident pulse $\epsilon_{inc}(t)$ and the exciton resonance modulation $E_x(t)$ due to the strain pulse. The temporal shape of the pulse reflected from the MC, ϵ_{refl} can be found in the same resonant approximation from

$$\epsilon_{refl}(k,t) = \frac{\epsilon_{QW}(k,t) - T^{inc}(k)\epsilon_{inc}(k,t)}{T^{refl}}, \tag{8.6}$$

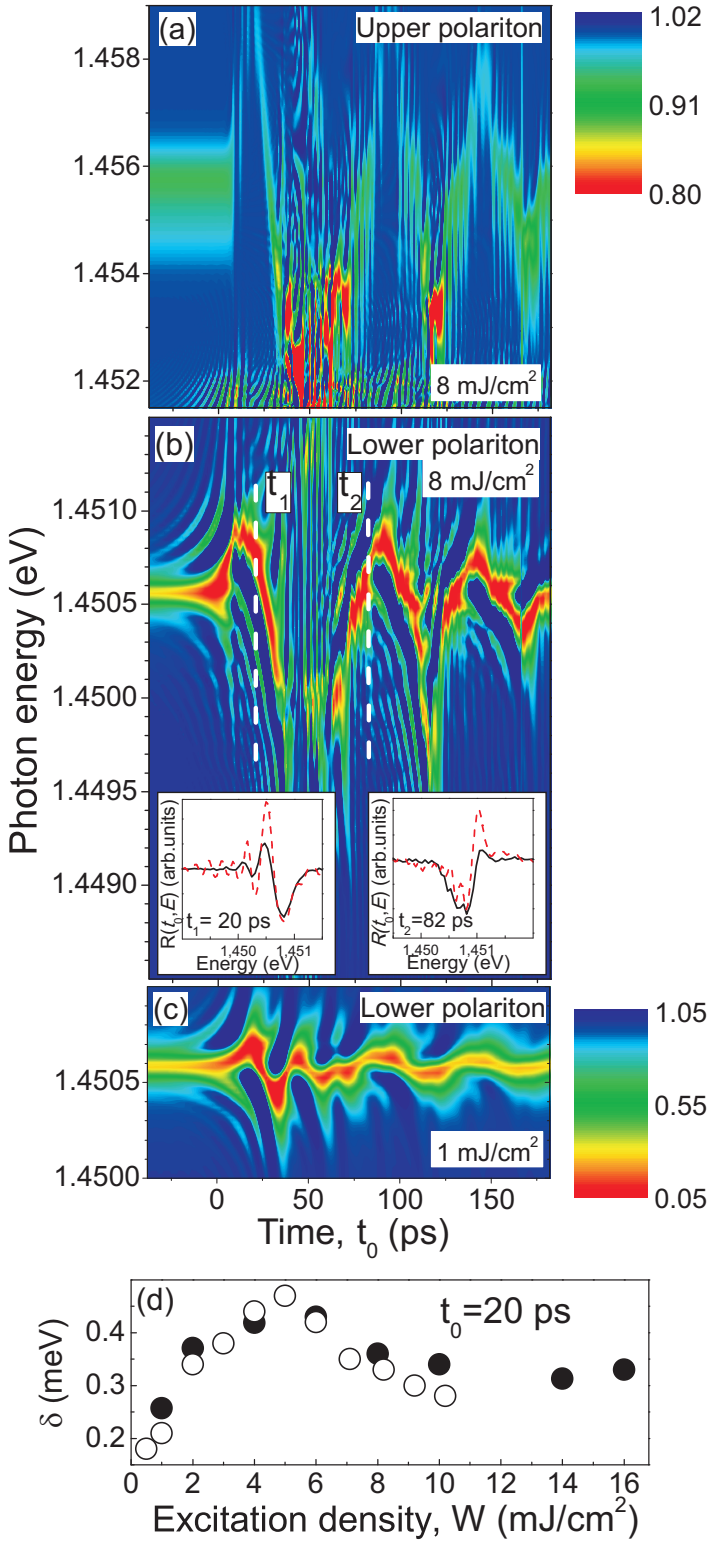

Figure 8.4: Theoretical analysis of the polariton sidebands. (a-c) Spectral/temporal contour plots of the modulated UP (a) and LP (b,c) optical signals calculated for high (a,b) and low (c) excitation densities P. Panels (b) and (c) have the same intensity scale, which is shown on the right of (c). Insets in (b) are normalized measured (solid lines) and calculated (dashed lines) spectral profiles obtained for two delay times t_1 and t_2. (d) Spectral separation δ (bar in Fig. 8.2(d)) between the first minimum and first maximum in the sideband spectrum of the LP modulated reflectance signal, as measured (closed symbols) and calculated (open symbols) for t_0=20 ps.

with the coefficients $T^{inc}(k)$ annd $T^{refl}(k)$, which are calculated from Maxwell's equations and depend on the microcavity design.
The temporal variation in the reflected pulse $\epsilon_{refl}(k,t)$ is obtained from Eqn. 8.6 for given $\epsilon_{inc}(k,t)$ and $\epsilon_{QW}(k,t)$, calculated from Equations 8.4 and 8.5 for a particular delay between ϵ_{inc} and $E_x(t)$. The spectra of the reflected and incident pulses are obtained by Fourier transformation and the time integrated reflectance spectrum is calculated as $|r(\omega)|^2 = |\epsilon_{refl}(\omega)/\epsilon_{inc}(\omega)|^2$.
The calculations have been performed for the following parameters: $E_c = 1.4513$ eV, $E_x^0 - E_c = 3.32$ meV, $2\Omega_R$=3.26 meV, and a Gaussian shape of the exciton line with $\Gamma = 0.7$ meV as well as the center of the exciton line modulated in time by the strain pulse. In order to obtain a better fit of the reflectance spectra near the upper polariton branch an asymmetric shape of the inhomogeneous exciton line was used. The best agreement with the experimental results has been obtained for $a = -20$ eV.
Figure 8.4(a-c) shows the spectra calculated when the exciton resonance is modulated by strain pulses generated at $P = 8$ mJ/cm^2 (Figs. 8.4(a) and 8.4(b)) and $P = 1$ mJ/cm^2 (Fig. 8.4(c)). The inhomogeneously broadened exciton line is smeared and the spectral peculiarities near the UP branch are not observed (Fig. 8.4(a)). However, inhomogeneous broadening of the UP has nearly no effect on the lower branch (Fig.8.4(b)) and several sidebands accompanying the main resonance are clearly visible. Most of the calculated sidebands in the LP modulated spectrum are observed also in the experiments (compare Figs. 8.2(b) and 8.4(b) and see insets in Fig. 8.4(b)). For a quantitative comparison we chose the time interval 10 ps to 25 ps where $\eta(t)$ changes linearly with t. To characterize the nonequidistant sideband fringes we consider the spectral separation δ (see the bar in Fig. 8.2(d)) between the zero-order minimum and first maximum in the sideband of the reflectance spectrum at fixed delay t_0. Figure 8.4(d) shows the experimental (closed symbols) and calculated (open symbols) values of δ as a function of P. These data are taken at t_0 =20 ps where δ can be considered almost independent of t_0 in the time interval $(t_0 - \tau_c, t_0 + \tau_c)$. Good agreement between the experimental and calculated values is seen, which supports that the suggested model of diabatic optical frequency modulation is appropriate for describing the underlying physics. The nonmonotonic dependence of δ on P results from the nonlinear strain pulse propagation in the GaAs substrate [27][29]. At small $P < 3$mJ/cm^2 the strain $\eta(t)$ shows only changes in amplitude while the shape in the time interval between negative and positive $\eta(t)$ remains the same. This yields $d\omega(t)/dt \sim P$ and correspondingly an increase of δ with P. For higher $P > 4$mJ/cm^2 the dynamical strain pulse consists of an acoustic soliton train at the front and a dispersive oscillating tail at the end while in the middle $d\omega(t)/dt$ first saturates and then decreases with increasing P [29].
Besides the observation of sidebands, the experiments bare another interesting feature connected to the strong coupling of the exciton and cavity mode resonances. To illustrate this, Fig. 8.5 shows the contour plot already shown in Fig. 8.2(b) on an extended timescale. Low amplitude oscillations occur between $t_0 = 150$ ps and $t_0 = 500$ ps due to reflected components of the acoustic pulse on the microcavity interfaces. The sideband effect is only weakly pronounced, making it possible to follow in reasonable

approximation the stationary LP resonance.

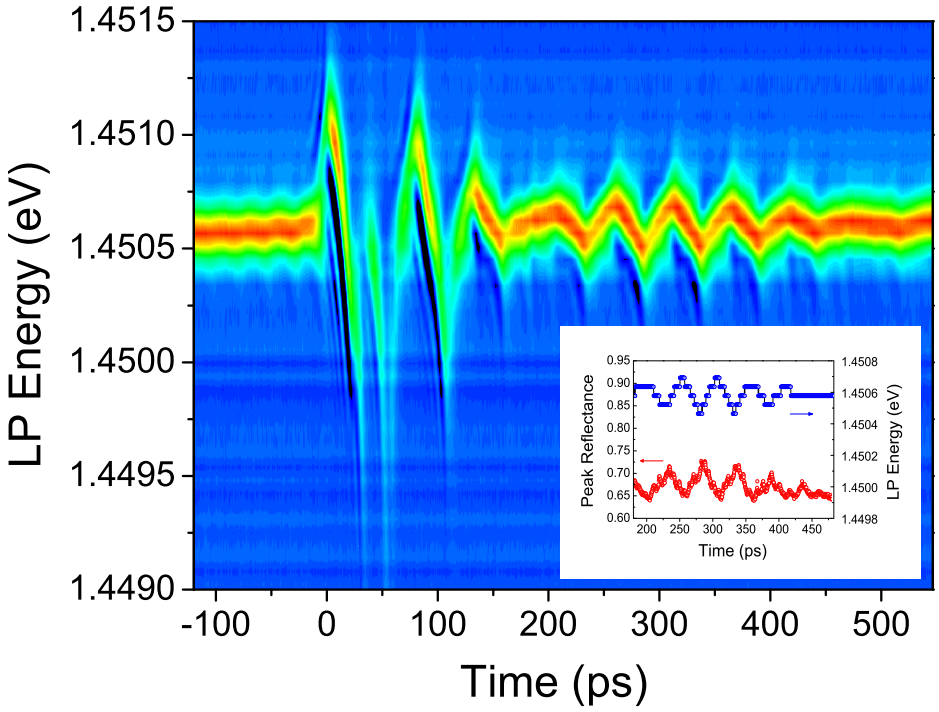

Figure 8.5: Spectral/temporal contour plot obtained from $P = 8\text{mJ/cm}^2$ like Fig. 8.2(b) but an extended timescale is shown. (inset) LP energy (blue symbols) and LP reflectance at the peak position of the resonance (red symbols).

The inset shows the LP energy position (blue symbols) and the reflected amount of intensity at the respective peak position of the LP resonance line (red symbols, compare also 8.1(b)). Apparently, antiphase oscillations are present, reflecting the well known behaviour within the polariton formalism, which is explained in detail in Chapter 3.1.3. At times when the LP resonance shifts to higher energies (as a result of the exciton shift), the detuning $E_x - E_c > 0$ increases and the LP gains photonic character. This manifests in a more pronounced LP resonance and accordingly to a lower reflectance coefficient at the peak position of the resonance.
The injected strain pulse though is able to modulate the light matter interaction in a well defined manner. To gain more insight into this aspect, Chapter 9 will provide more information on the ultrafast manipulation of light matter interaction.

8.5 Conclusions and Outlook

In conclusion the generation of sidebands in the microcavity polariton spectrum as a result of ultrafast, high amplitude optical frequency modulation has been demonstrated experimentally. The sideband spectra show quasiperiodic fringes with a period depending on the modulation rate $d\omega(t)/dt$. The frequency modulation can be analyzed by a simple diabatic model, in which the central optical frequency shifts by an amount larger than the spectral width during a time shorter than the coherence time of the resonance. The origin of the detected sidebands is distinctly different from that of the well-known vibronic sidebands or THz radiation induced sidebands [94] in optical spectra near the resonance lines of electronic transitions. The sidebands observed here require not only fast modulation times $\tau_a < \tau_c$ but also high modulation amplitudes $\Delta\Omega$, which exceed the stationary spectral width. The sidebands can be detected only in the coherent regime and may be considered as an optical analog of radio frequency signals, for which high amplitude frequency modulation is widely used.

9 Manipulation of Light Matter Interaction

Previously it has been shown that placing a quantum well (QW) inside a microcavity, in the strong light matter interaction regime a sharp photon like (lower) polariton resonance (LP) in a well detuned system might be observed (Chapter 8). The energy modulation of the underlying exciton resonance results in a shift of the LP for values exceeding the resonance width within times τ_a being shorter than the LP coherence time. This was shown to establish a novel diabatic regime in semiconductor optics, resulting in pronounced sidebands accompanying the resonance energy shift. In the preceeding chapter it has been already suggested that the methods of ultrafast acoustics might offer an access to modulation processes concerning the light matter interaction of excitons and cavity photons. In this chapter experiments will be presented, using a quantum well cavity at negligible detuning in order to demonstrate the ultimate possibilities connected with the modulation of light matter interaction induced by a picosecond strain wave.

9.1 Introduction

Manipulating Light-Matter Interaction (LMI) is a basic necessity for various fundamental applications in atom physics as well as in solid state physics. Especially in semiconductor physics, the strong interaction of electronic transitions with light have gained a lot of interest since manipulation and characterisation on picosecond timescales and below became feasible [83][95].
In particular tailoring the electromagnetic environment of an (optical) emitter using quantum confined photons in down to zero dimensions has been shown to be an efficient way to manipulate the radiative properties of the respective emitter [96]. In this so called weak-LMI regime significant losses of the system occur much faster than the interaction of the photon and the emitter appears to be [95]. Increasing the quality of the photonic resonator (i.e. increasing the time within the photon and the emitter can interact) leads to a strong-LMI regime as far as the oscillator strength of the emitter is sufficiently large, and the involved emitter is in resonance with the confined cavity mode (see Chapter 3.1.3). The system then shows new eigenstates called the upper and the lower polariton branches (UP, LP).
Cavity structures furthermore act as high repetitive optical emitters [96], optical retarders [97], lasers [98] and parametric amplifiers [99]. Moreover these cavities have

been considered as candidates for optical information storing, processing and transmission [100] as well as for Bose-Einstein condensates [101]. Experimental studies on the population dynamics in Atoms have shown that both, the amplitude and the frequency of the energy modulation of one of the underlying states can have significant influence on the transition probabilities in the respective system [102]. However, the transient picosecond switching from strong- to weak-LMI, precisely from the transition of a state which is characterized by a coherent conversion of a photon into a solid state excitation (and back), to an uncoupled state in semiconductors has remained challenging [103]. In this chapter the picosecond switch from strong- to weak-LMI utilising a semiconductor quantum well interband transition coupled to the confined mode of a planar optical microcavity will be demonstrated. The switch was induced by a terahertz acoustic pulse, which has been shown to be a powerful tool for manipulating optical transitions in semiconductors on picosecond and sub-picosecond timescales (see also Chapters 7 and 8) [85][50]. In the experiments described in the following, the energy of the underlying exciton resonance of an optical system, initially governed by strong-LMI is modulated in time, such that the characteristic Rabi-Frequency $2\Omega_R$ is exceeded. The amplitude of the energy modulation thereby is so high, that effectively the regime of strong-LMI is left.

9.2 Experimental Conditions and Sample

Picosecond strain waves have been applied to a 100 μm thick GaAs substrate using a 100 nm thin aluminium transducer excited by a high intense 150 fs laser pulse of wavelength 800 nm. The maximum reached excitation energy density on the transducer was $P = 14$ mJ/cm^2. A sketch of the experimental configuration is shown in Fig. 9.1. Propagating along the GaAs substrate, anharmonicity and dispersion give rise to acoustic soliton formation, leading to acoustic angular frequencies up to 10 THz [15]. After a propagation time $\sim$ 20 ns the strain wave reaches an 8 nm wide $In_{0.04}Ga_{0.96}As$ quantum well (QW) embedded in a high quality (Q $\sim 10^4$) optical cavity (Q, quality factor of the cavity mode). The cavity has been built up from 24 periods and 20 periods of AlAs/GaAs $\lambda/4$ layers forming the bottom (toward substrate) and top mirrors (toward vacuum) respectively. λ represents the wavelength of the confined cavity mode. The energy detuning between the pure QW exciton (electron-hole) resonance energy E_x and the pure cavity mode energy E_c is negligible at a temperature of 10 K and $k \approx 0$ (see Fig. 9.1(a)), leading to two almost equivalent polariton resonances in the strong-LMI regime. The polariton resonances split by $2\Omega_R = 5.7$ THz in terms of angular frequencies and the ralation $E_x - E_c \approx 0$ holds, if no strain wave is present. A corresponding reflectance spectrum, obtained with a frequency shifted laser pulse (via an optical parametric amplifier: *coherent* OPA) from the same source like the strain wave excitation pulse is shown in Fig. 9.1(b).

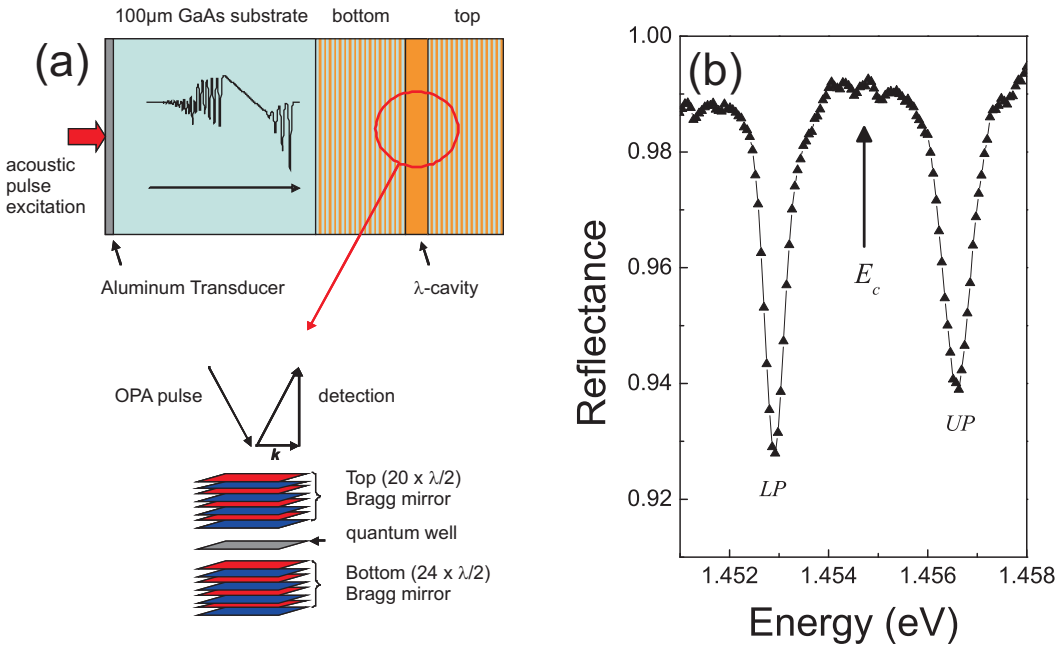

Figure 9.1: Experimental preconditions: (a) Sketch of the quantum well microcavity formed by two Distributed Bragg Reflectors and a central cavity layer with a centered quantum well at the antinode position of the confined light field. The strain pulses are injected via the aluminum film (left sided red arrow). (b) Reflectance spectrum at $T = 10$ K without applied strain pulse: LP and UP denote the lower and upper polariton resonances, respectively. (blach arrow) E_c points the expected energy of the caity mode.

The detection was realized using a 0.5 m grating spectrometer yielding a spectral resolution of 0.16 meV. Varying now the time delay t between both laser pulses (i.e. strain wave excitation and reflectance), it is possible to measure the time dependent influence from the strain wave on the reflectance. The observed changes are essentially due to deformation potential interaction, which determines the exciton energy (see Chapters 6, 7, and 8)[29][50][51].

$$E_x(t) = E_x + a\eta(t) \approx E_x + \Delta(t), \tag{9.1}$$

when the QW undergoes a time dependent uniaxial deformation $\eta(t)$ (see for example [104]) due to the presence of the strain wave, turning Δ into the time dependent function $\Delta(t)$ (a < 0, electron hole net deformation potential, see for details Chapter 3.2). The cavity mode energy will be taken to be constant within the experimental error in the following discussion (for justification see Chapters 8 and 6).

9.3 Results and Discussion

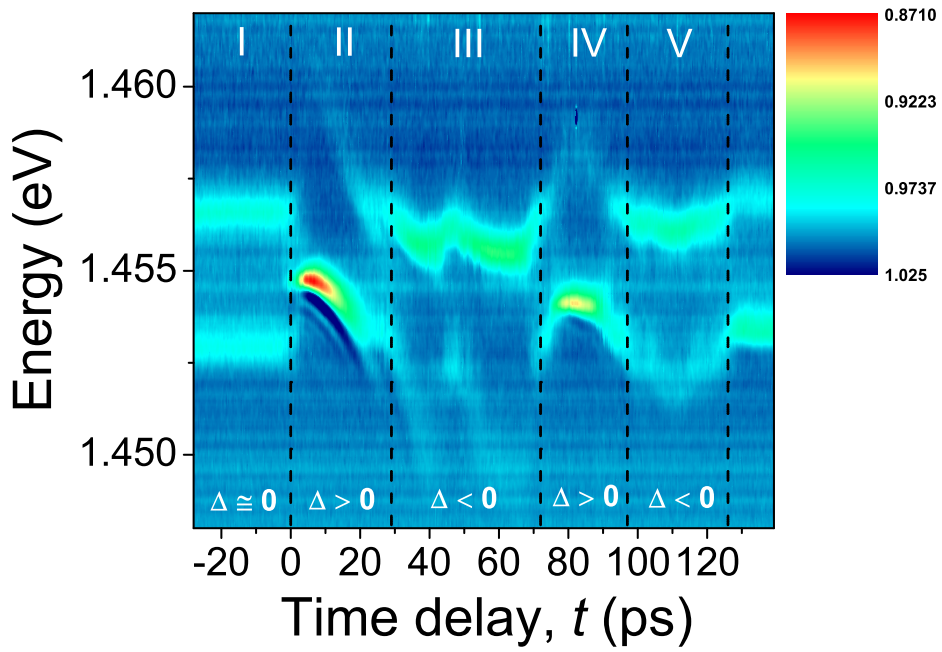

Figure 9.2: Spectral/temporal contour plot at an applied strain wave excitation density of $P = 12.5\text{mJ/cm}^2$ ($T = 20$ K). The strain wave impacts the central cavity layer at $t \approx 0$ ps. The areas I,II,..,V indicate the different coupling regimes with $\Delta \approx 0$ (area I), $\Delta > 0$ (areas II and IV) and $\Delta < 0$ (areas III and V).

Figure 9.2 shows a temporal/spectral contour plot of the observed reflectance spectra at a temperature $T = 20$ K at $P = 12.5$ mJ/cm^2. The time axis gives the time delay t, recorded with a sampling step of $\delta t = 300$ fs. The time $t = 0$ highlights the time delay when the strain wave enters the QW in the central cavity layer. Figure 9.2 is subdivided in areas labeled I,II,...,V, temporally separated by dashed vertical lines, which indicate the time windows of different light matter interaction conditions, i.e. $\Delta \approx 0$, $\Delta < 0$ or $\Delta > 0$. In area I the strain wave has not yet influence on the spectra and the UP and LP branches remain like shown in Fig. 9.1(b). At the beginning of area II ($t \approx 0$ ps) the UP and LP branches vanish from the spectrum, whereas a pronounced single resonance appears in between the LP and UP energy positions as seen in area I. Later on well separated sidebands occur (see Chapter 8) [50], and at the end of area II ($t \approx 30$ ps) again two equal polariton branches are seen at the original polariton energies. In the subsequent area III, the LP branch evolves to be very weak beside the UP branch, both shifted to lower energies until again two equal branches are seen. Contrary in area IV the LP branch is more pronounced than the UP branch

and both are shifted to higher energies. In area V a similar situation like in area III is apparent.

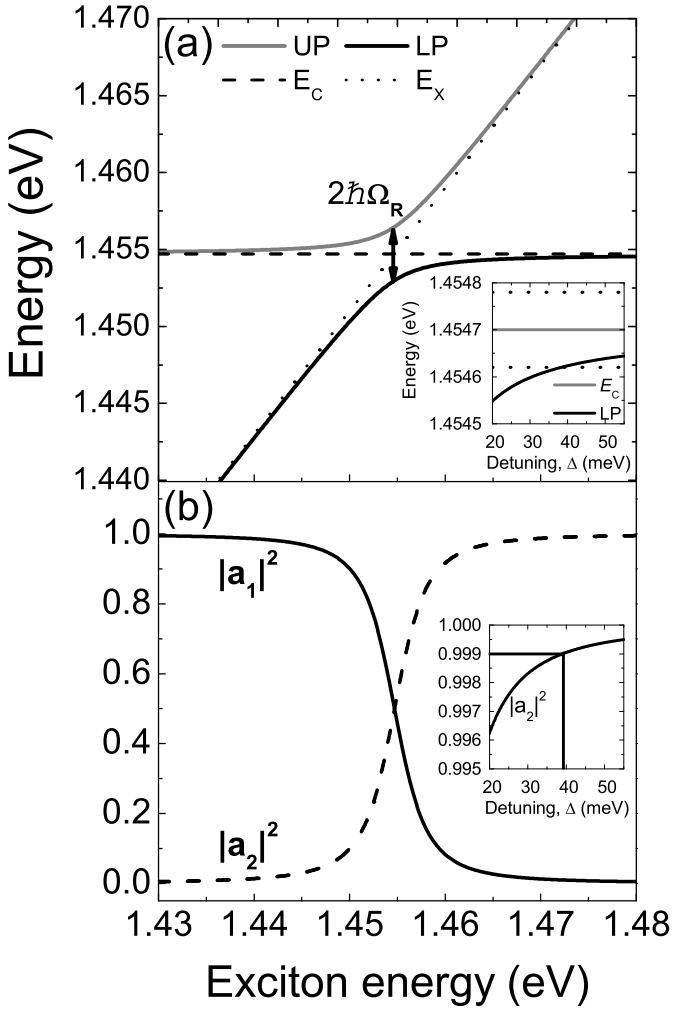

Figure 9.3: Calculated polariton properties according to Equations 3.12 and 3.16. (a) UP and LP polariton energies in dependence on the underlying exciton energy E_x (dotted line). The cavity photon energy E_c (dashed line) is held constant. The polariton energies anticross at resonance i.e. $E_x = E_c = 1.4547$ eV with a splitting according to Equation 3.14. (b) Same dependence as in (a) but for the Hopfield Coefficients $|a_1|^2$ and $|a_2|^2$ following Equation 3.16.(insets) Zoom into the dependencies in (a) and (b). (a) LP energy (solid black line) and cavity mode energy E_c (solid grey line) as a function of the detuning Δ. Dotted lines indicate the experimental uncertainty. (b) Same for the hopfield coefficient a_2^2. The solid lines indicate the minimum values of Δ and a_2^2 at which the LP gets purely photonic within the experimental uncertainty.

The observed evolution of the polariton branches can be explained straight forward, considering the polariton wave functions (see Chapter 3.1.3, Equation 3.15)

$$|\Psi\rangle = |\mathrm{UP}\rangle + |\mathrm{LP}\rangle = (a_1(\Delta_d)|C\rangle + a_2(\Delta_d)|X\rangle) + (a_1(\Delta_d)|X\rangle - a_2(\Delta_d)|C\rangle), \quad (9.2)$$

where $|X\rangle$ and $|C\rangle$ denote the exciton and the cavity state vectors respectively. The Hopfield coefficients $a_1(\Delta)$ and $a_2(\Delta)$ give the excitonic and photonic density of the respective polariton branch in dependence of the detuning $\Delta(t)$. In particular it is $\sqrt{a_1^2(\Delta) + a_2^2(\Delta)} = 1$. Further the avoided crossing behaviour of the polaritons (Equation 3.12), which at a given detection angle, determines the energies $E_{\mathrm{UP}}(\Delta)$ and $E_{\mathrm{LP}}(\Delta)$ of the polariton branches as well as their resonance width in dependence of

the exciton energy $E_x(\Delta)$ is to be considered. The polariton energies $E_{\mathrm{UP,LP}}(E_x)$ as well as the Hopfield coefficients $a^2_{1,2}(E_x)$ are plotted in Figure 9.3(a) and Figure 9.3(b), respectively, where $\Delta = 0$ at resonance when $E_x = E_c = 1.4547$ eV (see also Chapter 3.1.3). Corresponding to Fig. 9.2 (area I), at resonance, the UP and LP branches are both, excitonic and photonic in the same manner as $a_1^2 = a_2^2 \approx 0.5$ with the energies $E_{\mathrm{UP,LP}}(\Delta \approx 0) \approx E_c \pm \hbar\Omega_R$ (see equation 9.1 and Fig. 9.3(a,b)).
Since the leading edge of the strain wave compresses the crystal rapidly (i.e. easily $|d\eta(t)/dt| > 10^{-3}$/ps and $\eta(t) < 0$) [50], following Equation 9.1 and Fig. 9.3(a,b) the LP (UP) branch shifts to higher energy and gains photonic (excitonic) character (beginning of area II ($t \approx 0$ ps in Fig. 9.2). Later, when the compressive part of the strain wave has passed the QW and again $\eta(t) = 0$ and so $\Delta(t) = 0$ (end of area II ($t \approx 30$ ps)) equal polariton branches are recovered. In general when the strain changes the sign of $\Delta(t)$ (dashed lines in Fig. 9.2), i.e. $\eta(t)$ passes zero, the two polariton branches exchange their properties from photonic to excitonic and vice versa (Fig. 9.3(b)) while they are shifted to higher ($\Delta(t) > 0$) or lower ($\Delta(t) < 0$) energies following the avoided crossing curves (Fig. 9.3(a)). From Figure 9.2 it is obvious that the deformation amplitude of the strain wave decays in time while it is changing its sign from negative ($\eta(t) < 0$) to positive ($\eta(t) > 0$) several times within the observed time window. Apparently the strongest modulation of the spectra is observed at time $t \approx 0$, where the spectra change from double to single resonance.

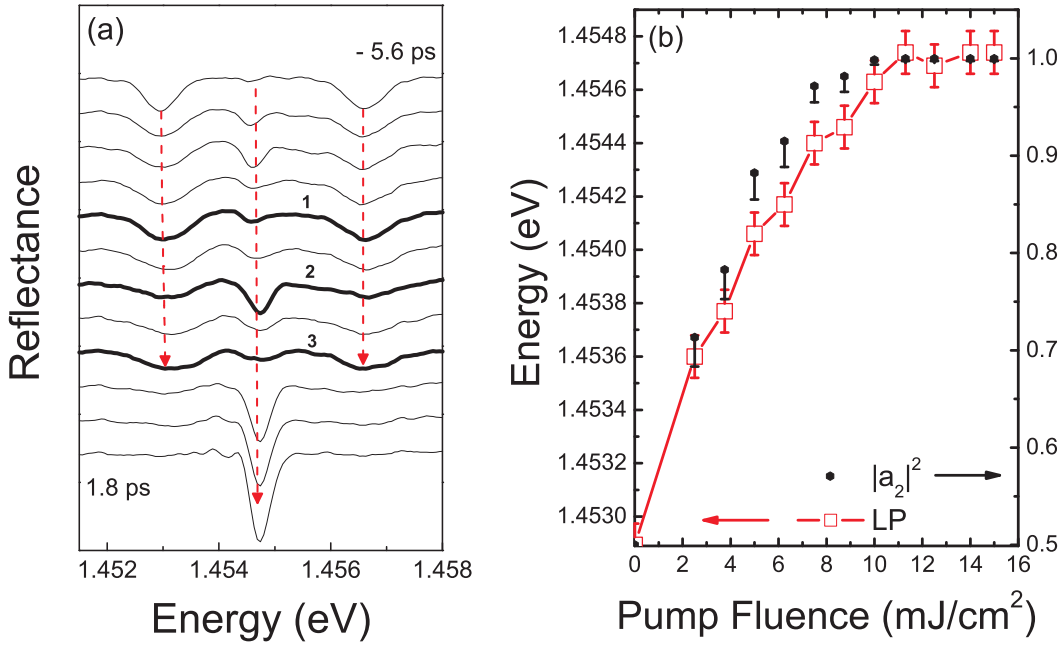

Figure 9.4: Experimental data from the transition region from weak-LMI to strong-LMI around $t = 0$ ($T = 10$ K). (a) Single spectra separated by ≈ 0.7 ps from $t = -5.6$ ps (upper spectrum) till $t = 1.8$ ps (lower spectrum). The spectra are shifted vertically for clarity. Red arrows indicate the time evolution of the resonances energies. (bold solid lines) Highlighted spectra (1,2,3) refer to the discussion in the text. (b) "LP" energy (red squares) as obtained at $t = 1.8$ ps and deduced hopfield coefficient a_2^2 (black dots) as a function of the strain wave excitation density P on the aluminum transducer.

In order to reduce the damping of the strain wave due to interaction with thermal phonons [13] and keeping to a high extend the experimental conditions given above (i.e. $\Delta \approx 0$), the temperature has been reduced to $T = 10$ K. Several spectra separated by ≈ 0.7 ps are shown in Fig. 9.4(a) obtained at $P = 14$ mJ/cm^2. Clearly the two polariton branches vanish while a single resonance appears close to the energy position in the middle between the polariton branches. The energies of the three involved resonances thereby stay constant during the transition process within experimental accuracy indicated by red dashed arrows.
The maximum energy position (corresponding to $t = 1.8$ ps in Fig. 9.4(a)) of the LP, which according to Figures 9.3(a,b) provides information about the photonic character of the resonance has been determined in dependence of P. The result is shown in Fig. 9.4(b) (open squares), where the error bars represent the spectral resolution of the detection apparatus. The LP maximum energy increases with increasing P, i.e. with increasing $|\eta^{max}|$, until it saturates at the energy $E_c \approx 1.4547$ eV within the experimental resolution. This energy corresponds to a maximum reached $\Delta(t)$ of at least 39 meV as shown in the inset of Fig. 9.3(a). Here the dashed lines denote the experimental error among the cavity mode energy. The corresponding Hopfield coefficients $a_2^2(P)$ are plotted in Fig. 9.4(b) as black dots and the error to lower values has been estimated on the basis of the experimental resolution and the polariton energy and Hopfield coefficient curves according to Equations 3.12 and 3.16. The maximum reached value of $a_2^2 = 0.9997 - 0.003$ (compare also inset of Fig. 9.3(b)) indicates a purely photonic mode within the experimental resolution and so a complete breakdown of the polariton in the experiment, indicating a transition from the strong-LMI to the weak-LMI regime.
An additional observed feature within the transition from strong to weak LMI within the time window between $t = -5.6$ ps and $t = 1.8$ ps (Fig. 9.4(a)) can be seen directly considering the highlighted (bold lines) spectra in Fig. 9.4(a). The third resonance at energy E_c is seen to gain intensity not monotonuosly, but shows an oscillating amplitude in dependence of the delay time t with a period of (1±0.3) ps (compare bold lines 1,2, and 3 in Fig. 9.4(a)). This period is in good agreement with the normal mode splitting $\tau_{2R} = 2\pi/2\Omega_R = 1.1$ ps. The amplitude of the oscillations thereby increases with t. The oscillations affect the middle resonance (at E_c) as well as the resonances at E_{LP} and E_{UP}, where the intensities at the polariton energies oscillate in phase with respect to each other. Contrary, the intensity of the resonance at E_c oscillates in antiphase with respect to the other two resonances.
This behaviour is not understood completely but might be a step forward to subcycle coherent control of light matter interaction in an optical cavity. The highest modulation angular frequecies involved (>10 THz) clearly exceed the Rabi frequency of 2.85 THz in this case and constitute a high amplitude leading strain edge, offering the possibility to modulate the coupling faster than the recurrence times, i.e. the Rabi-cycle, concerning the polaritons time evolution.
To verify that the reached energy E_c of the lower polariton resonance indeed is limited by the crossing behaviour of the involved polariton energies and so, is equivalent to the photonic mode energy, Fig. 9.5 shows the experimental polariton energies (LP,UP)

without applied strain wave (blue circles) as a function of temperature T.

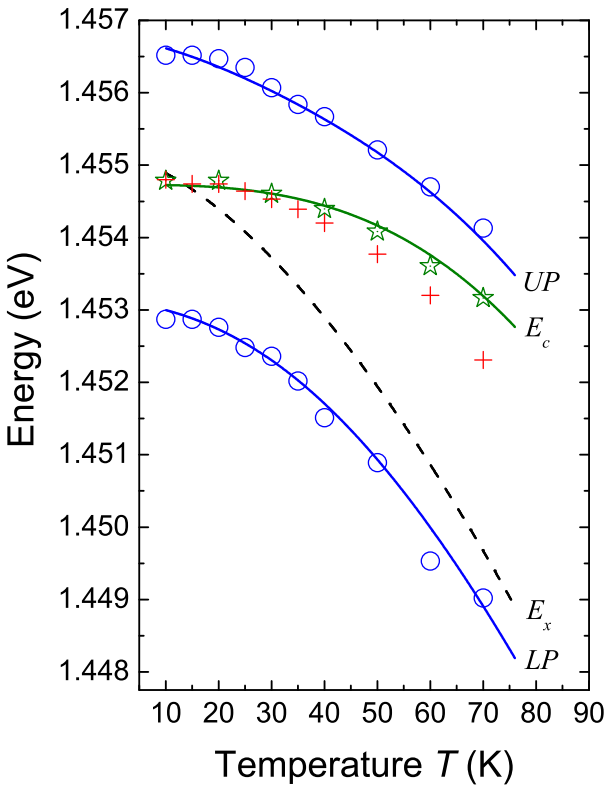

Figure 9.5: Energy structure as a function of temperature T. (blue circles) UP and LP energies as obtained from reflectance measurements. (green stars) shifted cavity mode energies obtained from high density photoluminescense spectra of a reference sample (see Chapter 10). The slopes have been fitted (solid lines) to yield the underlying exiton energy (dashed black line). Parameter: Normal mode splitting $2\Omega_R = 3.62$ meV, exciton linewidth $\delta E_x = 0.4$ meV, cavity mode linewidth $\delta E_c = 0.17$ meV, $E_c(T = 15\text{ K}) = E_x(T = 15\text{ K}) = 1.4547$ eV. Red crosses show the experimentally measured maximum LP energies at delay time $t \approx 0$.

The green stars indicate the measured temperature dependence of the cavity mode obtained from high excitation density luminescense spectra [105] of a similar sample structure with different detuning due to the growth procedure (see Chapter 10). An example for the obtained cavity mode energy is shown in Fig. 9.6. Note that the radiative decay in the laser regime, using pulsed high density excitation, is much shorter than the luminescense decay, which was not detected in the corresponding time resolved spectra at long times. The long-term low density luminescense component due to depletion of the quantum well therefore has been assumed to be negligible in the time integrated spectra at very high excitation density. The measured datapoints have been shifted to the calculated value corresponding to $\Delta = 0$ ($T = 15$ K), and the slope has been fitted (green solid line) together with the measured polariton energies (blue solid lines) to obtain the exciton energy (dashed black line) using Equation 3.12. The red crosses correspond to the maximum values of the LP resonance ($P = 12.5$ mJ/cm^2) at $t \approx 0$ (shown in Fig. 9.2). It is seen that the shifted LP energy follows the temperature dependence of the cavity mode energy up to $T = 30$ K, where the induced higher LP energy shift ΔE_{LP} increases with temperature (difference energy between the lower blue circles and the red crosses). This behaviour is a clear indication for ΔE_{LP} being limited by the cavity mode energy E_c and not by the applied maximum

strain amplitude at low T.

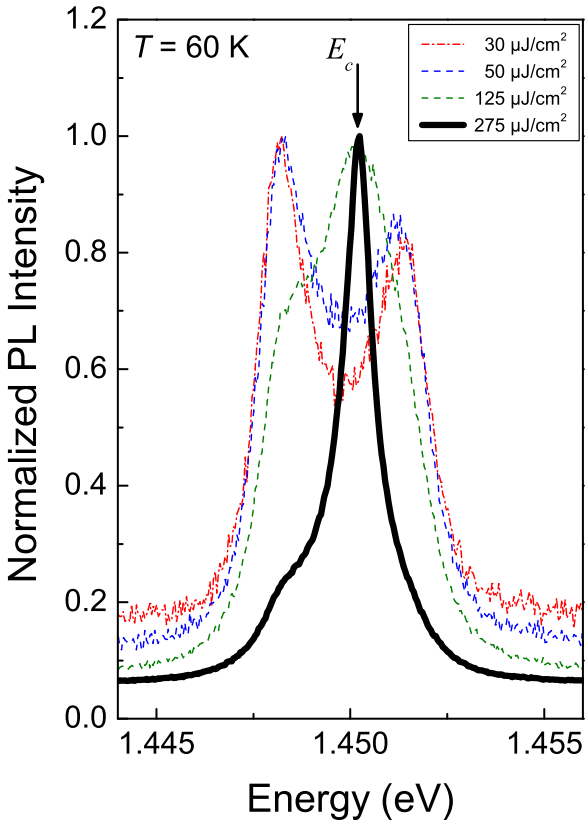

Figure 9.6: Photoluminescense spectra of a reference sample discussed in detail in Chapter 10. The full polariton temperature dependence is shown in the inset of Fig. 10.1(a). The cavity mode energy E_c has been obtained from the bold (black) spectrum which corresponds to the excitation density of $I = 275\mu\text{J/cm}^2$.

9.4 Summary and Outlook

The subterahertz transition from strong light matter interaction to weak light matter interaction and back in an optical cavity initially strongly interacting with a quantum well interband transition (exciton) was demonstrated. The applied ultrafast acoustics technique opens a new way to manipulate the coupling strength with THz frequencies. This is in particular interesting for the ultrafast control of polariton population dynamics, which is highly desired in quantum information processing schemes. The long term oscillatory behaviour of the strain wave might be tailored by phononic band gap materials, the variation of the metal type, the metal thickness and the surface coating of the used transducer. Also the control of the injection (propagation) process of the strain wave into (in) the substrate/sample (substrate) might be tailored using different materials (material thicknesses). Additionally, indications of sub-rabi-cycle modulation have been turned out, not seen in similar structures up to now. The ultrafast acoustics technique further proposes room temperature operation [70] with a

high potential for effective modulation processes, which indeed offers a prospective possibility for future applications.

10 Ultrafast Control of Polariton Emission Dynamics

Focusing on the reflectance spectra of a strongly coupled quantum well microcavity, where no carriers, i.e. elctrons and holes, have been excited in the preceding Chapters 8 and 9, in the following - closing - experimental Chapter, carriers are of explicit importance enabling the system to actively emit light. The electrons and holes thereby might be excited above the band gap and diffuse to the quantum well where they scatter to the lowest energy level and recombine radiatively. The emitted (confined) photons though couple strongly to the quantum well and will be released from the cavity at the polariton energies E_{UP} (upper polariton) and E_{LP} (lower polariton), where the emission distribution depends on the respective resonance profile as well as on the Boltzmann distribution in the stationary (linear excitation) case. Higher excitation densities might cause increasing scattering mechanisms, which lower the Rabi splitting, and at a certain threshold the breakdown of strong coupling in the system (see Fig. 9.6)[106][107][105]. In the focus of this chapter will be the question how and to what extend it is possible to manipulate the emission dynamics of a strongly coupled quantum well microcavity in the non-coherent regime on ultrafast timescales using a picosecond strain pulse [104].

10.1 Introduction

High-frequency acoustics has been recently shown to be a prospective tool for manipulating optical emission characteristics in microcavities (MCs) [85][108]. One of the currently challenging tasks of acousto-optics is to realize ultrafast intensity and frequency modulation of the spontaneous and stimulated light emission from nanophotonic emitters. Traditional ultrasonic experiments have been successfully performed on semiconductor MCs but there the modulation frequency is limited to the gigahertz frequency range [108][60]. The extension of the modulation frequencies to the terahertz range would provide significant progress in the ultrafast control of light emission from such cavities.
In the following, the potential of ultrafast acoustics, using picosecond strain pulses for modulating the photon energy of the spontaneous photoluminescence (PL) from a MC with a quantum well (QW) as the optically active medium will be explored. The strain pulse induces a dynamical energy shift of the quantum well exciton resonance, which results in an ultrafast modulation of the photoluminescence spectrum from the lower

polariton branch.
The studied MC structure was grown by metal-organic chemical-vapor deposition (MOCVD) on a (001)-oriented GaAs substrate.

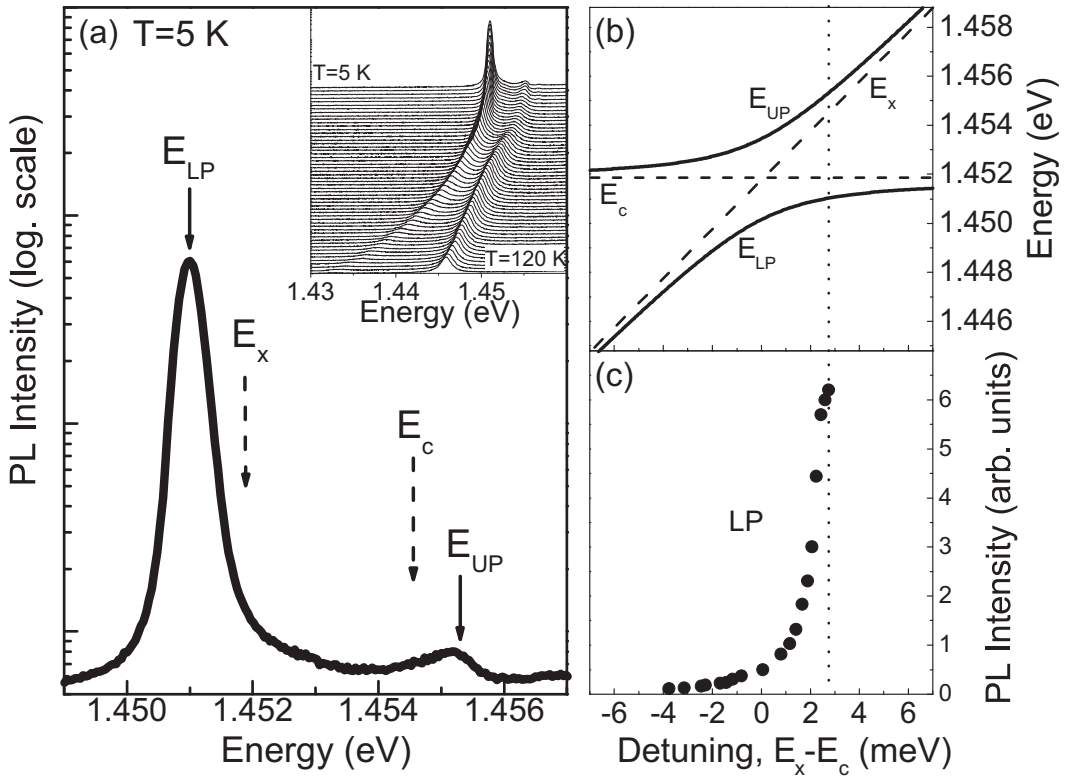

Figure 10.1: (a) Photoluminescence spectra of the studied MC structure at T=5 K for cw-low power excitation (λ_{las} = 352 nm; 100 W/cm^2). The dashed and solid vertical arrows indicate the energies of the uncoupled states (C photonic mode; X QW exciton) and polariton resonances (LP and UP), respectively. The inset shows PL spectra for different temperatures T=5-120 K. At T = 50 K the minimum-energy separation between the PL lines which is equal to 3.3 meV is reached corresponding to the Rabi splitting. (b) Calculated energies of lower and upper polariton branches as a function of detuning between the photon mode and the QW exciton for a Rabi splitting of 3.3 meV at T = 1.8 K (compare Fig. 3.7). The dashed lines are the resonance energies of the photon mode and the QW exciton. (c) Dependence of the lower polariton emission intensity on detuning determined from the temperature dependence of the PL spectra. The vertical dotted line in panels (b) and (c) shows the detuning at T = 1.8 K in the absence of a strain pulse.

It contains an 8-nm-wide InGaAs QW in the middle of a GaAs barrier layer with a width d=240 nm, corresponding to the wavelength λ of the confined photon resonance. This λ-cavity layer is surrounded by Bragg mirrors made from 24 and 20 pairs of GaAs/AlAs $\lambda/4$ wave stacks at the bottom (toward substrate) and the top (toward vacuum) respectively. The quality factor Q (for definition see Chapter 6) of the MC is $\sim 10^4$ and the exciton linewidth ≈ 0.6 meV, leading to the strong coupling regime among the resonances [46]
The PL spectrum measured at normal incidence to the cavity at low temperature (T = 5 K) for cw excitation is shown in Fig. 10.1 by the solid line. The spectrum

consists of two emission lines with maxima at E_{LP} and E_{UP}, which correspond to the lower and upper polariton states, respectively. The dashed vertical arrows labeled E_c and E_x indicate the energies of the uncoupled photon and exciton resonances of the MC and the QW (see also Fig. 9.5 for illustration). The value of 3.3 meV for the Rabi splitting was obtained from the dependence of the spectral position of the PL lines on temperature T (see inset) [109]. The calculated dependence of the polariton energies as a function of detuning E_x-E_c is shown in Fig. 10.1(b). For further consideration it is convenient to present the curves in Fig. 10.1(b) such that E_c shown by the dashed horizontal line is fixed while E_x (oblique dashed line in Fig. 10.1(b) could be tuned. The vertical dotted line in Fig. 10.1 corresponds to a detuning $E_x - E_c$=2.7 meV at T=1.8 K. Figure 10.1(c) shows the experimental dependence of the intensity of the lower polariton branch emission as a function of detuning, measured by varying the temperature. This dependence qualitatively is similar to one that was measured at fixed temperature for different detunings in a wedge-shaped cavity [110].

10.2 Strain Modulated Photoluminescense

The scheme of the ultrafast acoustics studies is shown in Fig. 10.2(a). A beam from a 150 fs ti:sapph laser pumping a regenerative amplifier (wavelength 800nm and repetition rate of 250 kHz) was used for generation of strain wave packets in a 100-nm-thin Al transducer deposited on the polished substrate opposite to the MC structure [19].

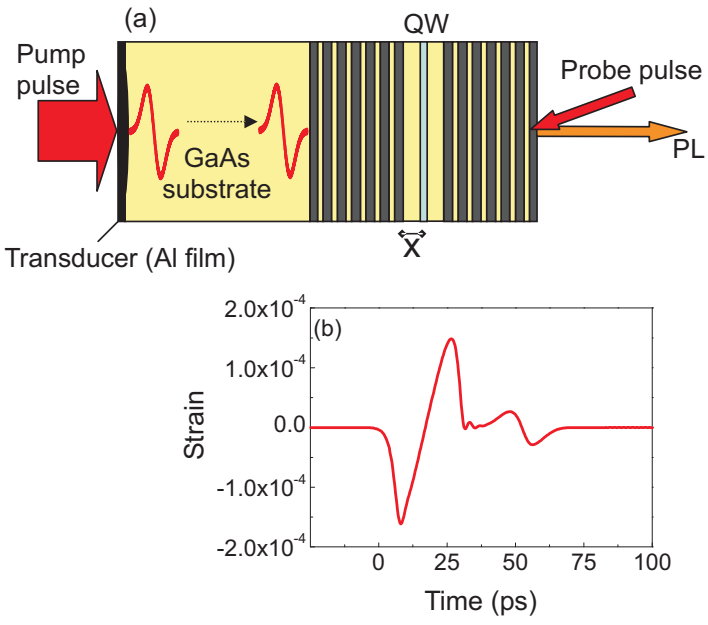

Figure 10.2: (a) Scheme of experiment with picosecond strain pulses. (b) Calculated temporal shape of a strain pulse at the interface between substrate and Bragg mirror in the medium excitation density regime (Chapter 2.2).

As a result of optical excitation with an energy density of 3 mJ/cm^2 on the metal film, a bipolar strain pulse with a strain amplitude of $\sim 10^{-4}$ is injected into the GaAs substrate. The strain wave packet propagates through the 100 μm GaAs substrate with the velocity of longitudinal sound s = 4800 m/s, so that after about 20 ns it reaches

the MC. Figure 10.2(b) shows the calculated temporal evolution of the pulse reaching the MC. Details of the calculations, which include the nonlinear elastic properties of the GaAs crystal, can be found in Chapter 2.2 [72].
A second beam split from the same laser excites nonresonantly the polariton PL through the top surface of the MC. The excitation wavelength (800 nm) thereby corresponds to the first stop band minimum, allowing for efficiently coupling light into the cavity structure (compare Fig. 3.3). The delay between the two pulses was set to about 20 ns so that the strain wave passes the GaAs substrate and reaches the MC when the PL is emitted with a decay constant τ_l. The effect of the strain pulse on the lower polariton emission was monitored by measuring the time-resolved PL spectrum with a single spectrometer followed by a streak camera. The temporal resolution was about 30 ps corresponding to a spectral resolution of $\sim$ 0.16 meV.

10.3 Experimental Results

Figure 10.3 shows the temporal and spectral streak camera images of the lower polariton PL intensity $I(E,t)$ measured at T=1.8 K in the absence (left) and in the presence (right) of the strain pulse. In the absence of the strain pulse (panel (a)) the PL line shifts to lower energies while decaying with a time constant of $\tau_l \approx 350$ ps. This behavior is governed by the dependence of the light-matter coupling parameter on the polariton density as discussed earlier for similar MC samples [106][107].

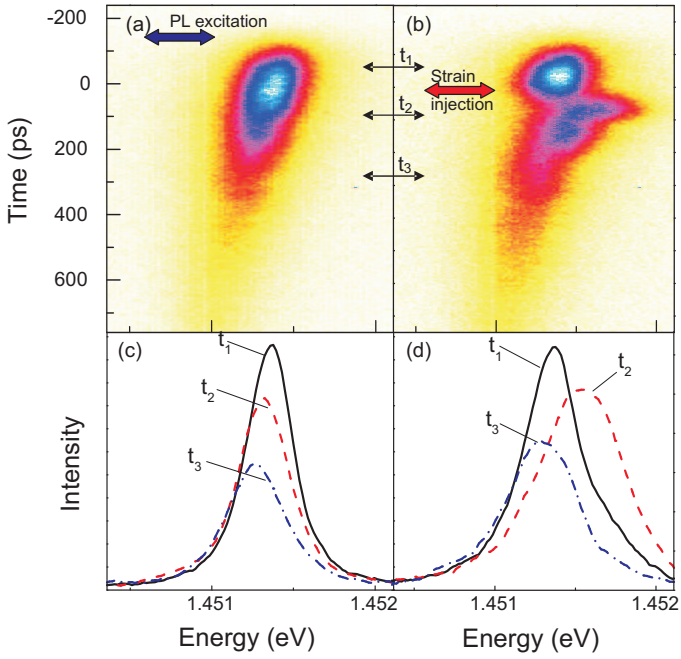

Figure 10.3: Streak-camera images of the temporal (vertical direction) and spectral (horizontal direction) PL evolution in the (a) absence and (b) presence of a strain pulse at T=1.8 K. The big horizontal arrows show times, which correspond to the pulsed excitation of the PL (panel (a)) and injection of a strain pulse into the MC (panel (b)). Panels (c) and (d) demonstrate spectral profiles at time delays shown in (a) and (b) by numbered arrows in (c) absence and (d) presence of a strain pulse.

The image in Fig. 10.3(b) shows the PL decay when a strain wave packet has been injected into the MC. The delay Δt between the exciting PL laser pulse (shown by the big horizontal arrow in panel (a)) and the time moment when the strain pulse

reaches the MC (shown by the big horizontal arrow in panel (b)) is 150 ps. Compared to the case without strain, a pronounced bump occurring at time $t \approx 100$ ps is clearly observed. The lower panels in Fig. 10.3 show emission spectra at different fixed delay times t. Panel (d) reveals, that the strain wave induces both, a shift and a broadening of the PL spectra.
Figure 10.4 shows the time evolutions of the energy of the PL maximum (panel (a)), of the spectral width of the emission (panel (b)) and of the PL intensity integrated over the emission line (panel (c)). The energy shift induced by the strain pulse reaches a maximum value of $\Delta E_{LP} \approx 0.2$ meV (panel (a)). Further, the shift is almost independent of the delay between the strain and the PL excitation pulses (see inset). The width of the spectrum increases in the presence of the strain pulse (panel (b)), whereas the integrated PL intensity of the lower polariton branch decreases (panel (c)) when the PL linewidth starts to increase ($t = 0$), then rapidly increases simultaneously with the shift of the emission line, and thereafter decreases again. From the comparison of the leading edge of the energy shift with those of spectral width and intensity, it is seen that this shift starts with a delay with respect to the two other quantities.
In the analysis of the strain-induced effect on the PL spectrum of the MC two effects have to be considered: (i) the strain-induced change in the length and the refractive index of the MC and (ii) the strain-induced change in the exciton resonance energy E_x in the QW [77]. At first the contributions of (i) and (ii) to the strain-induced energy shift of the PL line will be discussed (Figs. 10.3(b) and 10.4(a)). Both effects modulate the detuning $E_x - E_c$ and, therefore, the energies of the two polariton branches, as can be seen from Fig. 10.1(b). To estimate the two contributions consider the temporal profile $\eta(t)$ of the strain pulse in Fig. 10.2(b). The change in the strain pulse shape due to the multilayered Bragg mirrors (Chapter 8) [50] is ignored in the following discussion. According to Chapter 6 the strain wave induces a combined cavity energy shift which is $\Delta E_c^{max} < 0.1$ meV when the strain passes the λ-cavity interface, taking into account the displacement of the interfaces as well as the photoelastic effect. The second contribution (ii) gives a maximum strain-induced change in the exciton resonance energy by $\Delta E_x^{max} \sim 1$ meV and however occurs when the maximum strain reaches the quantum well.

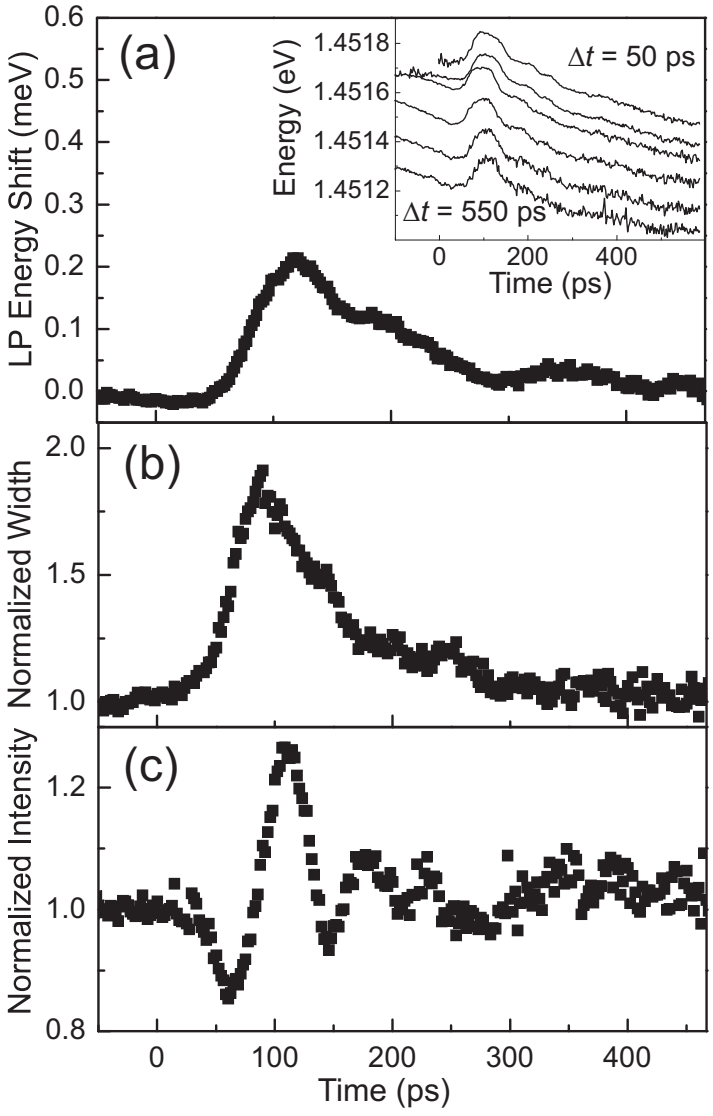

Figure 10.4: Temporal evolution of the LP line at T=1.8 K: (a) energy shift, (b) spectral width, and (c) integral PL intensity of the LP line normalized to the spectral width and integral intensity in the absence of a strain pulse. The inset shows the temporal evolution of the PL energy measured for various time delays Δt, between the pulses for PL excitation and strain pulse injection. The step between the delays is 100 ps. The upper curve corresponds to the shortest delay when the arrival of the strain pulse at the QW coincides with the maximum PL intensity. For better comparison the time scales have been shifted by the corresponding delay so that the curves lie on top of each other.

This can be evaluated from measurements under similar experimental conditions for a GaAs/(Al,Ga)As QW without a surrounding cavity [77]. Inserting the estimated values of ΔE_x^{max} and ΔE_c^{max} into the dependence of the lower polariton energy on $E_x - E_c$ Fig. 10.1(b), however it can be easily seen that contribution (ii) dominates over contribution (i) in the net straininduced PL energy shift, yielding $\Delta E_{LP} \approx 0.17$ meV. This value is in good agreement with the experimentally measured lower polariton energy shift $\Delta E_{LP} \approx 0.2$ meV (shown in Fig. 10.4(a)).

The strain wave packet acts on the MC as a bipolar strain pulse (Fig 10.2(b)). The compression part of the pulse $\eta(t) < 0$ is followed by a tensile perturbation ($\eta(t) > 0$). Thus ΔE_x is expected to change sign from positive for $\eta(t) < 0$ to negative for $\eta(t) > 0$ (see Chapter 7) [77]. Therefore also ΔE_{LP} should change its sign in phase with ΔE_x. However, this is not observed experimentally where only $\Delta E_{LP} > 0$ is detected (Fig. 10.3(b)). Qualitatively this can be explained by the strong quenching of the lower polariton branch PL for decreasing detuning (see Fig. 10.1(c) and Ref. [110]).

Consequently the PL signal during compression will give a much greater contribution than the PL signal during the tensile part to the signal $I(E,t)$, recorded with a limited time resolution. As a result $\Delta E_{LP} < 0$ is not observed in Fig. 10.3(b).
The observation of the lower polariton PL energy shift due to the modulation of E_x is possible only due to the strong coupling between the photon mode and the exciton resonance. An increase in the optical excitation density reduces this coupling (i.e. decreases the Rabi splitting). This explains the observed shift of the lower polariton PL peak up to 1.4515 eV at early delays in Fig. 10.3(a) from its energy position $E_{LP} = 1.4510$ eV measured for cw-low power optical excitation (Fig.10.1(a)). The dependence of the coupling strength on excitation density also results in a decrease in E_{LP} during the PL decay after pulsed excitation (Fig. 10.3(a) and Ref. [106][107]). However, the strain-induced shift $\Delta E_{LP} \sim 0.2$ meV does not depend on the polariton density in the experiments. This is demonstrated in the inset of Fig. 10.4(a) where ΔE_{LP} is almost independent of the delay between the pulsed optical excitation of the MC and the arrival of the strain pulse. Therefore here the density dependent effects can be neglected in the analysis of the strain-induced PL energy shift. However, for other experimental conditions than the ones realized here excitation density dependent effects in the light-matter coupling might become important for the strain induced PL changes.
The start of the strain-induced effect on the spectral width (Fig. 10.4(b)) and PL intensity (Fig. 10.4(c)) is shifted by 30 ± 10 ps to earlier times compared to the PL energy shift (Fig. 10.4(a)). This value agrees very well with the time for a distance of $x = 120$ nm (Fig. 10.2(a)), which a strain pulse travels during its motion from the edge of the Bragg mirror to the QW, as shown by the horizontal bar in Fig. 10.2(a). In fact, the strain pulse reaches first the internal edge of the Bragg mirror inducing a small energy shift hard to resolve with the used experimental setup. A much better indicator of the small cavity energy shift is the emitted lower polariton luminescense intensity which depends strongly on the detuning (Fig. 10.1(c)). Already small changes of the detuning $E_x - E_c$ are visible in the luminescense response. The strain-induced cavity mode energy changes, and the energy shift of the exciton in the QW give different signs for the PL intensity changes at the considered times. Together with different arrival times of the strain pulse at the cavity structure and the QW this results in the oscillation observed in Fig. 10.4(c). Also a broadening of the spectra might be observed taking into account the results of Chapters 6 and 8, which show, that small amplitude energy oscillation are expected, when the strain wave approaches the λ-cavity, where the period (≈ 23 ps) is below the experimental timeresolution.
The PL energy and intensity modulation obviously depend on the initial detuning $E_x - E_c$. In the present work this value is chosen positive and not too far from the Rabi splitting value. In this case we get a considerable energy modulation without strong changes in the PL intensity. From Figs. 10.1(b) and 10.1(c) it is clear that having a detuning closer to the resonance $E_x - E_c = 0$, the energy modulation will have higher amplitude but the intensity of the PL will be lower. Therefore values $E_x - E_c < 0$ appear to be not useful because of the low PL intensity.

10.4 Conclusions

In conclusion subterahertz modulation of the light-emission spectrum from a semiconductor quantum well strongly coupled to a high quality planar microcavity has been demonstrated. The modulation is achieved by injecting a picosecond strain pulse into the microcavity. The experiments open the way to ultrafast control of light emission in photonic devices using monochromatic sound, strain wave packets, and acoustic solitons. Further, experiments in which the strain pulse controls optically stimulated processes in a cavity, like lasing properties or Rabi flopping times (compare Chapter 9) as well as the manipulation of polariton condensates may become feasible.

11 Summary and Future Prospects

Summarizing the experiments and the experimental results obtained in Part II, a series of measurements has been presented, subsequently building up the basis for understanding the interaction of a picosecond strain wave with semiconductor quantum wells, semiconductor Bagg microcavities and the combined strongly coupled system.
It has been shown that the two main investigated constituents, namely a quantum well and a microcavity, representing electro-optic and elasto-optic components respectively, show very different response to the strain wave. Thereby both of them have turned out to be prospective structures for beyond-linewidth modulation within picoseconds as long as the definition of stationary linewidth is not hampered by the fundamental restriction of the finite coherent optical decay among the respective structure.
However, the achieved maximum energy shift is quite different. In the investigated Bragg microcavity the maximum shift from higher to lower energies was about 1 meV and could be explained by elasto-optical and dimensional considerations. The time to perform this shift was limited by the microcavity spatial dimensions to ~ 10 ps. In the quantum well, energy shifts of more than 10 meV have been reported. The temporal and spectral resolution of the detection was shown to be limited not by the experimental setup but by the inherent properties of the quantum well. The important parameters thereby were the quantum well thickness and the coherent resonant polarisation decay of the quantum well exciton. The exciton resonance thereby was shown to be stronly chirped and even doubled structures appear in the spectra due to fast and strong energy modulation.
Contrary, in the strongly coupled quantum well-microcavity system, the shifts of the polariton energies are limited by the avoided crossing of coupled resonances. It has been demonstrated that the shift to higher energies of the involved exciton can be as high as 40 meV within maximum ~ 7 ps. This fast shift produced a purely photonic lower polariton mode, which indicates and effective switch-off of the strong light matter interaction. The coherent optical decay has been further shown to be not a drawback, blurring the spectral response of the modulation process, but may lead to well defined sidebands in the detected spectrum in the diabatic modulation regime, from which information about the speed and amplitude of any underlying modulation process might be obtained.
Finally, the emission dynamics of the lower polariton luminescense decay have been investigated, where a picosecond modulation of the polariton energy as well as of the emitted intensity was found. The intensity modulation thereby was shown to be strongly dependent on the resonance detuning in the coupled system and might constitute a highly sensitive detector for small energy shifts of the underlying resonances

supposed that the detection time resolution is below the limit of the strain induced spectral changes.
The important ratios of the relevant timescales in the experiments might be tailored by the growth process of the semiconductor structures as well as by the adaptation of the strain wave excitation and injection process to the required experimental conditions. The results suggest a high relevance for future research and applications. There are many different structures available potentially showing different response to a strain wave. It is obvious and particularly attractive, that self assembled semiconductor quantum dots, as very tiny, highly strained objects, are expected to show strong optical response to an applied strain wave. Further the geometry in the experiments might be changed increasing for example the elasto-optic response. It might be possible to build up novel pulsed thermal light sources with pulse durations in the order of picoseconds, or on the other hand to influence the laser properties of certain structures. Further information on ultrafast phasetransitions might be obtained and coherent control of light matter interaction using sub-rabi-cycle modulation of quantum well optical polaritons as well as dynamic carrier trapping in bulk materials appear to be seizable.
To veer away from the presented data in this work, all materials that show a piezo response in the broadest sense (e.g. magnetostriction or piezoelectricity) are attractive candidates for efficient picosecond modulation spectroscopy. The idea of acoustic shockwave modulation thereby holds also at roomtemperature; a fact which allows the technique to adopt a prominent position among future ultrafast optical modulation spectroscopy techniques.

Bibliography

[1] N. W. Ashcroft and N. D. Mermin. *Solid State Physics*. Holt, Rinehart and Winston, New York, (1976).

[2] R. Biswas and D. R. Hamann. New classical models for silicon structural energies. *Phys. Rev. B*, **36**:6434, (1987).

[3] G. Dolling and R. A. Cowley. The thermodynamics and optical properties of germanium, silicon, diamond and gallium arsenide. *Proc. Phys. Soc.*, **88**:463, (1966).

[4] P. N. Keating. Effect of invariance requirements on the elastic strain energy of crystals with application to the diamond structure. *Phys. Rev.*, **145**:637, (1966).

[5] W. Weber. Adiabatic bond charge model for the phonons in diamond, Si, Ge, and α-Sn. *Phys. Rev. B*, **15**:4789, (1977).

[6] G. P. Srivastava. *The Physics of Phonons*. Adam Hilger, Bristol, Philadelphia and New York, (1990).

[7] C. Colvard; T. A. Gant; M. V. Klein; R. Merlin; R. Fisher; H. Morkoc and A. C. Gossard. Folded acoustic and quantized optic phonons in GaAl/As superlattices. *Phys. Rev. B*, **31**:2080, (1985).

[8] O. B. Wright; B. Perrin; O. Matsuda and V. E. Gusev. Ultrafast carrier diffusion in gallium arsenide probed with picosecond acoustic pulses. *Phys. Rev. B*, **64**:081202(R), (2001).

[9] T. D. Krauss and F. W. Wise. Coherent Acoustic Phonons in a Semiconductor Quantum Dot. *Phys. Rev. Lett.*, **79**:5102, (1997).

[10] A. Bartels; T. Dekorsey; H. Kurz and K. Köhler. Coherent Zone-Folded Longitudinal Acoustic Phonons in Semiconductor Superlattices: Excitation and Detection. *Phys. Rev. Lett.*, **82**:1044, (1999).

[11] A. J. Kent; R. N. Kini; N. M. Stanton; M. Henini; B. A. Glavin; V. A. Kochelap and T. L. Linnik. Acoustic Phonon Emission from a Weakly Coupled Superlattice under Vertical Electron Transport: Observation of Phonon Resonance. *Phys. Rev. Lett.*, **96**:215504, (2006).

[12] C. Thomson; H. T. Grahn; H. J. Maris and J. Tauc. Surface generation and detection of phonons by picosecond light pulses. *Phys. Rev. B*, **34**:4129, (1986).

[13] H.-Y. Hao and H. J. Maris. Dispersion of the long-wavelength phonons in Ge, Si, GaAs, quartz, and sapphire. *Phys. Rev. B*, **63**:224301, (2001).

[14] E. Pronne and B. Perrin. Generation and detection of acoustic solitons in crystalline slabs by laser ultrasonics. *Ultrasonics*, **44**:e1203, (2006).

[15] O. L. Muskens and J. I. Dijkhuis. High amplitude, ultrashort, longitudinal strain solitons in sapphire. *Phys. Rev. Lett.*, **89**:285504, (2002).

[16] E. J. Reed; M. Soljacic and J. D. Joannopoulos. Reversed Doppler Effect in Photonic Crystals. *Phys. Rev. Lett*, **91**:133901, (2003).

[17] Jr; M. M. de Lima and P. V. Santos. Modulation of photonic structures by surface acoustic waves. *Rep. Prog. Phys.*, **68**:1639, (2005).

[18] S. Tamura; D. C. Hurley and J. P. Wolfe. Acoustic-phonon propagation in superlattices. **38**:1427, (1988).

[19] G. Tas and H. J. Maris. Electron diffusion in metals studied by picosecond ultrasonics. *Phys. Rev. B*, **49**:15046, (1994).

[20] P. J. S. van Capel. *Ultrafast nonlinear acoustics in crystals and nanostructures*. Utrecht University, (2008).

[21] O. B. Wright. Ultrafast nonequilibrium stress generation in gold and silver. *Phys. Rev. B*, **49**:9985, (1994).

[22] J. Wang and C. Guo. Effect of electron heating on femtosecond laser-induced coherent acoustic phonons in noble metals. *Phys. Rev. B*, **75**:184304, (2007).

[23] A. F. Bower. *Applied Mechanics of Solids*. CRC, (2009).

[24] O. L. Muskens. *High-Amplitude, ultrashort strain solitons in solids*. Utrecht University, (2004).

[25] D. C. Wallace. *Solid State Physics*, volume 25. Academic Press, (1970).

[26] H. Reismann; P. S. Pawlik. *Elasticity, Theory and Applications*. John Wiley & Sons, (1980).

[27] H.-Y. Hao and H. J. Maris. Experiments with acoustic solitons in crystalline solids. *Phys. Rev. B*, **64**:064302, (2001).

[28] T. Dauxois; M. Peyrard. *Physics of Solitons*. Cambridge University Press, (2006).

[29] A. V. Scherbakov; P. J. S. van Capel; A. V. Akimov; J. I. Dijkhuis; D. R. Yakovlev; T. Berstermann and M. Bayer. Chirping of an Optical Transition by an Ultrafast Acoustic Soliton Train in a Semiconductor Quantum Well. *Phys. Rev. Lett.*, **99**:057402, (2007).

[30] N. C. Frateschi; A. P. Kanjamala; A. F. J. Levi and T. Tanbun-Ek. Polarization of lasing emission in microdisk laser diodes. *Appl. Phys. Lett.*, **66**:1859, (1995).

[31] J. M. Gerard; O. Cabrol and B. Sermage. InAs quantum boxes: Highly efficient radiative traps for light emitting devices on Si. *Appl. Phys. Lett.*, **68**:3123, (1996).

[32] G. V. Prakash; L. Besombes; T. Kelf; J. J. Baumberg; P. N. Bartlett and M. E. Abdelsalam. Tunable resonant optical microcavities by self-assembled templating. *Opt. Lett.*, **29**:1500, (2004).

[33] Y. Akahane; T. Asano; B.-S. Song and S. Noda. Fine-tuned high-Q photonic-crystal nanocavity. *Opt. Express*, **13**:1202, (2005).

[34] K. J. Vahala. Optical microcavities. *Nature*, **424**:839, (2003).

[35] A. V. Kavokin; J. J. Baumberg; G. Malpuech; F. P. Laussy. *Microcavities.* Oxford University Press, (2007).

[36] C. B. Fu; C. S. Yang; M. C. Kuo; Y. J. Lai; J. Lee; J. L. Shen; W. C. Chou and S. Jeng. High Reflectance ZnTe/ZnSe Distributed Bragg Reflector at 570 nm. *Chinese Journal of Physics*, **41**:535, (2003).

[37] G. T. Moore. Quantum Theory of the Electromagnetic Field in a Variable-Length One-Dimensional Cavity. *J. math. Phys.*, **11**:2679, (1970).

[38] E. L. Ivchenko. *Optical Spectroscopy of Semiconductor Nanostructures.* Springer, Berlin, (2004).

[39] N. Peyghambarian; S. W. Koch; A. Mysyrowicz. *Introduction to Semiconductor Optics.* Prentice Hall, Englewood Cliffs, New Jersey 07632, (1993).

[40] G. H. Wannier. The structure of electronic excitation levels in insulating crystals. *Phys. Rev.*, **52**:191, (1937).

[41] S. W. Kirchoefer; N. Holonyak; K. Hess; D. A. Gulino; H. G. Drickamer; J. J. Coleman and P. D. Dapkus. Absorption measurements at high pressure on AlAs-Al_xGa_{1-x}As-GaAs superlattices. *Appl. Phys. Lett.*, **40**:821, (1982).

[42] D. A. B. Miller; D. S. Chemla; T. C. Damen; A. C. Gossard; W. Wiegmann; T. H. Wood; C. A. Burrus. Band-Edge Electroabsorption in Quantum Well Structures: The Quantum-Confined Stark Effect. *Phys. Rev. Lett.*, **53**:2173, (1984).

[43] K. K. Bajaj R. L. Greene. . *Solid State Commun.*, **45**:831, (1983).

[44] C. Weisbuch; B. Vinter. *Quantum Semiconductor Structures.* Academic Press, London, (1991).

[45] E. L. Ivchenko; P. S. Kopev; V. P. Kochereshko; I. N. Uraltsev; D. R. Yakovlev; S. V. Ivanov; B. Ya. Meltser and M. A. Kalitievskii. Reflection in the exciton region of the spectrum of a structure with a single quantum well. Oblique and normal incidence of light. *Sov. Phys. Semicond.*, **22**:495, (1988).

[46] C. Weisbuch; M. Nishioka; A. Ishikawa and Y. Arakawa. Observation of the Coupled Exciton-Photon Mode Splitting in a Semiconductor Quantum Microcavity. *Phys. Rev. Lett.*, **69**:3314, (1992).

[47] E. M. Purcell. Spontaneous Emission Probabilities at Radio Frequencies. *Phys. Rev.*, **69**:681, (1946).

[48] B. Sermage; S. Long; I. Abram; J. Y. Marzin; J. Bloch; R. Planel; V. Thierry-Mieg. Time-resolved spontaneous emission of excitons in a microcavity: Behavior of the individual exciton-photon mixed states. *Phys. Rev. B*, **53**:16516, (1996).

[49] J. J. Hopfield. Theory of the contribution of excitons to the complex dielectric constant of crystals. *Phys. Rev.*, **112**:1555, (1958).

[50] T. Berstermann; A. V. Scherbakov; A. V. Akimov; D. R. Yakovlev; N. A. Gippius; B. A. Glavin; I. Sagnes; J. Bloch and M. Bayer. Terahertz polariton sidebands generated by ultrafast strain pulses in an optical semiconductor microcavity. *Phys. Rev. B*, **80**:075301, (2009).

[51] T. Berstermann; C. Brggemann; M. Bombeck; A. V. Akimov; D. R. Yakovlev; C. Kruse; D. Hommel and M. bayer. Optical bandpass switching by modulating a microcavity using ultrafast acoustics. *Accepted for publication in Phys. Rev. B, (2010).*

[52] S. Adachi. *Properties of Group-iV, III-V and II-VI Semiconductors.* John Wiley & Sons, (2005).

[53] Amnon Yariv and Pochi Yeh. *Optical Waves in Crystals.* John Wiley Sons, (1984).

[54] B. H. Bairamov; A. V. Gol'tsev; V. V. Toporov; R. Laiho and T. Levola. Photoelastic coefficients and deformation-potential constants of ZnSe crystals. *Phys. Rev. B*, **33**:5875, (1986).

[55] P. Y. Yu and M. Cardona. *Fundamentals of Semiconductors, Physics and Materials Properties.* Springer, Berlin, (1996).

[56] F. H. Pollak and M. Cardona. Piezo-Electroreflectance in Ge, GaAs, and Si. *Phys. Rev.*, **172**:816, (1968).

[57] G. L. Bir and G. E. Pikus. *Symmetry and Strain-Induced Effects in Semiconductors.* John Wiley & Sons, (1974).

[58] J. S. Blakemore. Semiconducting and other major properties of gallium arsenide. *J. Appl. Phys.*, **53**:R123, (1982).

[59] S. Reitzenstein; C. Hofmann; A. Gorbunov; M. Strau; S. H. Kwon; C. Schneider; A. Löffler; S. Höfling; M. Kamp; and A. Forchel. AlAs/GaAs micropillar cavities with quality factors exceeding 150.000. *Appl. Phys. Lett.*, **90**:251109, (2007).

[60] D. Grard; V. Laude; B. Sadani; A. Khelif; D. Van Labeke; and B. Guizal. Modulation of the extraordinary optical transmission by surface acoustic waves. *Appl. Phys. Lett.*, **76**:235427, (2007).

[61] J. J. Baumberg; D. A. Williams; and K. Köhler. Ultrafast Coherent Control and Destruction of Excitons in Quantum Wells. *Rep. Rev. Lett*, **75**:2598, (1995).

[62] A. Bartels; T. Dekorsy; H. Kurz; and K. Koehler. Coherent Control of acoustic phonons in semiconductor superlattices. *Appl. Phys. Lett.*, **72**:2844, (1998).

[63] C.-K. Sun; J.-C. Liang; X.-Y. Yu. Coherent Acoustic Phonon Oscillations in Semiconductor Multiple Quantum Wells with Piezoelectric Fields. *Phys. Rev. Lett.*, **84**:179, (2000).

[64] M. F. Pascual Winter; G. Rozas; A. Fainstein; B. Jusserand; B. Perrin; A. Huynh; P. O. Vaccaro; and S. Saravanan. Selective Optical Generation of Coherent Acoustic Nanocavity Modes. *Phys. Rev. Lett.*, **98**:265501, (2007).

[65] N. D. Lanzillotti-Kimura; A. Fainstein; A. Huynh; B. Perrin; B. Jusserand; A. Miard; and A. Lemaitre. Coherent Generation of Acoustic Phonons in an Optical Microcavity. *Phys. Rev. Lett.*, **99**:217405, (2007).

[66] A. V. Akimov; Y. Tanaka; A. B. Pevtsov; S. F. Kaplan; V. G. Golubev; S. Tamura; D. R. Yakovlev and M. Bayer. Hypersonic Modulation of Light in Three-Dimensional Photonic and Phononic Band-Gap Materials. *Phys. Rev. Lett.*, **101**:033902, (2008).

[67] C. Kruse; S. M. Ulrich; G. Alexe; E. Roventa; R. Kröger; B. Brendemühl; P. Michler; J. Gutowski; and D. Hommel. Green monolithic II-VI vertical-cavity surface-emitting laser operating at room temperature. *Phys. Stat. Sol. B*, **241**:731, (2004).

[68] R. Granger; J. T. Benhlal; O. Ndap and R. Triboulet. Optical properties and temperature dependence of critical transitions in ZnSe. *Eur. Phys. J. B*, **13**:429, (2000).

[69] B. Perrin; E. Pronne; L. Belliard. Generation and detection of incoherent phonons in picosecond ultrasonics. *Ultrasonics*, **44**:1277, (2006).

[70] P. J. S. van Capel; H. P. Porte; G. van der Star and J. I. Dijkhuis. Interferometric detection of acoustic shock waves. *Journal of Physics: Conference Series*, **92**:012092, (2007).

[71] O. Matsuda and O. B. Wright. Reflection and transmission of light in multilayers perturbed by picosecond strain pulse propagation. *J. Opt. Soc. Am. B*, **19**:3028, (2002).

[72] O. L. Muskens; A. V. Akimov and J. I. Dijkhuis. Coherent Interactions of Terahertz Strain Solitons and Electronic Two-Level Systems in Photoexcited Ruby. *Phys. Rev. Lett.*, **92**:035503, (2004).

[73] B. C. Daly; T. B. Norris; J. Chen and J. B. Khurgin. Picosecond acoustic phonon pulse propagating in silicon. *Phys. Rev. Lett.*, **70**:214307, (2004).

[74] O. L. Muskens and J. I. Dijkhuis. Interactions of ultrashort strain solitons and terahertz electronic two-level systems in photoexcited ruby. *Phys. Rev. B*, **71**:104304, (2005).

[75] G . V. Astakhov; D. R. Yakovlev; V. P. Kochereshko; W. Ossau; W. Faschinger; J. Puls; F. Henneberger; S. A. Crooker; Q. McCulloch; D. Wolverson; N. A. Gippius and A. Waag. Binding energy of charged excitons in ZnSe-based qantum wells. *Phys. Rev. B*, **65**:165335, (2002).

[76] P. J. S. van Capel and J. I. Dijkhuis. Optical generation and detection of shock waves in sapphire at room temperature. *Appl. Phys. Lett.*, **88**:151910, (2006).

[77] A. V. Akimov; A. V. Scherbakov; D. R. Yakovlev; C. T. Foxon; and M. Bayer. Ultrafast Band-Gap Shift Induced by a Strain Pulse in Semiconductor Heterostructures. *Phys. Rev. Lett*, **97**:037401, (2006).

[78] B. H. Lee. Elastic Constants of ZnTe and ZnSe between 77-300K. *J. Appl. Phys.*, **41**:2984, (1970).

[79] A. V. Akimov. *Electron-Phonon Interaction in Low-Dimensional Structures.* Oxford University Press, Oxford, (2003).

[80] E. J. Mayer; N. T. Pelekanos; J. Kuhl; N. Magnea and H. Mariette. Homogeneous linewidth of excitons in CdTe/(Cd,Zn)Te single quantum wells. *Phys. Rev. B*, **51**:1995, (1994).

[81] H. P. Wagner; A. Schätz; R. Mayer; W. Langbein and J. M. Hvam. Coherent optical nonlinearities and phase relaxation of quasi-three-dimensional and quasi-two-dimensional excitons in $ZnS_xSe_{1-x}/ZnSe$ structures. *Phys. Rev. B*, **56**:12581, (1997).

[82] Ü. Özguer; C.-W. Lee and H. O. Everitt. Control of Coherent Acoustic Phonons in Semiconductor Quantum Wells. *Phys. Rev. Lett.*, **86**:5604, (2001).

[83] P. H. Bucksbaum. The Future of Attosecond Spectroscopy. **317**:766, (2007).

[84] M. R. Armstrong; E. J. Reed; Ki-Yong Kim; J. H. Glownia; W. M. Howard; E. L. Piner and J. C. Roberts. Observation of terahertz radiation coherently generated by acoustic waves. **5**:285, (2009).

[85] L. A. Kulakova and I. S. Tarasov. Optical bandpass switching by modulating a microcavity using ultrafast acoustics. *JETP Lett.*, **78**:67, (2003).

[86] M. M. de Lima Jr.; M. van der Poel; P. V. Santos and J. M. Hvam. Phonon-Induced Polariton Superlattices. *Phys. Rev. Lett.*, **97**:045501, (2006).

[87] C. Weisbuch; H. Benisty and R. Houdre. Overview of fundamentals and applications of electrons, excitons and photons in confined structures. *J. Lumin.*, **85**:271, (2000).

[88] A. Huynh; B. Perrin; N. D. Lanzillotti-Kimura; B. Jusserand; A. Fainstein and A. Lemaitre. Subterahertz monochromatic acoustic wave propagation using semiconductor superlattices as transducers. *Phys. Rev. B*, **78**:233302, (2008).

[89] H. T. Grahn; D. A. Young; H. J. Maris; J. Tauc; J. M. Hong and T. P. Smith. Sound velocity and index of refraction of AlAs measured by picosecond ultrasonics. *Appl. Phys. Lett.*, **53**:2023, (1988).

[90] E. Anastassaki. Ionic photoelasticity of GaAs. *J. Phys. C: Solid State Physics*, **16**:3329, (1983).

[91] I. Vurgaftman; J. R. Meyer and L. R. Ram-Mohan. Subterahertz monochromatic acoustic wave propagation using semiconductor superlattices as transducers. *J. Appl. Phys.*, **89**:5815, (2001).

[92] S. G. Tikhodeev; A. L. Yablonskii; E. A. Muljarov; N. A. Gippius and T. Ishihara. Quasiguided modes and optical properties of photonic crystal slabs. *Phys. Rev. B*, **66**:045102, (2002).

[93] N. A. Gippius; S. G. Tikhodeev and T. Ishihara. Optical properties of photonic crystal slabs with an asymmetrical unit cell. *Phys. Rev. B*, **72**:045138, (2005).

[94] Jr. J. Kono; M. Y. Su; T. Inoshita; T. Noda; M. S. Sherwin; S. J. Allen and H. Sakaki. Resonant Terahertz Optical Sideband Generation from Confined Magnetoexcitons. *Phys. Rev. Lett*, **79**:1758, (1997).

[95] G. Khitrova; H. M. Gibbs; F. Jahnke; M. Kira and S. W. Koch. Nonlinear optics of normal-mode-coupling semiconductor microcavities. *Rev. Mod. Phys.*, **71**:1591, (1999).

[96] M. Schwab; H. Kurtze; T. Auer; T. Berstermann; M. Bayer; J. Wiersig; N. Baer; C. Gies; F. Jahnke; J. P. Reithmaier; A. Forchel; M. Benyoucef and P. Michler. Radiative emission dynamics of quantum dots in a single cavity micropillar. *Phys. Rev. B*, **74**:045323, (2006).

[97] B. M. Möller; U. Woggon and M. V. Artemyev. Bloch modes and disorder phenomena in coupled resonator chains. *Phys. Rev. B*, **75**:245327, (2007).

[98] P. L. Gourley. Microstructured semiconductor lasers for high-speed information processing. *Nature*, **371**:571, (1994).

[99] G. Dasbach; T. Baars; M. Bayer; A. Larionov and A. Forchel. Coherent and incoherent polaritonic gain in a planar semiconductor microcavity. *Phys. Rev. B*, **62**:13076, (2000).

[100] J. Majer; J. M. Chow; J. M. Gambetta; J. Koch; B. R. Johnson; J. A. Schreier; L. Frunzio; D. I. Schuster; A. A. Houck; A. Wallraff; A. Blais; M. H. Devoret; S. M. Girvin and R. J. Schoelkopf. Coupling superconducting qubits via a cavity bus. *Phys. Rev. Lett.*, **449**:443, (2007).

[101] J. Kasprzak; M. Richard; S. Kundermann; A. Baas; P. Jeambrun; J. M. J. Keeling; F. M. Marchetti; M. H. Szymanska; R. Andre; J. L. Staehli; V. Savona; P. B. Littlewood; B. Deveaud and Le Si Dang. Bose-Einstein condensation of exciton polaritons. *Nature*, **443**:409, (2006).

[102] M. W. Noel; W. M. Griffith; T. F. Gallagher. Frequency-modulated excitation of a two-level atom. *Phys. Rev. A*, **58**(2265), (1998).

[103] G. Günter; A. A. Anappara; J. Hees; A. Sell; G. Biasiol; L. Sorba; S. De Liberato; C. Ciuti; A. Tredicucci; A. Leitenstorfer and R. Huber. Sub-cycle switch-on of ultrastrong light-matter interaction. *Nature*, **458**:178, (2009).

[104] A. V. Scherbakov; T. Berstermann; A. V. Akimov; D. R. Yakovlev; G. Beaudoin; D. Bajoni; I. Sagnes; J. Bloch and M. Bayer. Ultrafast control of light emission from a quantum-well semiconductor microcavity using picosecond strain pulses. *Phys. Rev. B*, **78**:241302(R), (2008).

[105] R. Butte; G. Delalleau; A. I. Tartakovskii; M. S. Skolnick; V. N. Astratov; J. J. Baumberg; G. Malpuech; A. Di Carlo; A. V. Kavokin and J. S. Roberts. Transition from strong to weak coupling and the onset of lasing in semiconductor microcavities. *Phys. Rev . B*, **65**:205310, (2002).

[106] J. Bloch; B. Sermage; C. Jacquot; P. Senellart and V. Thierry-Mieg. Time resolved stimulated emission in excitonic semiconductor microcavities. *Physica E*, **13**:390, (2002).

[107] F. Quochi; G. Bongiovanni; A. Mura; J. L. Staehli; B. Deveaud; R. P. Stanley; U. Oesterle and R. Houdre. Strongly Driven Semiconductor Microcavities: From the Polariton Doublet to an ac Stark Triplet. *Phys. Rev. Lett.*, **80**:4733, (1998).

[108] J. R. Gell; M. B. Ward; A. J. Shields; P. Atkinson; S. P. Bremner; D. Anderson; M. Kataoka; C. H. W. Barnes; G. A. C. Jones and D. A. Ritchie. Temporal characteristics of surface-acoustic-wave-driven luminescence from a lateral p-n junction. *Appl. Phys. Lett.*, **91**:013506, (2007).

[109] R. Pratt; T. Takamori and T. Kamijoh. Temperature dependence of the cavity-polariton mode splitting in a semiconductor microcavity. *Phys. Rev. B*, **58**:9656, (1998).

[110] R. P. Stanley; R. Houdre; C. Weisbuch; U. Oesterle and M. Ilegems. Cavity-polariton photoluminescense in semiconductor microcavities: Experimental evidence. *Phys. Rev. B*, **53**:10995, (1996).

List of Publications

1. T. Berstermann, C. Brüggemann, M. Bombeck, A. V. Akimov, D. R. Yakovlev, I. Sagnes, J. Bloch and M. Bayer. *Sub-Rabi-Cycle Coherent Control of Light-Matter Interaction by THz acoustics.* In preparation.

2. A. Pawlis, T. Berstermann, C. Brüggemann, M. Bombeck, D. R. Yakovlev, K. Lischka and M. Bayer. *Depth Resolved Spectroscopy via Local Dynamical Band-structure Tuning in a Strained ZnMgSe/ZnSe Quantum Well.* In preparation.

3. A. S. Salasyuk, A. V. Scherbakov, D. R. Yakovlev, A. V. Akimov, A. A. Kaplyanskii, S. F. Kaplan, S. A. Grudinkin, A. V. Nashchekin, A. B. Pevtsov, V. G. Golubev, T. Berstermann, C. Brüggemann, M. Bombeck and M. Bayer. *Filtering of elastic waves by opal-based hypersonic crystals.* Nano Letters **10**, 1319 (2010).

4. T. Berstermann, C. Brüggemann, M. Bombeck, A. V. Akimov, D. R. Yakovlev, C. Kruse, D. Hommel and M. Bayer. *Optical bandpass switching by modulating a microcavity using ultrafast acoustics.* Physical Review B **81**,085316 (2010).

5. T. Berstermann, A. V. Scherbakov, A. V. Akimov, D. R. Yakovlev, N. A. Gippius, B. A. Glavin, I. Sagnes, J. Bloch and M. Bayer. *Terahertz polariton sidebands generated by ultrafast strain pulses in an optical semiconductor microcavity.* Physical Review B **80**, 075301 (2009).

6. J. Wiersig, C. Gies, F. Jahnke, M. Aßmann, T. Berstermann, M. Bayer, C. Kistner, S. Reitzenstein, C. Schneider, S. Höfling, A. Forchel, C. Kruse, J. Kalden and D. Hommel. *Direct observation of correlations between individual photon emission events of a microcavity laser.* Nature **460**, 245-249 (2009).

7. A. V. Scherbakov, T. Berstermann, A. V. Akimov, D. R. Yakovlev, G. Beaudoin, D. Bajoni, I. Sagnes, J. Bloch and M. Bayer. *Ultrafast control of light emission from a quantum-well semiconductor microcavity using picosecond strain pulses.* Physical Review B **78**, 241302(R) (2008).

8. A. V. Scherbakov, P. J. S. van Capel, A. V. Akimov, J. I. Dijkhuis, D. R. Yakovlev, T. Berstermann and M. Bayer. *Chirping of an Optical Transition by an Ultrafast Acoustic Soliton Train in a Semiconductor Quantum Well.* Physical Review Letters **99**, 057402 (2007).

9. A. V. Akimov, A. V. Scherbakov, P. J. S. van Capel, J. I. Dijkhuis, T. Berstermann, D. R. Yakovlev and M. Bayer. *Acoustic solitons in semiconductor nanostructures.* Journal of Physics: Conference Series **92**, 012002 (2007).

10. T. Berstermann, T. Auer, H. Kurtze, M. Schwab, D. R. Yakovlev and M. Bayer. *Systematic study of carrier correlations in the electron-hole recombination dynamics of quantum dots.* Physical Review B **76**, 165318 (2007).

11. M. Schwab, H. Kurtze, T. Auer, T. Berstermann, M. Bayer, J. Wiersig, N. Baer, C. Gies, F. Jahnke, J. P. Reithmaier, A. Forchel, M. Benyoucef and P. Michler. *Radiative emission dynamics of quantum dots in a single cavity micropillar.* Physical Review B **74**, 045323 (2006).

12. A. Greilich, M. Schwab, T. Berstermann, T. Auer, R. Oulton, D. R. Yakovlev and M. Bayer. *Tailored quantum dots for entangled photon pair creation.* Physical Review B **73**, 045323 (2006).

Index